

**RESPONSE OF TRANSITION METAL NANOTUBES AND THEIR JANUS
VARIANTS TO MECHANICAL DEFORMATIONS: AN AB INITIO STUDY**

A Dissertation
Presented to
The Academic Faculty

By

Arpit Bhardwaj

In Partial Fulfillment
of the Requirements for the Degree
Doctor of Philosophy in the
School of Civil and Environmental Engineering

Georgia Institute of Technology

May 2023

© Arpit Bhardwaj 2023

**RESPONSE OF TRANSITION METAL NANOTUBES AND THEIR JANUS
VARIANTS TO MECHANICAL DEFORMATIONS: AN AB INITIO STUDY**

Thesis committee:

Dr. Phanish Suryanarayana
School of Civil and Environmental Engi-
neering
Georgia Institute of Technology

Dr. Arash Yavari
School of Civil and Environmental Engi-
neering
Georgia Institute of Technology

Dr. Rampi Ramprasad
School Of Materials Science And Engi-
neering
Georgia Institute of Technology

Dr. Chaitanya S. Deo
George W. Woodruff School of Mechani-
cal Engineering
Georgia Institute of Technology

Dr. Seung Soon Jang
School Of Materials Science And Engi-
neering
Georgia Institute of Technology

Date approved: April 11, 2023

If everything seems under control, you're not going fast enough.

Mario Andretti

Dedicated to my parents

ACKNOWLEDGMENTS

I would like to express my sincere gratitude to my PhD advisor, Dr. Phanish Suryanarayana, for his unwavering support, guidance, and encouragement throughout my PhD program. His invaluable insights and feedback have been instrumental in shaping my research and career. I would also like to extend my heartfelt thanks to my thesis advisory committee members, Dr. Arash Yavari, Dr. Rampi Ramprasad, Dr. Chaitanya S. Seo, and Dr. Seung Soon Jang, for their time, expertise, and valuable feedback that have significantly contributed to the success of my research.

I would like to acknowledge the contributions of my colleagues and friends at Georgia Tech. Dr. Qimen Xu, Dr. Abhiraj Sharma, and Shashikant Kumar have generously shared their knowledge and expertise, and I am grateful for their assistance in resolving my doubts and queries. I also extend my thanks to my lab mates, Boqin Zhang, Xin Jing, David Codony, Mostafa Shojaei, Sayan Bhowmik, and Zixi Zhang, for their insightful discussions and camaraderie.

I am deeply grateful to my parents and sister, whose constant support and unwavering belief in me have been the cornerstone of my success. Their love, encouragement, and guidance have given me the strength to persevere through difficult times and keep my eyes fixed on the goal. I would also like to thank my friends Shyam, Krishna, and Madhavan for their unwavering support and encouragement during my PhD journey.

I gratefully acknowledge the support of the US National Science Foundation (CAREER-1553212) and the PACE HIVE cluster for its computational resources (MRI-1828187). I also acknowledge support from the Clifford and William Greene, Jr. Professorship.

TABLE OF CONTENTS

Acknowledgments	v
List of Tables	ix
List of Figures	xi
Summary	xiv
Chapter 1: Introduction	1
1.1 Background	1
1.2 Motivation	3
1.3 Organization	5
Chapter 2: Systems and methods	6
2.1 Transition metal dichalcogenide (TMD) nanotubes	6
2.1.1 Elastic properties	6
2.1.2 Electromechanical response	9
2.1.3 Spintronic properties: Rashba and Zeeman effect	10
2.2 Janus TMD nanotubes	11
2.2.1 Elastic properties	11
2.2.2 Electromechanical response	13

2.2.3	Spintronic properties: Rashba and Zeeman effect	15
2.3	Janus Transition metal dihalide (TMH) nanotubes	16
2.3.1	Electromechanical properties	16
Chapter 3: Results and discussion		19
3.1	Transition metal dichalcogenide (TMD) nanotubes	19
3.1.1	Elastic properties	19
3.1.2	Electromechanical response	28
3.1.3	Spintronic properties: Rashba and Zeeman effect	34
3.2	Janus TMD nanotubes	36
3.2.1	Elastic properties	36
3.2.2	Electromechanical response	40
3.2.3	Spintronic properties: Rashba and Zeeman effect	49
3.3	Janus Transition metal dihalide (TMH) nanotubes	51
3.3.1	Electromechanical properties	51
Chapter 4: Conclusion		60
4.1	Transition metal dichalcogenide (TMD) nanotubes	60
4.1.1	Elastic properties	60
4.1.2	Electromechanical response	60
4.1.3	Spintronic properties: Rashba and Zeeman effect	61
4.2	Janus TMD nanotubes	62
4.2.1	Elastic properties	62
4.2.2	Electromechanical response	62

4.2.3	Spintronic properties: Rashba and Zeeman effect	63
4.3	Janus Transition metal dihalide (TMH) nanotubes	64
4.3.1	Electromechanical properties	64
Chapter 5: Future work		65
Appendices		67
Chapter A: Nanotube geometry		68
Chapter B: Monolayer stability		77
References		88

LIST OF TABLES

2.1	Equilibrium diameters in nm for the twelve armchair and zigzag Janus TMH nanotubes. The uncertainty in values accounts for the energy differences being smaller than the numerical accuracy in the calculations, i.e., 10^{-6} Ha/atom.	17
3.1	Torsional modulus coefficient (k) and exponent (α) for the forty-five select armchair and zigzag TMD nanotubes.	20
3.2	Young's modulus (Y), shear modulus (G) and Poisson's ratio (ν) for the forty-five select armchair and zigzag Transition Metal Dichalcogenides (TMD) nanotubes from first principles DFT calculations	25
3.3	Variation of bandgap with shear strain (γ) for the forty-five select TMD nanotubes. (D: direct bandgap, I: indirect bandgap).	28
3.4	Variation of the effective mass of holes with shear strain (γ) for the nineteen semiconducting TMD nanotubes.	29
3.5	Variation of the effective mass of electrons with shear strain (γ) for the nineteen semiconducting TMD nanotubes.	30
3.6	Young's modulus (E), Poisson's ratio (ν), and torsional modulus coefficient (\hat{k}) for the twenty-seven select Janus TMD nanotubes from first principles DFT calculations.	38
3.7	Variation of bandgap with axial strain (ε) for the twenty-seven select Janus TMD nanotubes. (D: direct bandgap, I: indirect bandgap).	43
3.8	Variation of the effective mass of electrons with axial strain (ε) for the eleven semiconducting Janus TMD nanotubes.	44
3.9	Variation of the effective mass of holes with axial strain (ε) for the eleven semiconducting Janus TMD nanotubes.	44

3.10	Variation of bandgap with shear strain (γ) for the twenty-seven select Janus TMD nanotubes. (D: direct bandgap, I: indirect bandgap).	45
3.11	Variation of the effective mass of electrons with shear strain (γ) for the eleven semiconducting Janus TMD nanotubes.	46
3.12	Variation of the effective mass of holes with shear strain (γ) for the eleven semiconducting Janus TMD nanotubes.	46
3.13	Variation of bandgap with axial strain (ε) for the twelve Janus TMH nanotubes. (D: direct bandgap, I: indirect bandgap). Red colored data points are used for strains at which the nanotube is expected to be unstable, based on phonon calculations for the monolayer counterparts.	52
3.14	Variation of the effective mass of electrons with axial strain (ε) for the twelve semiconducting Janus TMH nanotubes. Red colored data points are used for strains at which the nanotube is expected to be unstable, based on phonon calculations for the monolayer counterparts.	53
3.15	Variation of the effective mass of holes with axial strain (ε) for the twelve semiconducting Janus TMH nanotubes. Red colored data points are used for strains at which the nanotube is expected to be unstable, based on phonon calculations for the monolayer counterparts.	54
3.16	Variation of bandgap with shear strain (γ) for the twelve select Janus TMH nanotubes. (D: direct bandgap, I: indirect bandgap). Red colored data points are used for strains at which the nanotube is expected to be unstable, based on phonon calculations for the monolayer counterparts.	54
3.17	Variation of the effective mass of electrons with shear strain (γ) for the twelve semiconducting Janus TMH nanotubes. Red colored data points are used for strains at which the nanotube is expected to be unstable, based on phonon calculations for the monolayer counterparts.	55
3.18	Variation of the effective mass of holes with shear strain (γ) for the twelve semiconducting Janus TMH nanotubes. Red colored data points are used for strains at which the nanotube is expected to be unstable, based on phonon calculations for the monolayer counterparts.	55

LIST OF FIGURES

- 2.1 Illustration showing the cyclic and helical symmetry present in a twisted (6,6) TMD nanotube with 2H-t symmetry. In particular, all atoms in the nanotube can be considered to be cyclic and/or helical images of the metal and chalcogen atoms that have been colored red and blue, respectively. This symmetry is exploited while performing electronic structure simulations using the Cyclix-DFT code [111]. 7
- 2.2 Illustration portraying the cyclic+helical symmetry inherent to Janus TMD nanotubes subject to axial/torsional deformations, using a (10,10) 1T-o symmetry nanotube as the representative example (structural model generated using VESTA [166]). In particular, the nanotube can be described by the symmetry operators and the positions of three atoms, e.g., metal and chalcogens colored red and violet/pink, respectively. This structural and resultant electronic symmetry is exploited while performing ab initio calculations using the Cyclix-DFT code [111, 130]. 12
- 2.3 Illustration generated using VESTA [166] that depicts the inherent cyclic and helical symmetry of an axially and torsionally deformed (10,10) 1T-o Janus TMH nanotube. The entire nanotube can be generated using 3 atoms, e.g., metal and halogens colored red and blue/yellow, respectively, that lie within the cyclic+helical symmetry-adapted unit cell. This symmetry is exploited while performing Kohn-Sham DFT calculations using the electronic structure code SPARC's Cyclix-DFT feature. 16
- 3.1 Average torsional modulus coefficient (\hat{k}) for the forty-five select armchair and zigzag TMD nanotubes. 21
- 3.2 Young's modulus (E), shear modulus (G), and Poisson's ratio (ν) of the forty-five select armchair and zigzag TMD nanotubes. The predicted shear modulus refers to that obtained from the isotropic relation in terms of the Young's modulus and Poisson's ratio. The values of R^2 shown in the legend denotes the coefficient of determination for the linear regression. The results correspond to the largest diameter nanotube that has been studied for each material. 23

3.3	The set of computed average torsional modulus coefficients (\hat{k}) and its linear regression with the features being the metal-chalcogen bond length, difference in electronegativity between the metal and chalcogen atoms, and sum of the metal's ionization potential and chalcogen's electron affinity. The values of R^2 shown in the legend denotes the coefficient of determination for the linear regression.	26
3.4	Variation of bandgap with twist for the forty-five select armchair and zigzag TMD nanotubes.	27
3.5	Variation of the difference in effective mass between holes and electrons (holes minus electrons) with twist for the nineteen semiconducting armchair and zigzag TMD nanotubes.	31
3.6	Contours of electron density difference — integrated along the x_1 direction — between the twisted and untwisted armchair nanotube configurations (twisted minus untwisted). The twists chosen for a, b, c, and d correspond to the semiconductor–metal transition; and in e, f, g, and h they correspond to the transition from n-type to p-type semiconductors. The contours are plotted on the x_2x_3 -plane in the corresponding monolayer flat sheet configuration. The charge transfer due to twisting, shown near the corresponding atoms in the lattice structure, is obtained from Bader analysis [197, 198].	33
3.7	Zeeman spin splitting at (a) VBM (Valence Band Maximum) with axial and shear strain and (b) at CBM (Conduction Band Minimum) with axial and shear strain	35
3.8	Rashba spin splitting coefficient at VBM (Valence Band Maximum) with shear strain (Gamma Point)	35
3.9	Torsional modulus coefficient (\hat{k}), Young's modulus (E), and Poisson's ratio (ν) for the twenty-seven select armchair and zigzag Janus TMD nanotubes. Also presented is the shear modulus computed from the torsional modulus coefficient vs. that predicted from the isotropic relation in terms of the Young's modulus and Poisson's ratio. The R^2 values listed in the legend represent the coefficient of determination for the linear regression.	37
3.10	Computed elastic properties and their linear regression, with the features being the metal-chalcogen bond lengths, difference in electronegativity between the chalcogen atoms, and sum of the metal's ionization potential and chalcogens' electron affinity. The R^2 values listed in the legend represent the coefficient of determination for the linear regression.	40
3.11	Variation of bandgap with axial and torsional deformations for the eighteen select armchair and zigzag Janus TMD nanotubes.	42

3.12 (a) The coefficient of determination of the linear regression (R^2) for the linear and quadratic fits of the bandgap vs. axial and shear strain, respectively. (b) The computed bandgap vs. that predicted using the linear regression model. The two outliers: HfSSe and ZrSSe, are not included in the regression. The systems under consideration are the eleven semiconducting armchair Janus TMD nanotubes, with results for the zigzag variants being nearly identical to those presented here.	47
3.13 Variation of the effective mass of holes minus that of the electrons with axial and torsional deformations for the eleven semiconducting Janus TMD nanotubes.	49
3.14 Contours of difference in electron density (integrated along the x_1 direction) between the strained — smallest value at which n-type to p-type semiconductor transition occurs — and unstrained armchair nanotube configurations. The top four panels (a, b, c, and d) correspond to axial deformations, and the bottom four panels (e, f, g, and h) correspond to torsional deformations. Contour plots are on x_2x_3 -plane w.r.t their monolayer flat sheet configuration. The numbers listed next to the atoms correspond to the amount of charge transfer, as determined by Bader analysis [197, 198]. . . .	50
3.15 Zeeman spin splitting at (a) VBM (Valence Band Maximum) with axial and shear strain and (b) at CBM (Conduction Band Minimum) with axial and shear strain	51
3.16 Rashba spin splitting coefficient at VBM (Valence Band Maximum) with shear strain (Gamma Point)	52
3.17 (a), (b): variation of bandgap with axial strains; and (c), (d): variation of bandgap with shear strains for the twelve armchair and zigzag Janus TMH nanotubes. (e): computed bandgap for the undeformed nanotubes vs. that predicted by the linear regression model. (f): coefficient of determination of the linear regression (R^2) for the linear and quadratic fits of the bandgap vs. axial and shear strains, respectively.	53
3.18 The change in bandgap for the twelve armchair Janus TMH nanotubes vs. the percentage contribution of the transition metal's d_{yz} orbital to the PDOS at the bottom of the conduction band.	57
3.19 Variation of the difference in charge carriers' effective mass (holes minus electrons) with axial and shear strains for the twelve armchair and zigzag Janus TMH nanotubes.	58

SUMMARY

In the past three decades, the importance of nanotubes has significantly increased since the synthesis of carbon nanotubes. Among them, transition metal nanotubes, such as transition metal dichalcogenide (TMD) nanotubes, have gained attention due to their unique properties, including high tensile strength and mechanically tunable electronic properties, which make them ideal candidates for various applications such as reinforcement in nanocomposites, mechanical sensors, nanoelectromechanical (NEMS) devices, and biosensors. However, despite their potential, TMD nanotubes have not been thoroughly investigated for their elastic properties and electromechanical response, particularly concerning torsional deformations, using first-principles calculations. This is primarily due to the limitations imposed by standard periodic conditions, which require a large number of atoms.

TMD nanotubes are generally multi-walled with large diameters because of the relatively high energies required to bend their 2D material analogs. To address this issue, we introduce asymmetry in TMD nanotubes and form Janus TMD nanotubes, which are expected to exhibit unique and fascinating properties typically associated with quantum confinement effects. Moreover, Janus TMD nanotubes can form small single-walled nanotubes, thereby providing additional opportunities for their potential applications. Another promising class of transition metal nanotubes is transition metal dihalides (TMH), which have not yet been synthesized. However, due to the fascinating usage of their 2D analogs in piezoelectric-ferromagnetic, and ferrovalley materials, it is anticipated that TMH nanotubes will exhibit advantageous features similar to those of their 2D counterparts.

In this thesis, we employ symmetry-adapted DFT simulations to calculate the elastic properties of TMD and Janus TMD nanotubes, including Young's modulus, Poisson's ratio, and torsional modulus. Additionally, we investigate the electromechanical response of TMD nanotubes to torsional deformations and explore the behavior of Janus TMD and TMH nanotubes under axial and torsional deformations. Furthermore, we investigate the

effect of spin-orbit coupling on mechanically deformed TMD and Janus TMD nanotubes and observe Zeeman and Rashba spin-splitting, which are highly relevant for spintronics applications. Overall, our research provides valuable insights into the mechanical and electronic properties of these nanotubes, which could lead to their potential applications in a wide range of fields, such as electronics, spintronics, and sensors.

Our calculations reveal that the Young's and torsional moduli of TMD nanotubes follow the trend $MS_2 > MSe_2 > MTe_2$, while for Janus TMD nanotubes, the trend is $MSSe > MSTe > MSeTe$. Furthermore, TMD nanotubes are isotropic, while Janus TMD nanotubes are anisotropic, with the ordering being $MSTe > MSeTe > MSSe$. We also observe that strain engineering has little to no effect on metallic nanotubes, while it generally reduces the bandgap of semiconducting nanotubes, leading to semiconductor-to-metal transitions. This reduction in bandgap is typically observed to be linear with axial strain and quadratic with shear strain. Moreover, it results in a decrease in the effective mass of holes and an increase in the effective mass of electrons, leading to transitions from n-type to p-type semiconductors.

The TMD and Janus TMD nanotubes exhibit inversion symmetry, which leads to the absence of Rashba spin-splitting without any mechanical deformations. However, the introduction of twist in these nanotubes breaks the symmetry and induces Rashba spin-splitting, with relatively high values of the Rashba coefficient. We also investigate the Zeeman spin-splitting in these nanotubes under axial and shear strain. Our results reveal that the splitting values at the VBM (Valence Band Maximum) and CBM (Conduction Band Minimum) levels decrease monotonically, and in most cases of VBM with axial strain, it reaches 0. This is a crucial finding as the maximum splitting value at VBM is significant, reaching 0.46 eV in the WSe_2 nanotube before becoming zero with axial strain.

CHAPTER 1

INTRODUCTION

1.1 Background

The synthesis of carbon nanotubes around three decades ago [1] has revolutionized the fields of nanoscience and nanotechnology. Even in the specific instance of nanotubes — quasi-one-dimensional hollow cylindrical structures with diameters in the nanometer range — nearly two dozen nanotubes have now been synthesized [2, 3, 4], with the potential for thousands more given the large number of stable two-dimensional materials that have been predicted from first principles calculations [5, 6, 7]. Nanotubes have been the subject of intensive research, inspired by the novel and enhanced mechanical, electronic, optical, and thermal properties relative to their bulk counterparts [2, 3, 4]. In particular, a number of strategies have been developed to tune/engineer these properties, including chirality/radius [8, 9, 10, 11, 12, 13, 14, 15, 16, 17], defects [18, 19, 20], electric field [21, 22, 20], and mechanical deformations [23, 24, 25, 26, 9, 27, 28, 29, 30], highlighting the technological importance of nanotubes.

The transition metal dichalcogenide TMD group of nanotubes — materials denoted by MX_2 , where M and X are used to represent a transition metal and chalcogen, respectively — is the most diverse set, with the highest number of distinct nanotubes synthesized thus far [2, 3, 4]. This manifests itself into varying electronic properties encompassing semi-conducting [31, 32], metallic [33, 34], and superconducting [35, 36]. TMD nanotubes have a number of interesting properties including high tensile strength [37, 38, 39, 40], mechanically tunable electronic properties [41, 42, 43, 44, 45, 46, 47, 48, 49], and low cytotoxicity [50]. Also, a number of mechanisms have been found to tune/tailor the properties of TMD nanotubes, including chirality/radius [51, 52, 53, 54, 55, 56, 57, 58, 32, 47, 31], defects

[59, 60], temperature [35, 36], electric field [61, 62], and mechanical deformation [41, 42, 43, 44, 45, 46, 47, 48, 49]. These properties make TMD nanotubes suited to a number of applications, including reinforcement of composites [63, 64, 65, 66, 67, 68], nanoelectromechanical (NEMS) devices [69, 48, 70], medicine [71], photodetectors [72, 73, 74], mechanical sensors [75, 76, 42], biosensors [77], and superconductive materials [35, 36], where knowledge of their mechanical properties and electromechanical response is important from the perspective of both design and performance.

However, TMD nanotubes are generally multi-walled with large diameters — rationalized by the need for relatively high energies to bend their 2D material analogs [78] — limiting the appearance of unique and fascinating properties that are typically associated with quantum confinement effects. Furthermore, only a small percentage of all the potential TMD nanotubes have been synthesized thus far, in significant part to the nanotubes generally being energetically less favorable relative to their 2D counterparts. Janus TMD nanotubes [79] — materials denoted by MXY, where X and Y are used to represent two different chalcogens — do not suffer from the aforementioned limitations. In particular, the asymmetry in the system makes the rolled nanotube configuration energetically more favorable than the corresponding flat sheet [80, 81] — MoSSe and WSSe monolayers have recently been synthesized [82, 83, 84, 85] — significantly increasing the likelihood of single-walled small-diameter nanotubes with exotic properties/behavior. Therefore, at the very least, it is to be expected that Janus TMD nanotubes have similarly many applications as their non-Janus counterparts, including photodetectors [86, 42, 87, 88, 89, 90], nanoelectromechanical (NEMS) devices [69, 48, 70], biosensors [77], mechanical sensors [75, 76, 42], and superconductive materials [35, 36].

The Janus transition metal dihalide (TMH) nanotube group [91], which consists of materials of the form MXY, where X and Y are now different halogens, are likely to possess fascinating and exciting properties similar to those displayed in flat TMH monolayers [92] and their Janus variants, e.g., FeCl_2 is piezoelectric ferromagnetic with the Curie tempera-

ture around room temperature [93], and FeClBr and FeClF are ferrovalley materials based on their magnetic anisotropy [94, 95]. Simultaneously, the nanotubes inherit the aforementioned advantageous features of being a Janus structure.

1.2 Motivation

In view of the above, there have been a number of efforts to characterize the elastic properties of TMD nanotubes, both experimentally [96, 39, 97, 98] and theoretically [41, 44, 99, 100, 47, 101, 102, 103, 43, 76, 104]. However, these studies are limited to only a few TMDs, and that too only for the case of axial tension/compression. For Janus TMD nanotubes, apart from Ref. [105] where Young’s modulus of the MoSSe nanotube has been computed using DFT, the mechanical properties of Janus TMD nanotubes remain unexplored heretofore. In particular, determining the torsional moduli for these systems — relevant for applications such as resonators in NEMS devices [69, 48, 70] — has been limited to very few experimental [106, 70, 48] and theoretical [107, 108] research works, and that too only for a couple of materials. Indeed, the study of torsional deformations at practically relevant twists and nanotube diameters is intractable to ab initio methods like Kohn-Sham density functional theory (DFT) [109, 110] — expected to provide higher fidelity than tight binding and force field calculations for nanoscale systems — given the large number of atoms that are required when employing the standard periodic boundary conditions [111]. Therefore, accurate estimates for a fundamental mechanical property like torsional modulus is not available for TMD and Janus TMD nanotubes, which provides the motivation for the current work to compute the elastic properties of TMD and Janus TMD nanotubes.

Strain engineering represents an elegant and efficient way to control the electronic properties of TMD nanotubes, as shown experimentally [48] as well as theoretically from ab initio Kohn-Sham density functional theory (DFT) calculations [41, 42, 43, 44, 45, 46]. However, other than the experimental work referenced above, where the effect of both ten-

sile and torsional deformations have been studied for the WS_2 nanotube, research efforts have focused solely on tensile/compressive deformations, and that too for only a small fraction of the materials in the TMD nanotube group. Indeed, the study of torsional deformations at practically relevant twists and nanotube diameters requires large number of atoms when employing the standard periodic boundary conditions [111], which makes it intractable to first principles methods like Kohn-Sham DFT, given its cubic scaling with system size and large associated prefactor. Therefore, it provides the motivation for the current work to compute the electromechanical response of TMD nanotubes to torsional deformations.

There have been a number of ab initio studies to characterize the properties of Janus TMD nanotubes [112, 113, 114, 115, 87, 116, 91] and their electronic response to mechanical deformations [42, 105, 86, 117]. However, these investigations have been restricted to relatively few nanotubes, particularly in the case of electromechanical response, where only MoSSe has been studied to date. Even then, only the electronic response to axial deformations has been studied, with torsional deformations not considered. Also, apart from Ref. [42], the equilibrium diameter for the nanotube has not been considered in determining the electromechanical response. For TMH and Janus TMH nanotubes, we have not been able to find any kind of study in the literature. Overall, this gives us motivation to study the electronic response of Janus TMD and TMH nanotubes to axial and torsional deformations as it has not been comprehensively studied heretofore.

Spintronics has the potential for various interesting applications due to the effects of Rashba spin-splitting and Zeeman spin-splitting in various monolayers. Including spin-orbit coupling (SOC) in our calculations allows us to uncover these phenomena. However, in most studies related to the elastic property of materials, we do not consider SOC as it does not significantly affect the values. Similarly, in electromechanical response studies, we are usually more interested in comparing and analyzing trends between materials rather than obtaining the best values. Nonetheless, to examine the impact of SOC on electronic

band structures, we investigate them under mechanical deformation.

Zeeman spin-splitting and Rashba spin-splitting are both important phenomena in the context of spintronics. Zeeman spin-splitting occurs at the VBM (Valence Band Maximum) and CBM (Conduction Band Minimum) levels, where the eigenvalues split due to SOC, leading to changes in the bandgap and its structure. On the other hand, Rashba spin-splitting is observed in materials that lack inversion symmetry, and it typically occurs at the Gamma point. In the case of TMD and Janus TMD nanotubes, the inversion symmetry is present in their undeformed state, but it is broken when we apply twist, leading to the observance of Rashba effect. The role of twist in inducing Rashba spin-splitting is yet another application of this deformation mechanism in TMD nanotubes.

1.3 Organization

The remainder of this thesis is organized as follows. In chapter 2, we discuss the chosen TMD, Janus TMD and TMH nanotubes and describe the symmetry-adapted DFT simulations for calculation of their elastic properties, electromechanical and spintronic response to torsional/axial strains. Next, we present and discuss the results obtained in chapter 3. Finally, we provide concluding remarks and future work in chapter 4 and chapter 5 respectively.

CHAPTER 2

SYSTEMS AND METHODS

2.1 Transition metal dichalcogenide (TMD) nanotubes

2.1.1 Elastic properties

We consider the following single-walled TMD nanotubes with 2H-t symmetry [118, 119]: $M=\{V, Nb, Ta, Cr, Mo, W, Fe, Cu\}$ and $X=\{S, Se, Te\}$; and the following ones with 1T-o symmetry [118, 119]: $M=\{Ti, Zr, Hf, Mn, Ni, Pd, Pt\}$ and $X=\{S, Se, Te\}$. These materials have been selected among all the possible transition metal-chalcogen combinations as they have either been synthesized as single/multi-walled nanotubes [120, 121, 122, 123, 118, 124, 125, 126, 127] or the corresponding two-dimensional atomic monolayers have been predicted to be stable from ab initio calculations [5, 128, 129]. The radii for these nanotubes have been chosen so as to be commensurate with those that have been experimentally synthesized, and in cases where such data is not available, we choose radii commensurate with synthesized nanotubes that are expected to have similar structure.

We utilize the Cyclix-DFT code [111] — adaptation of the state-of-the-art real-space DFT code SPARC [130, 131, 132] to cylindrical and helical coordinate systems, with the ability to exploit cyclic and helical symmetry in one-dimensional nanostructures [111, 8, 133] — to calculate the torsional moduli of the aforementioned TMD nanotubes in the low twist limit. SPARC-X [130] is the latest iteration of the real-space density functional theory (DFT) code SPARC, which overcomes the quadratic scaling with respect to the number of atoms through a local real-space formulation of electrostatics [134, 135]. SPARC-X also employs the alternating Anderson-Richardson (AAR) method [136, 137] as a linear solver and uses a real-space preconditioner [138] to accelerate the convergence of the self-consistent field (SCF) iteration. Additionally, the restarted variant [139] of the Periodic

Pulay mixing scheme [140] is utilized to further enhance the convergence of the SCF iteration. These optimizations make SPARC-X a highly efficient and powerful tool for simulating complex systems with large numbers of atoms. Recent developments in machine-learned interatomic potentials [141, 142] and orbital-free density functional theory [143, 144, 145, 146] has the potential to accelerate the simulations while retaining the accuracy of first principle methods. However, these methods have not been applied to nanotubes or two-dimensional monolayers to study their bending properties.

Specifically, we consider three-atom unit cell/fundamental domains that have one metal atom and two chalcogen atoms, as illustrated in Figure 2.1. Indeed, such calculations are impractical without the symmetry adaption, e.g., a (57,57) MoS₂ nanotube (diameter ~ 10 nm) with an external twist of 2×10^{-4} rad/Bohr has 234, 783 atoms in the simulation domain when employing periodic boundary conditions, well beyond the reach of even state-of-the-art DFT codes on large-scale parallel machines [147, 148, 130]. It is worth noting that the Cyclix-DFT code has already been successfully employed for the study of physical applications [149, 150, 111, 78, 151, 49, 81, 152, 153, 154], which provides evidence of its accuracy.

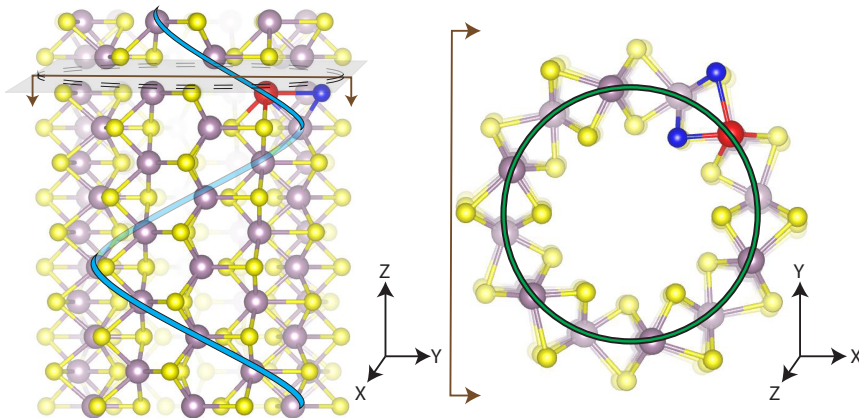


Figure 2.1: Illustration showing the cyclic and helical symmetry present in a twisted (6,6) TMD nanotube with 2H-t symmetry. In particular, all atoms in the nanotube can be considered to be cyclic and/or helical images of the metal and chalcogen atoms that have been colored red and blue, respectively. This symmetry is exploited while performing electronic structure simulations using the Cyclix-DFT code [111].

We employ optimized norm-conserving Vanderbilt (ONCV) [155] pseudopotentials from the SG15 [156] collection and the semilocal Perdew–Burke–Ernzerhof (PBE) [157] exchange-correlation functional. Apart from the tests by the developers [156], we have verified the transferability of the chosen pseudopotentials by comparisons with all-electron DFT code Elk [158] for select bulk systems. In addition, we have found that the equilibrium geometries of the nanotubes and their two-dimensional counterparts are in very good agreement with previous DFT results [5, 6, 44, 102, 43, 159, 160, 161, 129]. There is also very good agreement with experimental measurements [122, 35, 118, 120], confirming the suitability of the chosen exchange-correlation functional. Since we are interested in torsional moduli for the low-twist regime — corresponds to small (linear) perturbations of electron density from the undeformed nanotube — the use of more sophisticated functionals and/or inclusion of relativistic effects through spin orbit coupling (SOC) are not expected to change the results noticeably, especially considering that significant error cancellations occur while taking differences in energy. This is evidenced by the small differences in the ground state electron density between PBE and more sophisticated hybrid functionals for the TMD monolayer systems, even in the presence of SOC [78].

We calculate the torsional modulus in the low-twist regime by first performing ground state DFT simulations for various twisted configurations of the nanotube, and then fitting the data to the following quadratic relation:

$$\mathcal{E}(d, \theta) = \mathcal{E}(d, 0) + \frac{1}{2}K(d)\theta^2, \quad (2.1)$$

where K is the torsional modulus, d is the diameter of the nanotube, and θ and \mathcal{E} are the twist and ground state energy densities, respectively, i.e., defined per unit length of the nanotube. Indeed, small enough twists are chosen so that linear response is observed, i.e., the torsional modulus is independent of the twist. The other elastic properties : Young’s modulus, shear modulus and Poisson’s ratio will be described in the Result section. It

is important to note that the resulting shear strains — quantity that better describes the behavior/response of nanotubes, by allowing systematic comparison between tubes with different diameters — are commensurate with those found in torsion experiments [48, 70, 106]. All numerical parameters in Cyclix-DFT, including grid spacing, number of points for Brillouin zone integration, vacuum in the radial direction, and structural relaxation tolerances (both cell and atom) are chosen such that the computed torsional moduli are numerically accurate to within 1% of their reported value. In terms of the energy, this translates to the value at the structural and electronic ground state being converged to within 10^{-5} Ha/atom, a relatively stringent criterion that is necessary to capture the extremely small energy differences that occur at low values of twist.

2.1.2 Electromechanical response

We consider the same TMD nanotubes as in the case of elastic property calculations from previous subsection. Other parameters are also similar to the previous subsection. Indeed, PBE is known to under-predict the bandgap of TMD monolayers — expected to have similar band structure as the nanotubes, given that they have considerably large diameters where curvature effects are minor — relative to hybrid functionals like HSE [5]. However, there is good agreement in the overall band structure and nature of bandgap [5]. In particular, we are interested in general trends, which are expected to be insensitive to the choice of exchange-correlation functional, particularly given the small twists considered here. Even quantitatively, hybrid functionals are not necessarily more accurate than PBE in predicting the band structure, e.g., bulk TMDs [162]. In view of this and the tremendously larger cost associated with hybrids, PBE has been the functional of choice for TMD nanotubes [45, 58, 62, 44, 41, 54, 61, 60, 43, 46, 47]. Note that the incorporation of spin-orbit coupling (SOC) causes relatively minor modifications to the band structure [5], which is why it has been neglected here.

We perform the symmetry-adapted Kohn-Sham DFT calculations described above to

determine the variation in bandgap and effective mass of charge carriers (i.e., electrons and holes) with shear strain for the forty-five select armchair and zigzag TMD nanotubes. The shear strain is defined to be the product of the nanotube radius and the applied twist per unit length. The values for shear strain are chosen to be commensurate with those found in experiments [48, 70, 106]. Additional details regarding the calculation of the bandgap and effective mass within the symmetry-adapted formulation can be found in previous work [111]. The numerical parameters in Cyclix-DFT, including real-space grid spacing, Brillouin zone integration grid spacing, vacuum in the radial direction, and structural relaxation tolerances (both cell and atom) are chosen such that the bandgap and effective mass are calculated to within an accuracy of 0.01 eV and 0.01 a.u., respectively. This translates to the requirement of the ground state energy being converged to within 10^{-4} Ha/atom, respectively.

2.1.3 Spintronic properties: Rashba and Zeeman effect

We consider all the synthesized TMD nanotubes: $\{\text{MoS}_2, \text{MoSe}_2, \text{MoTe}_2, \text{WS}_2, \text{WSe}_2, \text{WTe}_2, \text{Nb}_2, \text{NbSe}_2, \text{Tas}_2\}$ with 2H-t symmetry [118, 119] and $\{\text{TiS}_2, \text{TiSe}_2, \text{HfS}_2, \text{Zr}_2\}$ with 1T-o symmetry [118, 119]. Other parameters are also similar to the previous subsection, except for the inclusion of spin-orbit coupling. Some preliminary tests for implementing spin-orbit coupling were performed in M-SPARC code [163, 164] which is the MATLAB version of SPARC code. We only consider the armchair variant as a few checks on representative cases show that the splitting values are independent of the chirality of nanotubes, also mentioned in this work [165].

We perform the symmetry-adapted Kohn-Sham DFT calculations described above to determine the Zeeman spin-splitting with axial and shear strain & Rashba spin-splitting coefficient with shear strain for the thirteen synthesized armchair TMD nanotubes. The numerical parameters in Cyclix-DFT, including real-space grid spacing, Brillouin zone integration grid spacing, vacuum in the radial direction, and structural relaxation tolerances

(both cell and atom) are chosen such that the Zeeman spin-splitting energy is calculated to within an accuracy of 0.01 eV. This translates to the requirement of the ground state energy being converged to within 10^{-4} Ha/atom, respectively.

2.2 Janus TMD nanotubes

2.2.1 Elastic properties

We consider the following single-walled Janus TMD nanotubes with 2H-t symmetry [118, 119]: $M=\{V, Nb, Ta, Cr, Mo, W\}$ and $X,Y=\{S, Se, Te\}$; and the following ones with 1T-o symmetry [118, 119]: $M=\{Ti, Zr, Hf\}$ and $X,Y=\{S, Se, Te\}$, in both armchair and zigzag configurations, with the heavier chalcogen on the outside in all cases. The chosen twenty-seven materials represent the set of all Janus TMD nanotubes that have previously been predicted to be thermodynamically stable [91]. The diameters for these nanotubes are selected so as to minimize the ground state Kohn-Sham energy [91], since experimentally synthesized nanotubes are likely to adopt energy minimizing configurations.

We perform simulations using the massively parallel real-space DFT code SPARC [130, 131, 132]. In particular, we employ the recently developed Cyclix-DFT feature [111], which provides a cyclic+helical symmetry-adapted formulation [111, 8, 133] and implementation [111] of the Kohn-Sham problem, enabling the simulation of Janus TMD nanotubes subject to axial and/or torsional deformations with only three atoms in the fundamental domain, i.e., one of each chemical element Figure 2.2. This provides a tremendous reduction in the cost, making many of the calculations performed here tractable, e.g., a (50,50) TiSTe nanotube with diameter ~ 10 nm subject to a twist of 5×10^{-4} rad/Bohr has 238,950 atoms in the periodic unit cell, a system size that is clearly beyond the reach of traditional DFT formulations/implementations due to the cubic scaling diagonalization bottleneck.

In all the simulations, we employ pseudopotentials from the SPMS collection [167], which is a set of transferable and soft optimized norm-conserving Vanderbilt (ONCV)

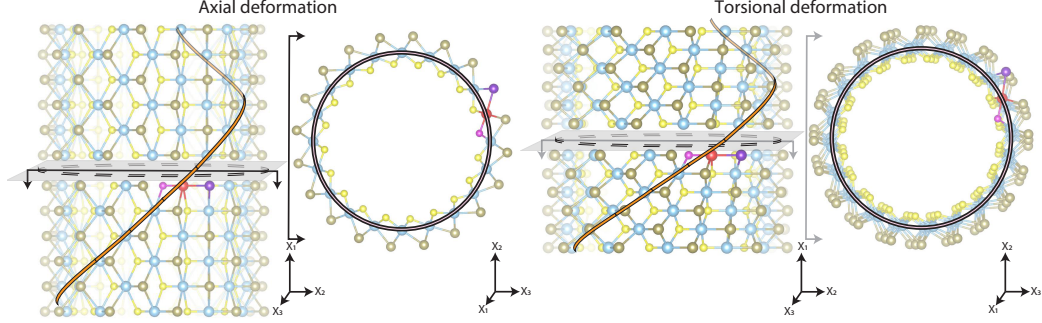


Figure 2.2: Illustration portraying the cyclic+helical symmetry inherent to Janus TMD nanotubes subject to axial/torsional deformations, using a (10,10) 1T-o symmetry nanotube as the representative example (structural model generated using VESTA [166]). In particular, the nanotube can be described by the symmetry operators and the positions of three atoms, e.g., metal and chalcogens colored red and violet/pink, respectively. This structural and resultant electronic symmetry is exploited while performing ab initio calculations using the Cyclix-DFT code [111, 130].

pseudopotentials [155] with nonlinear core correction (NLCC). The accuracy of the pseudopotentials in the current context is confirmed by the very good agreement of the computed equilibrium geometry with previous DFT results for Janus TMD nanotubes [117, 113, 86, 105, 91] as well as monolayers [5, 91, 168, 114]. We employ the semilocal Perdew–Burke–Ernzerhof (PBE) exchange–correlation functional [157], which is considered to accurately describe properties/behavior for TMD systems [5, 6, 44, 102, 43, 159, 160, 161, 129, 117, 113, 86, 105, 91, 168, 114], as validated by experimental measurements [122, 35, 118, 120, 169, 170, 171, 172, 173, 82, 83]. Indeed, the use of more advanced density functionals such as hybrids and/or inclusion of spin orbit coupling (SOC) are not expected to change the elastic properties noticeably, considering that the linear small-strain regime is accompanied by relatively small perturbations of electron density with respect to the undeformed nanotube, resulting in significant error cancellations while taking energy differences. This is expected to be particularly true in the current context, given that the difference in ground state electron density between PBE and hybrid functionals has been found to be relatively small for TMD monolayers, even in the presence of SOC [78].

We calculate the torsional modulus K , Young’s modulus E , and Poisson’s ratio ν by

fitting the data to the relations:

$$\mathcal{E}(\theta, \varepsilon^*(\theta), 0) \equiv \min_{\varepsilon} \mathcal{E}(\theta, \varepsilon, 0) = \mathcal{E}(0, 0, 0) + \frac{1}{2}K\theta^2, \quad (2.2)$$

$$\mathcal{E}(0, \varepsilon, \tilde{\varepsilon}^*(\varepsilon)) \equiv \min_{\tilde{\varepsilon}} \mathcal{E}(0, \varepsilon, \tilde{\varepsilon}) = \mathcal{E}(0, 0, 0) + \frac{1}{2}E\varepsilon^2, \quad (2.3)$$

$$\tilde{\varepsilon}^* = -\nu\varepsilon, \quad (2.4)$$

where $\mathcal{E}(\theta, \varepsilon, \tilde{\varepsilon})$ is the energy density — value at the electronic ground state corresponding to the force-relaxed atomic configuration — for twist density θ , axial strain ε , and circumferential/hoop strain $\tilde{\varepsilon}$, with both energy and twist densities defined to be per unit length of the nanotube. The superscript * is used to denote the value of the quantity that minimizes the energy density. The numerical parameters in the Cyclix-DFT simulations, including real-space grid spacing, reciprocal space grid spacing for Brillouin zone integration, radial vacuum, and cell/atom structural relaxation tolerances are selected to ensure that the torsional and Young's moduli are accurate to within 1% of their reported value. This translates to the ground state energy being accurate to within 10^{-5} Ha/atom, which is necessary to capture the exceedingly small energy differences that occur for the mechanical deformations considered in this work, which have been chosen to be small enough so as to have strains that are commensurate with those found in experiments [48, 70, 106, 38, 39].

2.2.2 Electromechanical response

We consider the following single-walled armchair and zigzag Janus TMD nanotubes at their equilibrium diameters [81]: (i) $M=\{\text{Ti, Zr, Hf}\}$, $X=\{\text{S, Se, Te}\}$, and $Y=\{\text{S, Se, Te}\}$, with 1T-o symmetry; and (ii) $M=\{\text{V, Nb, Ta, Cr, Mo, W}\}$, $X=\{\text{S, Se, Te}\}$, and $Y=\{\text{S, Se, Te}\}$, with 2H-t symmetry, the lighter chalcogen placed on the inner side of the nanotube in each case. These materials are chosen in the present work since they correspond to the full set of Janus TMD nanotubes predicted to be thermodynamically stable from Kohn-Sham DFT calculations [91]. To verify that these nanotubes are also mechanically stable,

given the exceedingly expensive nature of first principles stability calculations for such systems, we compute the phonon spectra for their monolayer counterparts using density functional perturbation theory (DFPT) feature in the planewave DFT code ABINIT [174]. The stability results so obtained are expected to be transferable to the nanotubes, given the relatively minor effects of curvature in large diameter nanotubes, and the stress-free configuration associated with the nanotube, i.e., the monolayer has bending stresses due to the asymmetry resulting from different chalcogens on either side, whereby the lowest phonon frequency for the equilibrium diameter nanotube is expected to be higher than the monolayer. From this study, the following nanotubes have been identified to be stable: $M=\{\text{Ti, Zr, Hf, Cr, Mo, W}\}$, $X=\{\text{S, Se, Te}\}$, and $Y=\{\text{S, Se, Te}\}$, the set of which will be the focus for the remainder of this work.

Other parameters are similar to the previous subsection, except the maximum values of axial and shear strains, which have been chosen such that the monolayer counterparts are still stable. These stability results are expected to be transferable to the nanotubes, as justified above. Note that in this work we do not focus on axial strains that are compressive, since nanotubes are prone to buckling-type instabilities at even small strain values, given the extremely large length to diameter ratios associated with nanotubes. Though PBE generally underpredicts the bandgap and is considered less reliable than hybrid functionals for computation of the band structure, the situation appears to be reversed for Janus TMD monolayers, a trend that is expected to hold for their nanotube counterparts as well. In particular, the bandgap for MoSSe monolayer computed here using PBE is in much better agreement with experiment than the Heyd–Scuseria–Ernzerhof (HSE) [175] hybrid functional. Specifically, the PBE and HSE values for MoSSe are 1.63 eV (Ref. [168]: 1.56 eV) and 1.95/2.23 eV [5, 116] respectively, with the experimental value being 1.48 eV [83]. Note that for Janus TMD monolayers, only minor modifications to the band structure have been observed upon the inclusion of spin-orbit coupling [5], hence we neglect it, expecting a similarly negligible effect for the nanotubes.

We use the above first principles framework to compute the change in bandgap and effective mass of charge carriers, i.e., electrons and holes, with axial and torsional deformations, for the aforementioned eighteen Janus TMD nanotubes, considering both the armchair and zigzag variants. Additional details regarding the computation of the bandgap and effective mass of charge carriers within the symmetry-adapted framework can be found in Ref. [111]. All the numerical parameters for Cyclix-DFT, including the grid spacing for real-space discretization and Brillouin zone integration, radial vacuum, and structural relaxation tolerances are chosen such that the ground state Kohn-Sham energy is converged to within 10^{-4} Ha/atom, which results in the bandgap and charge carriers' effective mass being accurate to within 0.01 eV and 0.01 a.u., respectively.

2.2.3 Spintronic properties: Rashba and Zeeman effect

We consider all the Janus combinations of Mo and W nanotubes: $\{\text{MoS}_2, \text{MoSe}_2, \text{MoTe}_2, \text{WS}_2, \text{WSe}_2, \text{WTe}_2\}$ with 2H-t symmetry. Janus variants of Mo and W's TMDs have been considered due to the synthesis of their monolayers and nanotubes[83, 84, 85, 176]. Other parameters are also similar to the previous subsection, except for the inclusion of spin-orbit coupling. We only consider the armchair variant as a few checks on representative cases show that the splitting values are independent of the chirality of nanotubes, also mentioned in this work [165].

We perform the symmetry-adapted Kohn-Sham DFT calculations described above to determine the Zeeman spin-splitting with axial and shear strain & Rashba spin-splitting coefficient with shear strain for the thirteen synthesized armchair TMD nanotubes. The numerical parameters in Cyclix-DFT, including real-space grid spacing, Brillouin zone integration grid spacing, vacuum in the radial direction, and structural relaxation tolerances (both cell and atom) are chosen such that the Zeeman spin-splitting energy is calculated to within an accuracy of 0.01 eV. This translates to the requirement of the ground state energy being converged to within 10^{-4} Ha/atom, respectively.

2.3 Janus Transition metal dihalide (TMH) nanotubes

2.3.1 Electromechanical properties

We consider zigzag and armchair variants of the following Janus TMH nanotubes: (i) $M=\{\text{Ti, Zr, Hf}\}$ and $X,Y=\{\text{Cl, Br, I}\}$, with 2H-t symmetry [118, 119]; and (ii) $M=\{\text{Fe}\}$ and $X,Y=\{\text{Cl, Br, I}\}$, with 1T-o symmetry [118, 119], all having the lighter halogen on the inner side. These represent the set of all Janus TMH nanotubes that have been predicted to be thermodynamically stable from first principles investigations [91].

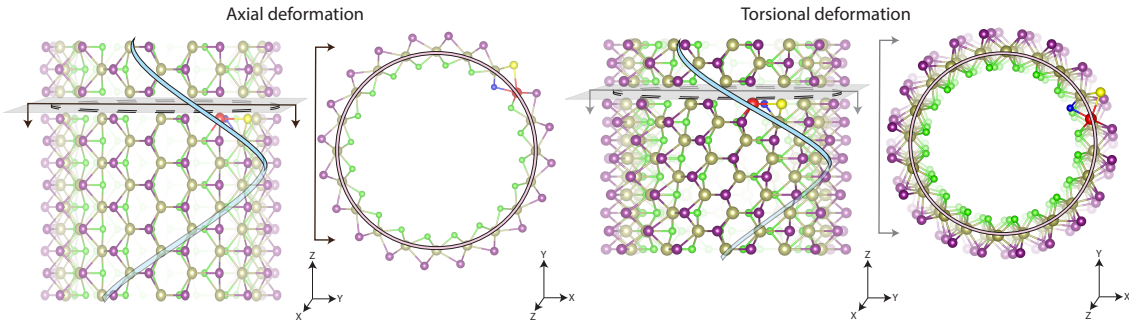


Figure 2.3: Illustration generated using VESTA [166] that depicts the inherent cyclic and helical symmetry of an axially and torsionally deformed (10,10) 1T-o Janus TMH nanotube. The entire nanotube can be generated using 3 atoms, e.g., metal and halogens colored red and blue/yellow, respectively, that lie within the cyclic+helical symmetry-adapted unit cell. This symmetry is exploited while performing Kohn-Sham DFT calculations using the electronic structure code SPARC’s Cyclix-DFT feature.

We perform all nanotube simulations using the Cyclix-DFT [111] feature — well tested in various physical applications [149, 150, 111, 78, 151, 49, 81, 152, 153] — in the state-of-the-art real-space DFT code SPARC [130, 131, 132]. In this formalism, as illustrated in figure Figure 2.1, the cyclic and/or helical symmetry of the system is exploited to reduce all computations to a unit cell that contains only a small fraction of the atoms in the traditional periodic unit cell [111, 8, 133], e.g., the periodic unit cell for a (45,45) HfClBr nanotube with diameter ~ 9 nm and an external twist of 6×10^{-4} rad/Bohr has 169, 155 atoms, whereas the cyclic+helical symmetry-adapted unit cell has only 3 atoms (one of each chemical element), a number that remains unchanged by axial and/or torsional defor-

mations. This symmetry-adaption provides tremendous computational savings, given that Kohn-Sham DFT computations scale cubically with system size.

Table 2.1: Equilibrium diameters in nm for the twelve armchair and zigzag Janus TMH nanotubes. The uncertainty in values accounts for the energy differences being smaller than the numerical accuracy in the calculations, i.e., 10^{-6} Ha/atom.

M	MCII		MBrI		MCIBr	
	Armchair	Zigzag	Armchair	Zigzag	Armchair	Zigzag
Ti	3.2 ± 0.2	3.2 ± 0.2	6.2 ± 0.4	6.0 ± 0.2	7.4 ± 0.4	7.8 ± 0.4
Zr	4.0 ± 0.2	3.8 ± 0.2	7.0 ± 0.4	6.6 ± 0.4	8.6 ± 0.8	8.8 ± 0.8
Hf	3.8 ± 0.2	3.8 ± 0.2	6.8 ± 0.4	6.8 ± 0.4	8.6 ± 0.6	8.6 ± 0.4
Fe	3.0 ± 0.2	2.8 ± 0.2	5.8 ± 0.2	6.0 ± 0.2	5.0 ± 0.4	4.8 ± 0.4

In all simulations, we employ the Perdew–Burke–Ernzerhof (PBE) [157] exchange-correlation functional, and scalar relativistic optimized norm-conserving Vanderbilt (ONCV) [155] pseudopotentials with nonlinear core correction from the SPMS collection [167]. The equilibrium configurations for the flat monolayer counterparts so obtained are in very good agreement with PBE results in literature [5], verifying the accuracy of the chosen pseudopotentials. Though PBE is known to generally underpredict the bandgap [5], it does provide good qualitative trends, making it a common choice for DFT calculations and Janus transition metal nanotubes in particular [112, 86, 113, 117, 115, 87, 105], motivating its selection here. Even quantitatively, sophisticated exchange-correlation functionals like hybrid are not necessarily more accurate for Janus materials [152]. Relativistic effects are neglected in all calculations, since only minor band structure modifications have been observed when spin-orbit coupling is incorporated for TMH and Janus TMD monolayers [5].

We set the diameter of each nanotube to be that which minimizes the ground state energy, the results for which are summarized in Table 2.1. All numerical parameters in Cyclix-DFT, including real-space grid spacing, k -point sampling for Brillouin zone, vacuum in the radial direction, and structural relaxation tolerances (both cell and atom) are chosen such that the lattice parameters and atomic positions are numerically converged to

within 0.01 bohr, which translates to the energy being accurate to within 10^{-6} Ha/atom. We find that the equilibrium diameters so computed are in good agreement with Ref. [91], the maximum difference of 0.6 nm occurring for the ZrClBr nanotube. The diameters follow the trend: $\text{MClI} < \text{MBrI} < \text{MClBr}$, which can be explained by the electronegativity difference in halogens, i.e., larger difference results in smaller equilibrium diameters, similar to Janus TMD nanotubes [152]. Interestingly, the stable symmetry (2H-t/1T-o) found in the present TMH nanotubes is opposite to that in TMD and Janus TMD nanotubes [49, 152]. We have also verified the mechanical stability of the flat TMH monolayers by computing their phonon spectra using the density functional perturbation theory (DFPT) feature in the ABINIT code [174]. These results suggest that the selected nanotubes are also mechanically stable, since the flat monolayer represents the stressed configuration (i.e, bending stresses) relative to the equilibrium diameter nanotube.

We calculate the variation in bandgap and effective mass of charge carriers (i.e., electrons and holes) with axial and shear strains using the procedure detailed in Ref. [111]. The axial strain is defined as the ratio of change in nanotube length to its original length, while the shear strain is defined as the product of the nanotube radius and the applied external twist per unit length. The strain values considered here are commensurate with those found in axial [38, 39] and torsion [48, 70, 106] experiments, with the maximum value decided by the mechanical stability of the flat configuration, as determined by DFPT calculations performed using ABINIT. We observe that the mechanically unstable strained monolayer suffers fracture in the XY plane by looking at the vibrations of the unstable mode. All numerical parameters in Cyclix-DFT, including those listed above, are chosen such that the bandgap and charge carriers' effective mass are numerically converged to within 0.01 eV and 0.01 a.u., respectively.

CHAPTER 3

RESULTS AND DISCUSSION

3.1 Transition metal dichalcogenide (TMD) nanotubes

3.1.1 Elastic properties

As described in the previous section, we utilize symmetry-adapted DFT simulations to calculate torsional moduli of the forty-five select armchair and zigzag TMD nanotubes. Observing a power law dependence of the torsional modulus with nanotube diameter d , we fit the data to the following relation:

$$K(d) = kd^\alpha + K(0), \quad (3.1)$$

where k and α will be henceforth referred to as the torsional modulus coefficient and exponent, respectively. The values so obtained for the different materials are presented in Table 3.1. Observing that the exponents are generally close to $\alpha = 3$, in order to enable comparison between the different materials that can have nanotubes with significantly different diameters, we also fit the data to the relation:

$$K(d) = \hat{k}d^3 + K(0), \quad (3.2)$$

where \hat{k} is referred to as the average torsional modulus coefficient. The results so obtained are presented through violin plots in Figure 3.1.

Table 3.1: Torsional modulus coefficient (k) and exponent (α) for the forty-five select armchair and zigzag TMD nanotubes.

M	Diameter range (nm)	MS ₂		MSe ₂		MTe ₂	
		Torsional modulus coefficient k (eV nm ^{1-α}) and exponent α		Torsional modulus coefficient k (eV nm ^{1-α}) and exponent α		Torsional modulus coefficient k (eV nm ^{1-α}) and exponent α	
		Armchair	Zigzag	Armchair	Zigzag	Armchair	Zigzag
W	2 - 10	267 (3.02)	256 (3.04)	226 (3.03)	230 (3.01)	179 (3.04)	158 (3.09)
Mo	2 - 10	232 (3.03)	213 (3.07)	197 (3.03)	175 (3.09)	150 (3.03)	143 (3.04)
Cr	6 - 10	194 (3.08)	222 (2.98)	171 (3.00)	178 (2.99)	135 (2.95)	191 (2.76)
V	6 - 10	161 (3.07)	170 (3.00)	149 (3.00)	133 (3.00)	98 (2.98)	92 (2.97)
Ta	14 - 40	158 (3.07)	205 (2.95)	176 (2.97)	160 (2.97)	165 (2.85)	155 (2.86)
Nb	2 - 14	133 (3.08)	181 (2.92)	140 (3.00)	162 (2.91)	90 (3.01)	66 (3.17)
Pt	6 - 10	154 (3.01)	156 (3.00)	127 (3.01)	129 (3.00)	133 (2.92)	259 (2.53)
Hf	6 - 30	162 (3.00)	165 (2.98)	136 (3.00)	135 (2.99)	93 (3.00)	85 (3.02)
Zr	6 - 30	149 (3.00)	160 (2.96)	125 (3.00)	127 (2.98)	98 (2.93)	84 (2.98)
Ti	2 - 10	140 (3.03)	153 (2.98)	106 (3.08)	127 (2.94)	75 (3.03)	83 (2.93)
Ni	6 - 10	147 (2.99)	147 (3.00)	127 (2.93)	120 (2.98)	136 (2.63)	156 (2.53)
Pd	6 - 10	114 (3.02)	119 (2.99)	94 (3.02)	100 (2.98)	107 (2.85)	223 (2.40)
Mn	6 - 10	108 (3.08)	122 (3.00)	39 (3.23)	29 (3.38)	27 (3.40)	52 (2.99)
Fe	6 - 10	60 (3.26)	49 (3.29)	102 (2.90)	157 (2.71)	76 (2.87)	109 (2.66)
Cu	6 - 10	30 (3.19)	32 (3.13)	27 (3.14)	49 (2.76)	35 (3.20)	102 (2.35)

We observe that the torsional modulus coefficients span around an order of magnitude between the different materials, with WS₂ and CuSe₂ having the largest and smallest values, respectively. Notably, even the largest value obtained here is nearly three times smaller than the carbon nanotube (733 eV/nm²) [111], which can be attributed to the extremely strong covalent carbon-carbon bonds. In comparison with experiments, where only the torsional

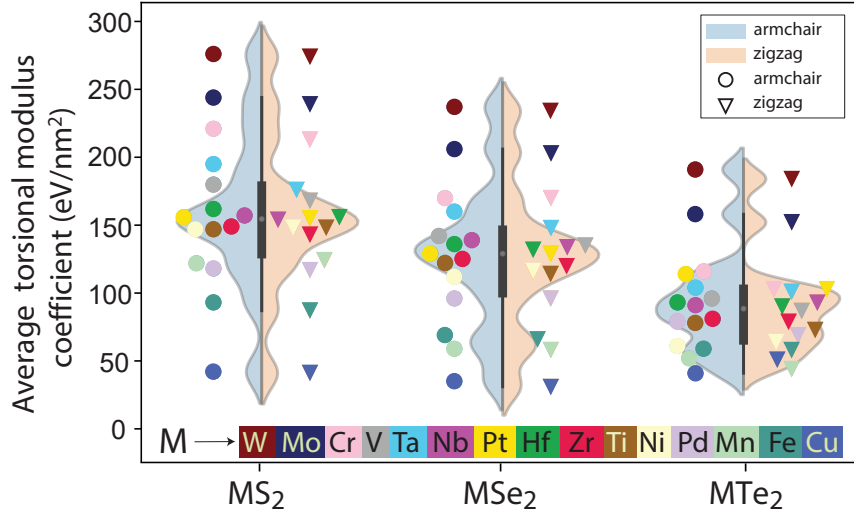


Figure 3.1: Average torsional modulus coefficient (\hat{k}) for the forty-five select armchair and zigzag TMD nanotubes.

modulus of WS₂ has been measured to date (384eV/nm²) [48], there is good agreement with the average torsional modulus coefficient reported here (275 eV/nm²). In particular, the computed value is well within the error bound communicated for the experimental result. In comparison with theoretical predictions, where only the values for MoS₂ are available from force field (armchair: 249 eV/nm² and zigzag: 243 eV/nm²) [108] and tight binding (armchair: 265 eV/nm² and zigzag: 265 eV/nm²) [107] simulations, there is good agreement with the average torsional modulus coefficients reported here (armchair: 244 eV/nm² and zigzag: 239 eV/nm²). Overall, we observe that the torsional moduli values generally follow the trend MS₂ > MSe₂ > MTe₂. This can be explained by the metal-chalcogen bond length having the reverse trend, with shorter bonds generally expected to be stronger due to the increase in orbital overlap.

We also observe from the results in Table 3.1 that the torsional modulus exponents are in the neighborhood of $\alpha = 3$, in agreement with the isotropic elastic continuum model [177]. In such an idealization, the shear modulus G can be calculated from the torsional modulus coefficient using the following relation derived from the continuum analysis of a

homogeneous isotropic circular tube subject to torsional deformations: ¹

$$G = \frac{4\hat{k}}{\pi}. \quad (3.3)$$

The results so obtained are presented in Figure 3.2. Note that since there are some noticeable deviations from $\alpha = 3$ (Table 3.1) — suggests that the shear modulus changes with diameter — the results in Figure 3.2 correspond to the case when \hat{k} is determined from the single data point corresponding to the largest diameter nanotube studied for each material. To verify their isotropic nature, we also determine the shear moduli of the nanotubes as predicted by the isotropic relation in terms of the Young’s modulus (E) and Poisson’s ratio (ν): $G = E/2(1 + \nu)$, both of which are also calculated using Cyclix-DFT, the results of which are summarized in Figure 3.2 and Table 3.2. It is clear that there is very good agreement between the computed and predicted shear moduli, suggesting that TMD nanotubes can be considered to be elastically isotropic.

We observe from the results in Figure 3.2 that the Young’s moduli follow a similar trend as the torsional modulus coefficients and therefore the shear moduli, which can be again explained by the strength of the metal-chalcogen bond, consistent with results obtained for molybdenum and tungsten TMD monolayers [180, 181, 182]. In regards to the Poisson’s ratio, we find that the MnS_2 , MnSe_2 , MnTe_2 , CrTe_2 , WTe_2 , MoTe_2 , TaTe_2 , and NiTe_2 nanotubes have a value near zero. In addition, the CuS_2 , CuSe_2 , CuTe_2 , VS_2 and FeS_2 nanotubes have ν greater than the isotropic theoretical limit of 0.5, which can be justified by the anisotropic nature of these materials — evidenced by the relatively poor agreement between the predicted and computed shear moduli (Figure 3.2) — where this bound is not applicable [183]. In regards to failure of these materials, it is possible to use Frantsevich’s rule [184] — materials with $\nu > 0.33$ and $\nu < 0.33$ are expected to be ductile and brit-

¹Since there is only a single parameter (i.e., shear modulus) in the continuum model, it can be determined from the average torsional modulus coefficient using Equation 4. In the case of discrete finite-element models of nanotubes[178, 179], which can provide significant computational efficiency relative to ab initio methods for studying mechanical behavior, a number of other DFT simulations would need to be performed to determine the force constants inherent to such models.

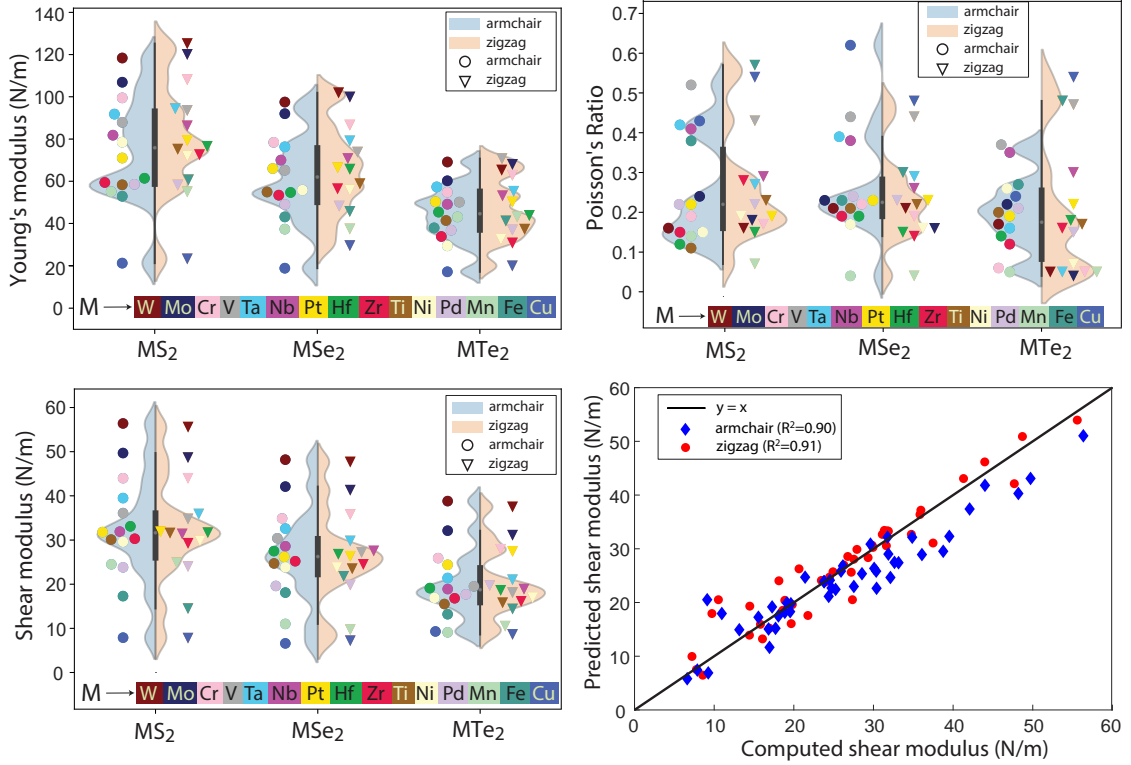


Figure 3.2: Young's modulus (E), shear modulus (G), and Poisson's ratio (ν) of the forty-five select armchair and zigzag TMD nanotubes. The predicted shear modulus refers to that obtained from the isotropic relation in terms of the Young's modulus and Poisson's ratio. The values of R^2 shown in the legend denotes the coefficient of determination for the linear regression. The results correspond to the largest diameter nanotube that has been studied for each material.

tle, respectively — to predict that $M=\{\text{Cu, Nb, Fe, Ta and V}\}$ nanotubes are ductile and $M=\{\text{W, Mo, Cr, Pt, Hf, Zr, Ti, Ni, Pd, Mn}\}$ are brittle. In particular, there is a clear divide between the Poisson's ratio of these two sets, as seen in Figure 3.2. Note that the computed Young's moduli and Poisson's ratio values are in good agreement with those available in literature [41, 107, 44, 99, 47, 103], further confirming the fidelity of the simulations performed here.

The above results indicate that the torsional moduli of TMD nanotubes are dependent on the nature and strength of the metal-chalcogen bond, which can be expected to depend on the bond length, difference in electronegativity between the atoms, and sum of their ionization potential and electron affinity. The first feature mentioned above is used to mainly capture the strength of the bond, and the other two features are used to mainly capture the nature of the bonding [185, 186, 187, 188]. Using these three features, we perform a linear regression on the set of average torsional modulus coefficients, the results of which are presented in Figure 3.3. The fit is reasonably good, suggesting that the features chosen here play a significant role in determining the torsional moduli of TMD nanotubes. Note that inclusion of the bond angle as a feature did not improve the quality of the fit, and therefore has been neglected here. Also note that though the quality of the fit can be further increased by using higher order polynomial regression, it can possibly lead to overfitting, and is hence not adopted here.

Table 3.2: Young's modulus (Y), shear modulus (G) and Poisson's ratio (ν) for the forty-five select armchair and zigzag Transition Metal Dichalcogenides (TMD) nanotubes from first principles DFT calculations

MX ₂	Young's modulus (N/m)		Shear modulus (N/m)		Poisson's ratio	
	Armchair	Zigzag	Armchair	Zigzag	Armchair	Zigzag
WS ₂	118.4	125.2	56.4	55.6	0.16	0.16
WSe ₂	97.5	101.9	48.2	47.7	0.21	0.21
WTe ₂	69.1	65.3	38.8	37.5	0.17	0.05
MoS ₂	106.9	120.1	49.7	48.7	0.24	0.18
MoSe ₂	92.0	99.9	42.1	41.3	0.23	0.16
MoTe ₂	60.2	68.0	32.1	31.1	0.22	0.04
CrS ₂	99.5	108.1	44.0	44.0	0.19	0.17
CrSe ₂	78.4	86.6	34.9	35.8	0.22	0.19
CrTe ₂	54.8	62.8	25.9	27.9	0.06	0.05
VS ₂	87.9	93.5	36.1	34.8	0.52	0.43
VSe ₂	65.2	73.8	30.4	27.2	0.44	0.44
VTe ₂	50.1	70.7	19.5	18.1	0.37	0.47
TaS ₂	91.8	94.4	39.5	35.9	0.42	0.27
TaSe ₂	76.3	79.1	32.6	29.8	0.39	0.29
TaTe ₂	57.3	55.2	21.4	21.0	0.16	0.05
NbS ₂	81.8	86.2	31.9	31.4	0.41	0.29
NbSe ₂	70.0	70.7	28.6	27.5	0.38	0.26
NbTe ₂	49.1	53.1	18.9	18.9	0.35	0.30
PtS ₂	78.5	79.3	31.8	31.7	0.22	0.19
PtSe ₂	66.0	66.4	26.2	26.3	0.23	0.23
PtTe ₂	50.3	50.1	24.4	27.4	0.19	0.22
HfS ₂	61.4	76.5	33.1	31.9	0.12	0.15
HfSe ₂	54.7	65.7	27.5	26.8	0.19	0.15
HfTe ₂	45.4	43.8	19.1	18.6	0.14	0.18
ZrS ₂	59.4	72.6	30.3	29.3	0.15	0.28
ZrSe ₂	53.4	56.4	25.2	24.5	0.19	0.14
ZrTe ₂	33.8	30.7	16.8	16.1	0.12	0.16
TiS ₂	58.5	75.2	30.1	31.6	0.11	0.23
TiSe ₂	54.9	58.8	24.7	23.5	0.21	0.22
TiTe ₂	41.4	37.3	15.5	15.8	0.20	0.17

Table 3.2 - *continued.*

MX ₂	Young's modulus (N/m)		Shear modulus (N/m)		Poisson's ratio	
	Armchair	Zigzag	Armchair	Zigzag	Armchair	Zigzag
NiS ₂	71.0	72.0	29.6	29.9	0.15	0.19
NiSe ₂	55.8	55.9	23.8	23.8	0.17	0.16
NiTe ₂	29.4	32.8	16.9	17.0	0.26	0.07
PdS ₂	58.3	58.2	23.8	24.0	0.22	0.22
PdSe ₂	49.0	48.2	19.6	19.8	0.24	0.23
PdTe ₂	36.8	36.9	17.7	19.7	0.21	0.15
MnS ₂	55.1	55.0	24.5	24.9	0.14	0.07
MnSe ₂	37.3	37.4	11.0	9.7	0.04	0.04
MnTe ₂	43.1	43.2	9.1	10.5	0.05	0.05
FeS ₂	52.9	60.7	17.3	14.5	0.38	0.57
FeSe ₂	43.1	45.7	18.1	21.8	0.23	0.30
FeTe ₂	37.9	41.2	13.2	14.4	0.27	0.48
CuS ₂	21.2	23.2	7.9	7.8	0.43	0.54
CuSe ₂	18.8	29.5	6.6	7.2	0.62	0.48
CuTe ₂	17.1	19.9	9.3	8.6	0.24	0.54

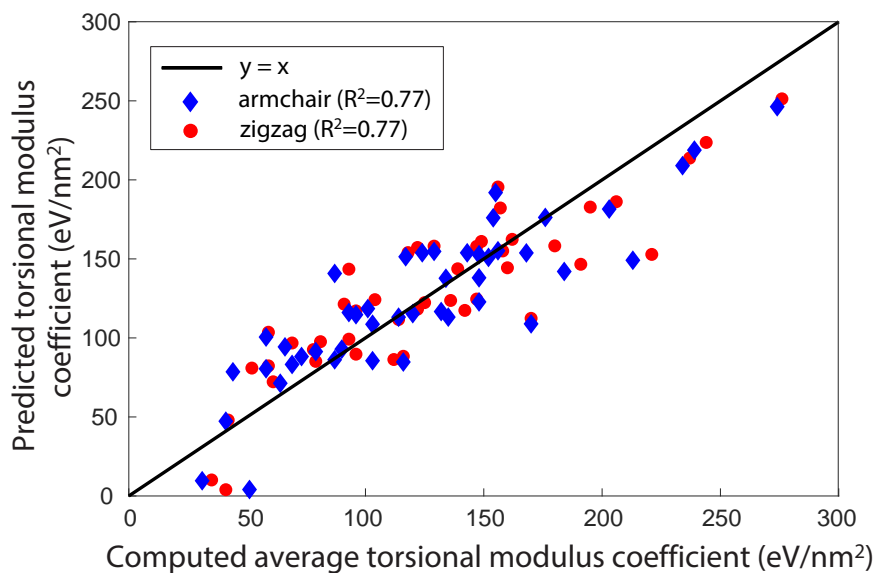


Figure 3.3: The set of computed average torsional modulus coefficients (\hat{k}) and its linear regression with the features being the metal-chalcogen bond length, difference in electronegativity between the metal and chalcogen atoms, and sum of the metal's ionization potential and chalcogen's electron affinity. The values of R^2 shown in the legend denotes the coefficient of determination for the linear regression.

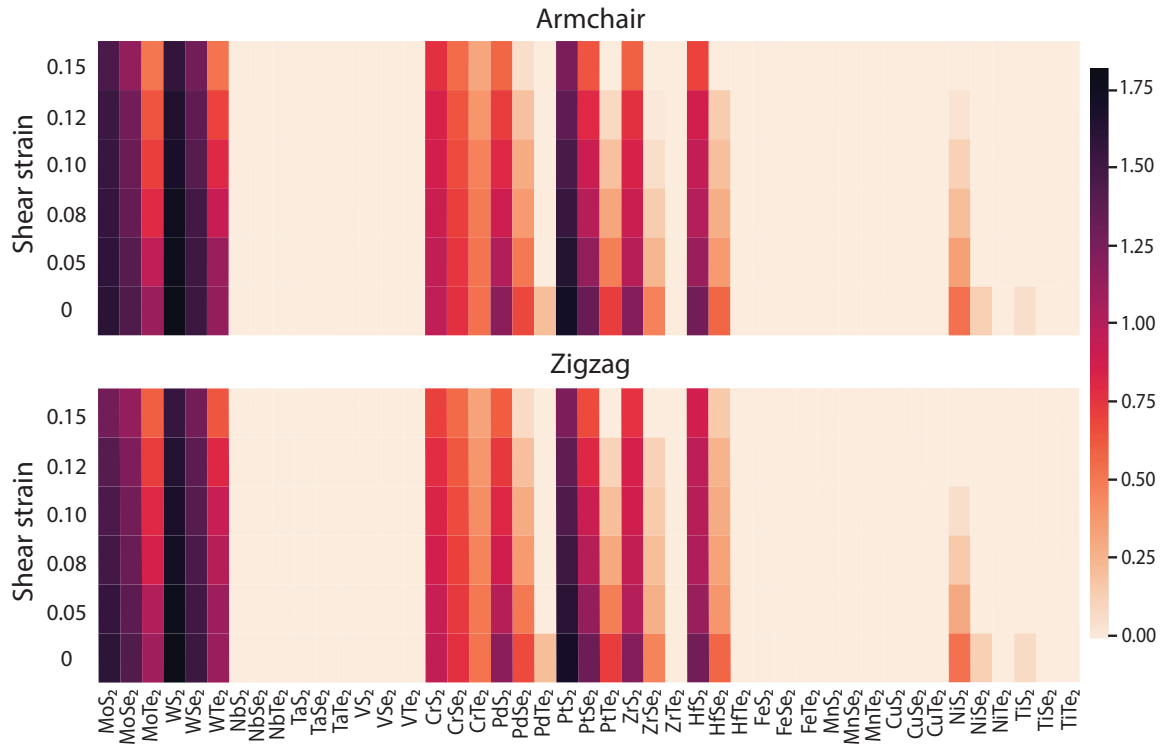


Figure 3.4: Variation of bandgap with twist for the forty-five select armchair and zigzag TMD nanotubes.

3.1.2 Electromechanical response

Table 3.3: Variation of bandgap with shear strain (γ) for the forty-five select TMD nanotubes. (D: direct bandgap, I: indirect bandgap).

MX ₂	Bandgap (eV)											
	Armchair						Zigzag					
	$\gamma = 0$	$\gamma = 0.05$	$\gamma = 0.08$	$\gamma = 0.10$	$\gamma = 0.12$	$\gamma = 0.15$	$\gamma = 0$	$\gamma = 0.05$	$\gamma = 0.08$	$\gamma = 0.10$	$\gamma = 0.12$	$\gamma = 0.15$
MoS ₂	1.60 (I)	1.58 (I)	1.56 (I)	1.54 (I)	1.53 (I)	1.45 (I)	1.6 (I)	1.57 (I)	1.50 (I)	1.46 (I)	1.41 (I)	1.29 (I)
MoSe ₂	1.44 (D)	1.41 (D)	1.35 (I)	1.32 (I)	1.29 (I)	1.15 (I)	1.44 (D)	1.39 (I)	1.33 (I)	1.29 (I)	1.24 (I)	1.15 (I)
MoTe ₂	1.11 (D)	0.97 (I)	0.80 (I)	0.72 (I)	0.65 (I)	0.52 (I)	1.10 (D)	1.03 (I)	0.87 (I)	0.81 (I)	0.73 (I)	0.61 (I)
WS ₂	1.82 (I)	1.78 (I)	1.76 (I)	1.69 (I)	1.65 (I)	1.57 (I)	1.83 (D)	1.78 (I)	1.73 (I)	1.69 (I)	1.65 (I)	1.56 (I)
WSe ₂	1.53 (D)	1.51 (D)	1.49 (D)	1.41 (I)	1.37 (I)	1.29 (I)	1.54 (D)	1.51 (I)	1.46 (I)	1.42 (I)	1.39 (I)	1.29 (I)
WTe ₂	1.14 (D)	1.11 (D)	0.92 (I)	0.81 (I)	0.71 (I)	0.53 (I)	1.12 (D)	1.11 (I)	1.01 (I)	0.93 (I)	0.82 (I)	0.65 (I)
NbS ₂	0	0	0	0	0	0	0	0	0	0	0	0
NbSe ₂	0	0	0	0	0	0	0	0	0	0	0	0
NbTe ₂	0	0	0	0	0	0	0	0	0	0	0	0
TaS ₂	0	0	0	0	0	0	0	0	0	0	0	0
TaSe ₂	0	0	0	0	0	0	0	0	0	0	0	0
TaTe ₂	0	0	0	0	0	0	0	0	0	0	0	0
VS ₂	0	0	0	0	0	0	0	0	0	0	0	0
VSe ₂	0	0	0	0	0	0	0	0	0	0	0	0
VTe ₂	0	0	0	0	0	0	0	0	0	0	0	0
CrS ₂	0.97 (D)	0.96 (D)	0.91 (I)	0.88 (I)	0.84 (I)	0.78 (I)	0.97 (D)	0.93 (I)	0.89 (I)	0.84 (I)	0.80 (I)	0.72 (I)
CrSe ₂	0.78 (D)	0.75 (I)	0.72 (I)	0.68 (I)	0.65 (I)	0.56 (I)	0.78 (D)	0.75 (I)	0.72 (I)	0.68 (I)	0.64 (I)	0.57 (I)
CrTe ₂	0.54 (D)	0.53 (D)	0.50 (D)	0.47 (D)	0.40 (I)	0.32 (I)	0.53 (D)	0.51 (I)	0.47 (I)	0.43 (I)	0.40 (I)	0.34 (I)
PdS ₂	1.18 (I)	1.02 (I)	0.90 (I)	0.81 (I)	0.73 (I)	0.59 (I)	1.18 (I)	1.01 (I)	0.90 (I)	0.82 (I)	0.74 (I)	0.62 (I)
PdSe ₂	0.69 (I)	0.51 (I)	0.38 (I)	0.30 (I)	0.20 (I)	0.06 (I)	0.69 (I)	0.51 (I)	0.38 (I)	0.30 (I)	0.21 (I)	0.08 (I)
PdTe ₂	0.22 (I)	0	0	0	0	0	0.22 (I)	0	0	0	0	0
PtS ₂	1.72 (I)	1.63 (I)	1.54 (I)	1.47 (I)	1.37 (I)	1.25 (I)	1.71 (I)	1.61 (I)	1.52 (I)	1.45 (I)	1.37 (I)	1.25 (I)
PtSe ₂	1.33 (I)	1.15 (I)	1	0.91 (I)	0.80 (I)	0.65 (I)	1.32 (I)	1.15 (I)	1.01 (I)	0.92 (I)	0.82 (I)	0.69 (I)
PtTe ₂	0.73 (I)	0.49 (I)	0.32 (I)	0.20 (I)	0.09 (I)	0	0.73 (I)	0.49 (I)	0.32 (I)	0.22 (I)	0.12 (I)	0
ZrS ₂	1.21 (I)	1.00 (I)	0.91 (I)	0.84 (I)	0.78 (I)	0.60 (I)	1.21 (I)	1.02 (I)	0.95 (I)	0.90 (I)	0.86 (I)	0.77 (I)
ZrSe ₂	0.47 (I)	0.25 (I)	0.15 (I)	0.07 (I)	0.01 (I)	0	0.47 (I)	0.28 (I)	0.22 (I)	0.16 (I)	0.13 (I)	0
ZrTe ₂	0	0	0	0	0	0	0	0	0	0	0	0

Table 3.3 - *continued*.

MX ₂	Bandgap (eV)											
	Armchair						Zigzag					
	$\gamma = 0$	$\gamma = 0.05$	$\gamma = 0.08$	$\gamma = 0.10$	$\gamma = 0.12$	$\gamma = 0.15$	$\gamma = 0$	$\gamma = 0.05$	$\gamma = 0.08$	$\gamma = 0.10$	$\gamma = 0.12$	$\gamma = 0.15$
HfS ₂	1.29 (I)	1.11 (I)	1.01 (I)	0.95 (I)	0.88 (I)	0.71 (I)	1.30 (I)	1.13 (I)	1.05 (I)	1.01 (I)	0.98 (I)	0.89 (I)
HfSe ₂	0.59 (I)	0.38 (I)	0.29 (I)	0.21 (I)	0.15 (I)	0	0.58 (I)	0.40 (I)	0.34 (I)	0.30 (I)	0.27 (I)	0.17 (I)
HfTe ₂	0	0	0	0	0	0	0	0	0	0	0	0
FeS ₂	0	0	0	0	0	0	0	0	0	0	0	0
FeSe ₂	0	0	0	0	0	0	0	0	0	0	0	0
FeTe ₂	0	0	0	0	0	0	0	0	0	0	0	0
MnS ₂	0	0	0	0	0	0	0	0	0	0	0	0
MnSe ₂	0	0	0	0	0	0	0	0	0	0	0	0
MnTe ₂	0	0	0	0	0	0	0	0	0	0	0	0
CuS ₂	0	0	0	0	0	0	0	0	0	0	0	0
CuSe ₂	0	0	0	0	0	0	0	0	0	0	0	0
CuTe ₂	0	0	0	0	0	0	0	0	0	0	0	0
NiS ₂	0.54 (I)	0.35 (I)	0.22 (I)	0.13 (I)	0.04 (I)	0	0.54 (I)	0.31 (I)	0.17 (I)	0.06 (I)	0	0
NiSe ₂	0.14 (I)	0	0	0	0	0	0.14 (I)	0	0	0	0	0
NiTe ₂	0	0	0	0	0	0	0	0	0	0	0	0
TiS ₂	0.06 (I)	0	0	0	0	0	0.08 (I)	0	0	0	0	0
TiSe ₂	0	0	0	0	0	0	0	0	0	0	0	0
TiTe ₂	0	0	0	0	0	0	0	0	0	0	0	0

Table 3.4: Variation of the effective mass of holes with shear strain (γ) for the nineteen semiconducting TMD nanotubes.

MX ₂	Effective mass of holes (a.u.)											
	Armchair						Zigzag					
	$\gamma = 0$	$\gamma = 0.05$	$\gamma = 0.08$	$\gamma = 0.10$	$\gamma = 0.12$	$\gamma = 0.15$	$\gamma = 0$	$\gamma = 0.05$	$\gamma = 0.08$	$\gamma = 0.10$	$\gamma = 0.12$	$\gamma = 0.15$
MoS ₂	5.10	4.45	3.86	3.50	0.55	0.52	4.32	4.38	4.27	4.20	4.03	3.74
MoSe ₂	0.65	0.63	0.63	0.62	0.61	0.60	0.64	0.66	0.67	0.61	0.62	0.65
MoTe ₂	0.72	0.68	0.63	0.63	0.66	0.76	0.73	0.41	0.34	0.33	0.32	0.34
WS ₂	4.10	0.42	0.41	0.41	0.40	0.39	0.44	0.40	0.40	0.40	0.40	0.39
WSe ₂	0.45	0.44	0.43	0.42	0.42	0.42	0.45	0.44	0.44	0.44	0.40	0.40
WTe ₂	0.44	0.43	0.44	0.42	0.43	0.44	0.46	0.44	0.26	0.25	0.23	0.22
CrS ₂	0.94	0.91	0.93	0.93	0.91	0.91	0.94	0.96	0.94	0.96	0.96	1.01
CrSe ₂	1.02	1.00	1.03	1.00	1.01	1.60	1.02	1.05	1.02	1.04	1.08	1.08
CrTe ₂	1.04	1.01	1.05	1.02	1.07	1.01	1.03	1.04	1.03	1.07	1.08	1.18
PdS ₂	2.45	1.77	1.41	1.28	1.20	1.10	3.17	1.58	1.24	1.09	0.97	0.83
PdSe ₂	1.64	0.70	0.67	0.66	0.65	0.63	1.48	0.65	0.57	0.53	0.49	0.45
PtS ₂	0.97	1.30	1.58	1.18	1.95	2.23	6.79	4.81	4.34	4.92	2.23	1.35
PtSe ₂	1.65	1.14	1.61	1.35	1.17	0.99	3.66	1.49	1.19	1.03	0.87	0.71
PtTe ₂	0.89	0.47	0.46	0.46	0.46	0.45	1.23	0.43	0.37	0.35	0.33	0.32
ZrS ₂	0.44	0.29	0.30	0.32	0.33	0.35	0.44	0.22	0.20	0.19	0.18	0.14
ZrSe ₂	0.30	0.19	0.20	0.21	0.22	0.23	0.29	0.13	0.11	0.10	0.09	0.06
HfS ₂	0.26	0.27	0.28	0.30	0.31	0.34	0.46	0.22	0.20	0.19	0.18	0.16
HfSe ₂	0.35	0.19	0.21	0.22	0.22	0.21	0.33	0.14	0.13	0.12	0.11	0.09
NiS ₂	5.02	0.60	0.59	0.58	0.59	0.59	2.17	0.57	0.53	0.50	0.49	0.48

Table 3.5: Variation of the effective mass of electrons with shear strain (γ) for the nineteen semiconducting TMD nanotubes.

MX ₂	Effective mass of electrons (a.u.)											
	Armchair						Zigzag					
	$\gamma = 0$	$\gamma = 0.05$	$\gamma = 0.08$	$\gamma = 0.10$	$\gamma = 0.12$	$\gamma = 0.15$	$\gamma = 0$	$\gamma = 0.05$	$\gamma = 0.08$	$\gamma = 0.10$	$\gamma = 0.12$	$\gamma = 0.15$
MoS ₂	0.47	0.47	0.50	0.50	0.50	0.55	0.48	0.46	0.46	0.48	0.49	0.50
MoSe ₂	0.56	0.56	0.58	0.59	0.58	0.59	0.55	0.56	0.53	0.54	0.55	0.62
MoTe ₂	0.63	0.63	0.66	0.65	0.64	0.70	0.62	0.61	0.67	0.60	0.60	0.61
WS ₂	0.32	0.33	0.33	0.34	0.34	0.34	0.32	0.33	0.32	0.32	0.32	0.33
WSe ₂	0.35	0.35	0.36	0.37	0.37	0.37	0.35	0.35	0.36	0.34	0.35	0.35
WTe ₂	0.35	0.35	0.46	0.37	0.36	0.35	0.35	0.34	0.34	0.28	0.33	0.33
CrS ₂	0.93	0.93	0.99	1.02	1.08	1.17	0.92	0.97	0.96	0.99	0.99	0.98
CrSe ₂	1.01	1.04	1.06	1.10	1.14	1.33	1.00	1.06	1.05	1.03	1.10	1.06
CrTe ₂	1.00	0.99	1.05	1.02	1.07	1.00	0.98	1.02	1.05	1.02	1.07	0.98
PdS ₂	0.30	0.30	0.30	0.31	0.31	0.30	0.45	0.46	0.45	0.45	0.45	0.43
PdSe ₂	0.22	0.22	0.22	0.22	0.21	0.21	0.21	0.28	0.27	0.26	0.26	0.24
PtS ₂	0.33	0.32	0.30	0.30	0.31	0.30	0.51	0.52	0.53	0.53	0.54	0.53
PtSe ₂	0.26	0.26	0.26	0.25	0.25	0.25	0.38	0.39	0.37	0.36	0.36	0.36
PtTe ₂	0.20	0.31	0.32	0.30	0.30	0.29	0.17	0.47	0.47	0.50	0.47	0.47
ZrS ₂	0.28	0.73	0.70	0.67	0.64	0.56	2.05	0.32	0.30	0.29	0.28	0.24
ZrSe ₂	0.19	0.50	0.45	0.40	0.37	0.36	0.26	0.21	0.20	0.18	0.17	0.15
HfS ₂	0.23	0.65	0.62	0.59	0.57	0.50	0.30	0.28	0.26	0.26	0.25	0.24
HfSe ₂	0.17	0.48	0.44	0.40	0.37	0.37	0.23	0.19	0.18	0.18	0.17	0.15
NiS ₂	0.28	0.26	0.26	0.25	0.25	0.24	0.26	0.34	0.32	0.31	0.31	0.30

In Figure 3.4, we present the variation of the bandgap with shear strain for the selected TMD nanotubes. We observe that the untwisted MoS₂, MoSe₂, MoTe₂, WS₂, WSe₂, WTe₂, CrS₂, CrSe₂, CrTe₂, PdS₂, PdSe₂, PdTe₂, PtS₂, PtSe₂, PtTe₂, ZrS₂, ZrSe₂, HfS₂, HfSe₂, NiS₂, NiSe₂, and TiS₂ nanotubes are semiconducting, while the remaining are metallic. In addition, nanotubes that are metallic continue to be so even after the application of twist, whereas semiconducting nanotubes undergo a decrease in bandgap value with twist — bandgaps that are originally direct become indirect — resulting in a semiconductor to metal transition. In particular, armchair HfSe₂, ZrSe₂, PtTe₂, NiS₂, TiS₂, NiSe₂, and PdTe₂; and zigzag ZrSe₂, PtTe₂, NiS₂, TiS₂, NiSe₂, and PdTe₂ nanotubes undergo a semiconductor to metal transition for the twists considered. The transition for TiS₂, NiSe₂, and PdTe₂

nanotubes occurs at substantially lower strains than the others, since the bandgaps in the untwisted state are smaller. Such transitions are also expected for the remaining semiconducting nanotubes, however the amount of twist required to achieve this can be significantly higher, at which point stability considerations become particularly important. Tunability of the bandgap and controlled semiconductor-metal transitions like those observed here have applications in devices such as mechanical sensors[75, 76, 42].

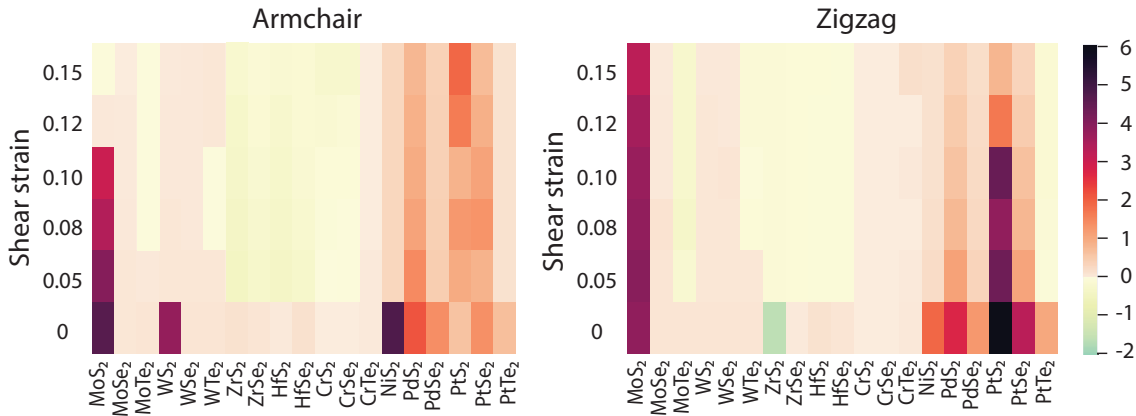


Figure 3.5: Variation of the difference in effective mass between holes and electrons (holes minus electrons) with twist for the nineteen semiconducting armchair and zigzag TMD nanotubes.

In Figure 3.5, we present the variation of the difference in effective mass between holes and electrons with twist for the nineteen semiconducting armchair and zigzag TMD nanotubes that were identified above. The effective mass of the holes and electrons relative to each other can be used to identify whether the nanotubes are n-type or p-type semiconductors. Specifically, the effective mass of the holes being greater than electrons suggests that the electrons have higher mobility, resulting in n-type semiconductors, with the reverse being true for p-type semiconductors. It is clear from the figure that other than the zigzag ZrS_2 nanotube, all other nanotubes are n-type semiconductors in their untwisted state. Upon the application of twist, the effective mass of the holes continuously decreases while that of the electrons continuously increases, leading to a crossover in their values. In particular, armchair MoS_2 , $MoTe_2$, WTe_2 , ZrS_2 , $ZrSe_2$, HfS_2 , $HfSe_2$, CrS_2 , and $CrSe_2$;

and zigzag MoTe_2 , WTe_2 , ZrSe_2 , HfS_2 , HfSe_2 , CrS_2 , CrSe_2 , and PtTe_2 nanotubes undergo a transition from n-type to p-type semiconducting behavior for the twists considered. Indeed, larger twists are likely to result in transitions for the other nanotubes as well, however, as mentioned above, stability considerations become particularly important in such scenarios. Controlled n-type to p-type semiconductor transitions like those observed here have applications in semiconductor switches [189, 190, 191, 192, 193, 194].

The results presented in this work are in good agreement with those available in literature. Specifically, in the untwisted state, the metallic nature predicted for TaS_2 , NbSe_2 , and NbS_2 nanotubes is in agreement with tight binding calculations [34, 195, 196, 33]; the bandgap values for MoS_2 , MoSe_2 , WS_2 , WSe_2 , and CrS_2 nanotubes are in good agreement with other DFT studies [44, 41]; and the effective masses of electrons for MoS_2 , WS_2 , and CrS_2 nanotubes are in good agreement with other DFT results [44, 43, 41]. In addition, the bandgap variation upon twisting for WS_2 and MoS_2 nanotubes is in good qualitative agreement with previous experiments and tight binding calculations, respectively [48]. A quantitative comparison cannot be made due to availability of only electrical response in the experiments, and the diameters in both experiments and tight binding simulations being different to those chosen here. Indeed, we have found that the bandgap variation with shear strain is qualitatively similar for different diameters. In view of this, we note that the ratio of change in bandgap between 15% and 10% shear strains for WS_2 nanotube is 2.1 based on experiments [48], which is in good agreement with the ratio of 1.9 obtained here for both armchair and zigzag variants. Furthermore, the ratio of bandgap between 15% and 0% strains for the armchair MoS_2 nanotube is 0.9 based on tight binding results [48], which is in excellent agreement with the value of 0.9 obtained here. It is interesting to note that metallic TMD nanotubes continue to be so even after the application of torsional deformations, which is fundamentally different from the response of carbon nanotubes [111].

To gain further insights into the results presented above, choosing representative TMD nanotubes that demonstrate semiconductor to metal and n-type to p-type transitions, we

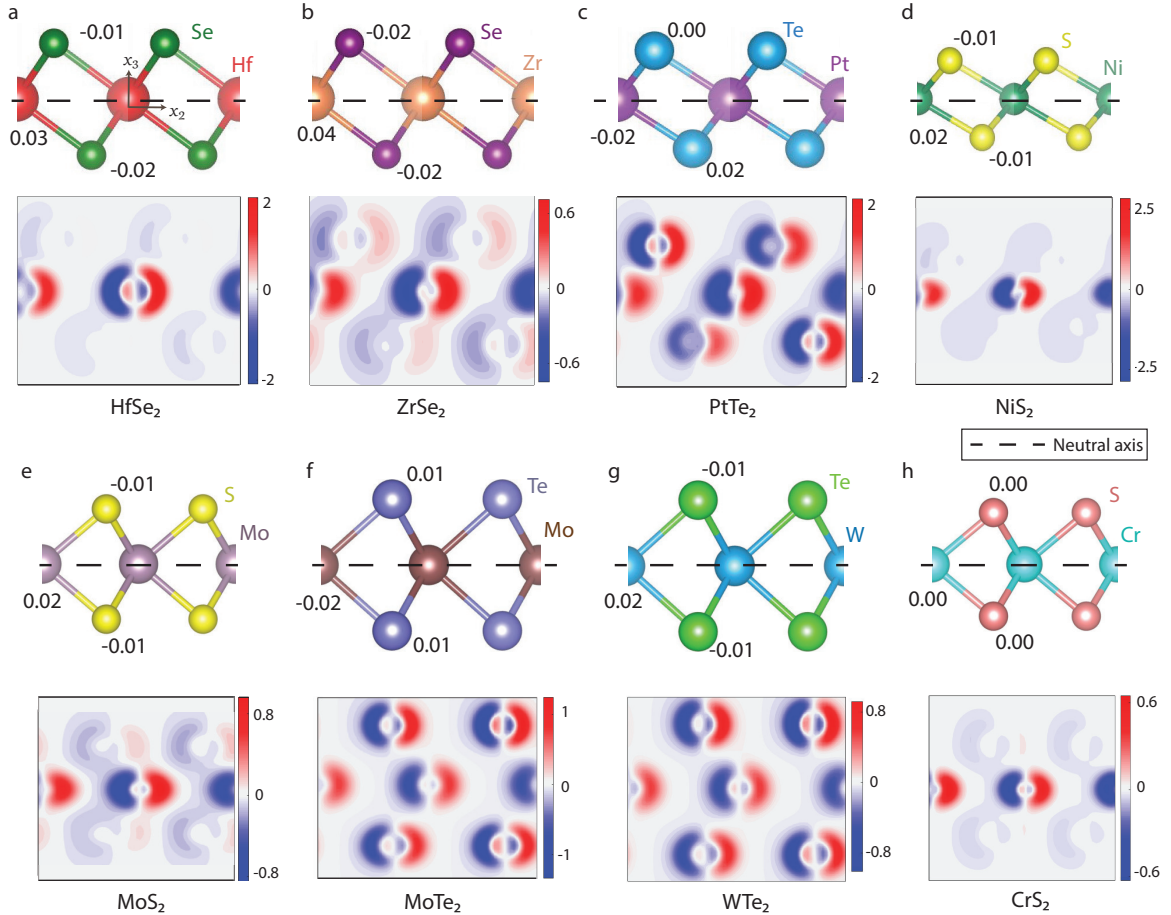


Figure 3.6: Contours of electron density difference — integrated along the x_1 direction — between the twisted and untwisted armchair nanotube configurations (twisted minus untwisted). The twists chosen for a, b, c, and d correspond to the semiconductor–metal transition; and in e, f, g, and h they correspond to the transition from n-type to p-type semiconductors. The contours are plotted on the x_2x_3 -plane in the corresponding monolayer flat sheet configuration. The charge transfer due to twisting, shown near the corresponding atoms in the lattice structure, is obtained from Bader analysis [197, 198].

plot the contours of electron density difference between the twisted and untwisted nanotube configurations in Figure 3.6. In addition, we compute the charge transfer due to torsional deformations using Bader analysis [197, 198]. We observe that there is negligible change in the Bader charge, suggesting the lack of charge transfer between the metal and chalcogen atoms, indicating that the nature of bonding between them remains unchanged. It can therefore be inferred that electronic variations due to torsional deformations, as visible through the change in electron density contours, is likely due to the rehybridization of orbitals in the metal and chalcogen atoms.

3.1.3 Spintronic properties: Rashba and Zeeman effect

We now present the spin-splitting results for TMD nanotubes with axial and shear strain. After introducing spin-orbital coupling (SOC), we find that there is no effect of it on the metallic nanotubes: NbS₂, NbSe₂, TaS₂ and TiSe₂. Also, we didn't observe any SOC effect in some other TMD nanotubes like TiS₂, HfS₂ and ZrS₂. Although, from Figure 3.7, we show the Zeeman spin-splitting in the remaining synthesized TMD nanotubes. We consider the splittings at both VBM (Valence Band Maximum) and CBM (Conduction Band Minimum) with axial and shear strain. We observe that the application of mechanical deformation usually results in a decrease in the splitting at VBM and CBM. The effect of SOC almost dissipates with axial strain at VBM, with splitting reaching 0. The values of VBM and CBM splitting at no mechanical deformation are almost similar to its 2d analogs [199], owing to the large enough diameter considered for the nanotubes. The trend of decrease in splitting is similar to the study on Janus TMD bilayers subjected to biaxial strains [200]

In Figure 3.8, the Rashba effect is not observed without any shear strain. It is consistent with our theory of the Rashba effect being present in only non-inversion-symmetry materials. As soon as we introduce shear strain (twist) in the nanotube, we break the inversion symmetry and we can see the Rashba coefficient continuously increasing with the strain.

The coefficient values at the highest strain are significant and can be used for spintronics applications. Note that we compute this change along momentum direction at the gamma point, similar to other Rashba effect studies [199, 200].

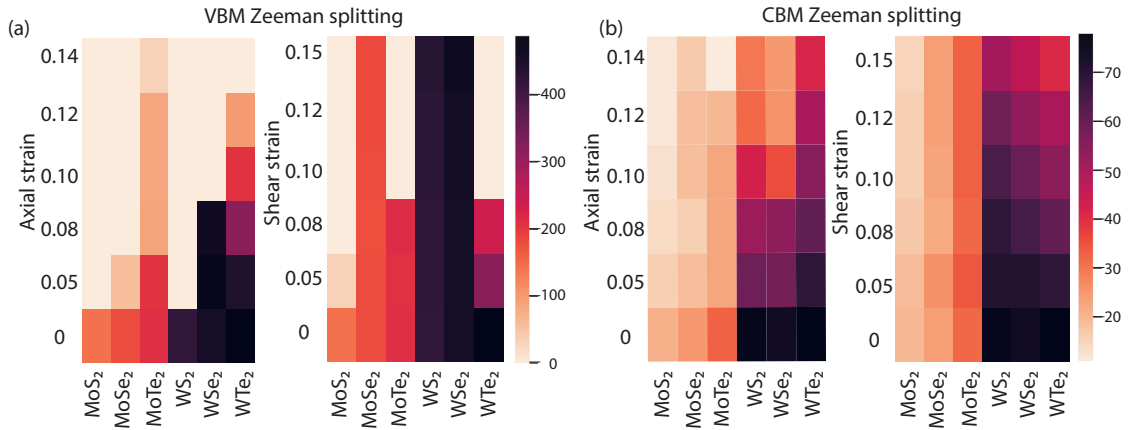


Figure 3.7: Zeeman spin splitting at (a) VBM (Valence Band Maximum) with axial and shear strain and (b) at CBM (Conduction Band Minimum) with axial and shear strain

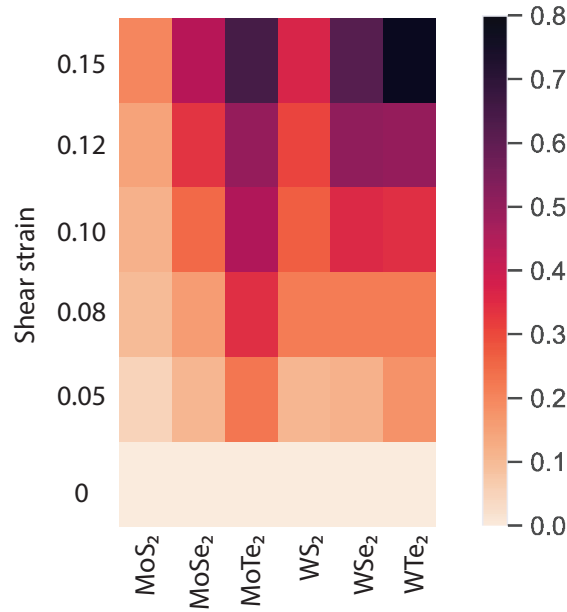


Figure 3.8: Rashba spin splitting coefficient at VBM (Valence Band Maximum) with shear strain (Gamma Point)

3.2 Janus TMD nanotubes

3.2.1 Elastic properties

As described in the previous section, we have performed symmetry-adapted Kohn-Sham DFT simulations to calculate the elastic properties of the twenty-seven select Janus TMD nanotubes, in both armchair and zigzag configurations, at their equilibrium diameters. The results so obtained have been summarized in Table 3.6 and Figure 3.9, which we discuss in detail below. Note that the results for the torsional moduli are reported in terms of the diameter-independent quantity referred to as the torsional modulus coefficient $\hat{k} = K/d^3$ [151], where d is the nanotube diameter. Also note that both the torsional and Young's moduli are reported in units of N/m rather than N/m^2 , since the latter requires an assumption on the thickness of the nanotube, whose value is not clearly defined [201].

The equilibrium radii generally follow the trend: $\text{MSTe} < \text{MSeTe} < \text{MSSe}$, which can be correlated to the difference in electronegativity between the chalcogens, i.e., larger electronegativity differences result in smaller equilibrium diameters, an observation that is in agreement with previous DFT results for $M=\{\text{Nb, Ta, Mo, W}\}$ and $X,Y=\{\text{S, Se, Te}\}$ [114]. The computed equilibrium diameters for these systems are also in excellent agreement with Ref [114], the maximum difference being 0.4 nm, which occurs for NbSSe. In terms of comparison with Ref. [91], which also employs DFT to predict the equilibrium diameters for all the materials studied here, while there is good agreement for nanotubes with smaller diameters, the difference increases with nanotube diameter, reaching a maximum of 22.8 nm for TiSeTe. This is a consequence of Ref. [91] using extrapolation from the data for small diameters — the current work employs interpolation, with data points on either side of the equilibrium diameter— whereby larger errors are accumulated when the equilibrium diameter is farther away from the region where Kohn-Sham calculations have actually been performed.

We observe from the results that the torsional modulus coefficients and the Young's

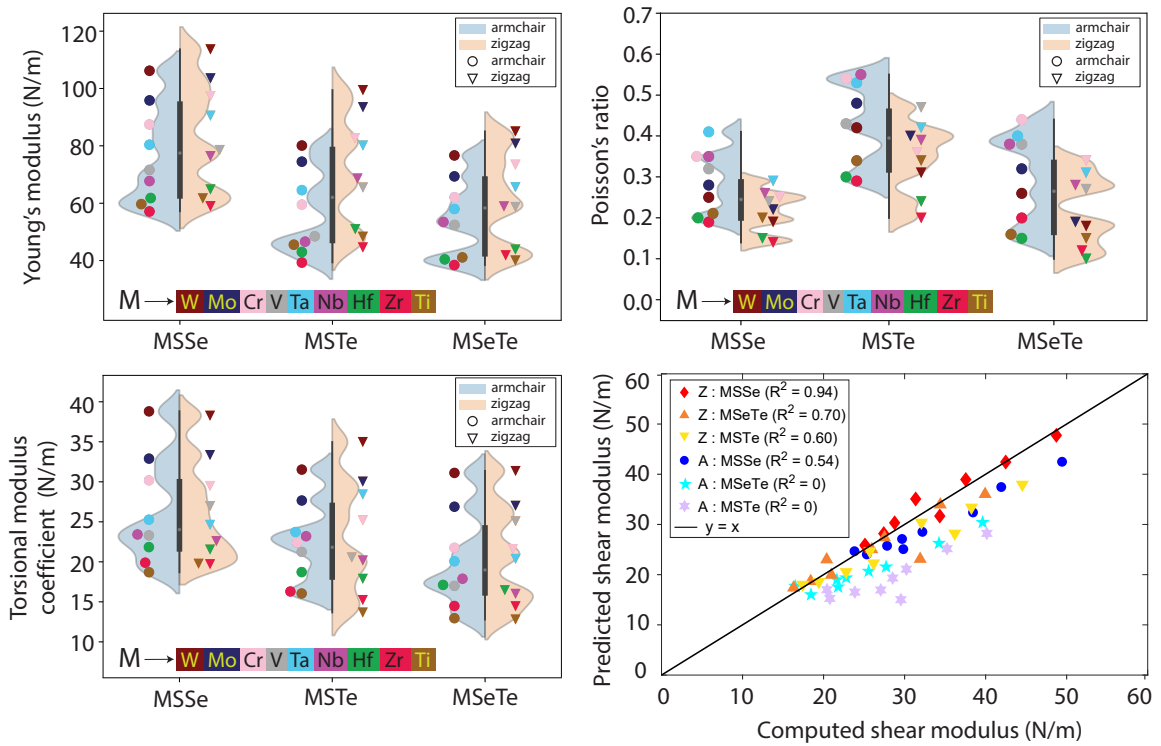


Figure 3.9: Torsional modulus coefficient (\hat{k}), Young's modulus (E), and Poisson's ratio (ν) for the twenty-seven select armchair and zigzag Janus TMD nanotubes. Also presented is the shear modulus computed from the torsional modulus coefficient vs. that predicted from the isotropic relation in terms of the Young's modulus and Poisson's ratio. The R^2 values listed in the legend represent the coefficient of determination for the linear regression.

Table 3.6: Young's modulus (E), Poisson's ratio (ν), and torsional modulus coefficient (\hat{k}) for the twenty-seven select Janus TMD nanotubes from first principles DFT calculations.

M	MSSe							
	Armchair				Zigzag			
	D (nm)	E (N/m)	ν	\hat{k} (N/m)	D (nm)	E (N/m)	ν	\hat{k} (N/m)
W	8.8 ± 0.5	106	0.25	39	9.0 ± 0.5	114	0.19	38
Mo	8.4 ± 0.2	96	0.28	33	8.3 ± 0.1	104	0.22	33
Cr	7.2 ± 0.3	87	0.35	30	7.5 ± 0.4	97	0.25	29
Ta	11.1 ± 1.5	80	0.41	25	11.2 ± 1.5	90	0.29	25
V	14.6 ± 2	72	0.32	23	14.2 ± 2.3	79	0.24	27
Nb	13.1 ± 1.4	68	0.35	23	14.1 ± 1.4	76	0.26	23
Hf	9.5 ± 0.5	62	0.20	22	10.4 ± 0.5	65	0.15	22
Zr	15.5 ± 3	57	0.19	20	14.9 ± 2.4	59	0.14	20
Ti	43.9 ± 5.9	60	0.21	19	44.9 ± 4.9	62	0.20	20
M	MSTe							
	Armchair				Zigzag			
	D (nm)	E (N/m)	ν	\hat{k} (N/m)	D (nm)	E (N/m)	ν	\hat{k} (N/m)
W	3.8 ± 0.1	80	0.42	32	3.8 ± 0.1	99	0.31	35
Mo	3.8 ± 0.1	74	0.48	28	3.8 ± 0.1	93	0.40	30
Cr	3.1 ± 0.1	60	0.54	22	3.1 ± 0.1	83	0.36	25
Ta	4.0 ± 0.1	65	0.53	24	4.1 ± 0.06	80	0.42	28
V	4.4	48	0.43	21	4.4 ± 0.06	65	0.47	21
Nb	4.4 ± 0.1	47	0.55	23	4.4 ± 0.1	69	0.39	20
Hf	4.4 ± 0.4	43	0.30	19	4.4 ± 0.4	51	0.24	18
Zr	6.1 ± 0.2	39	0.29	16	6.1 ± 0.2	45	0.20	15
Ti	10.0 ± 0.4	46	0.34	16	9.7 ± 0.6	48	0.34	14
M	MSeTe							
	Armchair				Zigzag			
	D (nm)	E (N/m)	ν	\hat{k} (N/m)	D (nm)	E (N/m)	ν	\hat{k} (N/m)
W	6.7 ± 0.1	77	0.26	31	7.1 ± 0.1	85	0.18	31
Mo	6.6 ± 0.3	69	0.32	27	6.5 ± 0.3	81	0.19	27
Cr	5.6 ± 0.2	62	0.44	22	5.6 ± 0.1	73	0.34	22
Ta	7.6 ± 0.3	58	0.40	20	7.6 ± 0.2	66	0.31	20
V	8.4 ± 0.6	52	0.38	17	8.2 ± 0.5	59	0.27	25
Nb	8.7 ± 0.8	53	0.38	18	8.9 ± 0.8	59	0.28	16
Hf	8.2 ± 0.5	40	0.15	17	8.1 ± 0.6	44	0.10	16
Zr	16.6 ± 3	38	0.20	14	15.8 ± 2.2	42	0.12	14
Ti	39.3 ± 10.9	41	0.16	13	28.7 ± 4.9	40	0.15	13

moduli for the Janus TMD nanotubes lie between the corresponding values for the parent TMD nanotubes [151]. In addition, we find that they follow the trend: MSSe > MSTe > MSeTe, which is the reverse of that for the metal-chalcogen bond lengths. Indeed, shorter bonds are expected to be stronger, due to the increase in overlap of the orbitals. In terms of individual values, WSSe and TiSeTe have the largest and smallest torsional modulus

coefficients, respectively, while WSSe and ZrSeTe have the largest and smallest Young's moduli, respectively. Notably, even the largest values obtained here are nearly a factor of 3 smaller than those for the carbon nanotube ($\hat{k} = 117$ N/m [111] and $E = 345$ N/m [202]), a likely consequence of the very strong covalent carbon-carbon bonds. In regards to the Poisson's ratio, we find that the armchair CrSTe, TaSTe, NbSTe nanotubes have values greater than the isotropic theoretical limit of 0.5 [183], which suggests their anisotropic nature, a result that we further confirm below. Note that we are not aware of any theoretical or experimental results in literature against which we can compare the values reported in this work. Indeed, the predictions made for MoSSe in Ref. [105] cannot be compared, given the significantly smaller diameter chosen there compared to the equilibrium value used here.

We also observe from the results that anisotropy with respect to armchair and zigzag configurations follows the ordering: $MSTe > MSeTe > MSSe$, which can likely be attributed to the level of dissimilarity between the chalcogens. To confirm this, we compute the effective shear modulus using the relation $G = 4\hat{k}/\pi$, which corresponds to the nanotube being modeled as a homogeneous isotropic circular tube subject to an external twist, and compare it against that predicted by the isotropic relation featuring the Young's modulus and Poisson's ratio: $G = E/2(1 + \nu)$. The results so obtained are summarized in Figure 3.9, from which it is clear that the disagreement between the computed and predicted shear moduli follows the same trend as that stated above for the difference in values between armchair and zigzag configurations, indicative of the relative degree of anisotropy between the different groups. In addition, the armchair nanotubes are significantly more anisotropic compared to their zigzag counterparts.

The above results indicate that the nature/strength of the metal-chalcogen bonds as well as the level of dissimilarity between the chalcogen atoms plays a significant role in determining the torsional and Young's moduli of Janus TMD nanotubes. In view of this, we develop a regression model with the following features: metal-chalcogen bond lengths,

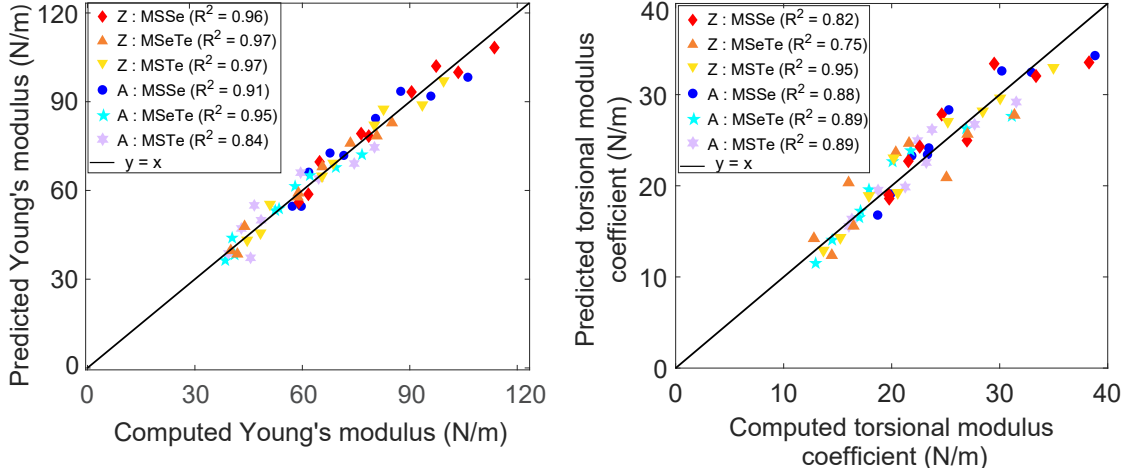


Figure 3.10: Computed elastic properties and their linear regression, with the features being the metal-chalcogen bond lengths, difference in electronegativity between the chalcogen atoms, and sum of the metal's ionization potential and chalcogens' electron affinity. The R^2 values listed in the legend represent the coefficient of determination for the linear regression.

difference in electronegativity between the chalcogens, and sum of the ionization potential and electron affinity for the metal and chalcogens, respectively. In particular, we perform a linear regression on the sets of torsional modulus coefficients and Young's moduli, the results of which are presented in Figure 3.10. The fit is reasonably good, which confirms that the chosen features play a significant role in determining the elastic properties for Janus TMD nanotubes. Note that higher order polynomial regression can be used to improve the quality of the fit, however this can possibly lead to overfitting, and hence not adopted here.

3.2.2 Electromechanical response

We now present and discuss the electronic response of the aforementioned Janus TMD nanotubes to axial/torsional deformations, from first principles, using the symmetry-adapted Kohn-Sham DFT framework described in the previous section. Wherever available, we compare the results obtained here with those in literature.

First, we summarize the variation of bandgap with axial and shear strains in Figure 3.11. We observe that the undeformed CrSSe, CrSeTe, CrSTe, MoSSe, MoSeTe, MoSTe, WSSe,

WSeTe, WSTe, ZrSSe, and HfSSe nanotubes are semiconducting, while the rest are metallic. In particular, bandgaps for MoSSe and MoSTe are in agreement with previous DFT studies [112, 86, 113, 114]. Upon deformation, the metallic nanotubes continue to remain metallic (behavior that distinguishes them from carbon nanotubes [203, 111]), whereas semiconducting nanotubes undergo a monotonic decrease in bandgap, the exceptions being HfSSe: bandgap increases with axial strain, and ZrSSe: bandgap first increases and then decreases with axial strain. Such tunability of bandgaps has a number of applications in nanotechnology, e.g., mechanical sensors [75, 76, 42]. Notably, both armchair and zigzag CrSTe nanotubes go through a semiconductor to metal transition within the range of axial strains considered. Indeed, for large enough axial/torsional deformations, such semiconductor to metal transitions are likely to occur for all the semiconducting nanotubes, though stability considerations become particularly important and therefore need to be considered/addressed. Note that on the application of compressive axial strains, the metallic nanotubes continue to remain metallic, three semiconducting nanotubes (MoSSe, WSSe, CrSSe) undergo an increase in bandgap, while the remaining eight undergo a decrease in bandgap, with the rate of bandgap variation being larger for compressive strains compared to tensile strains.

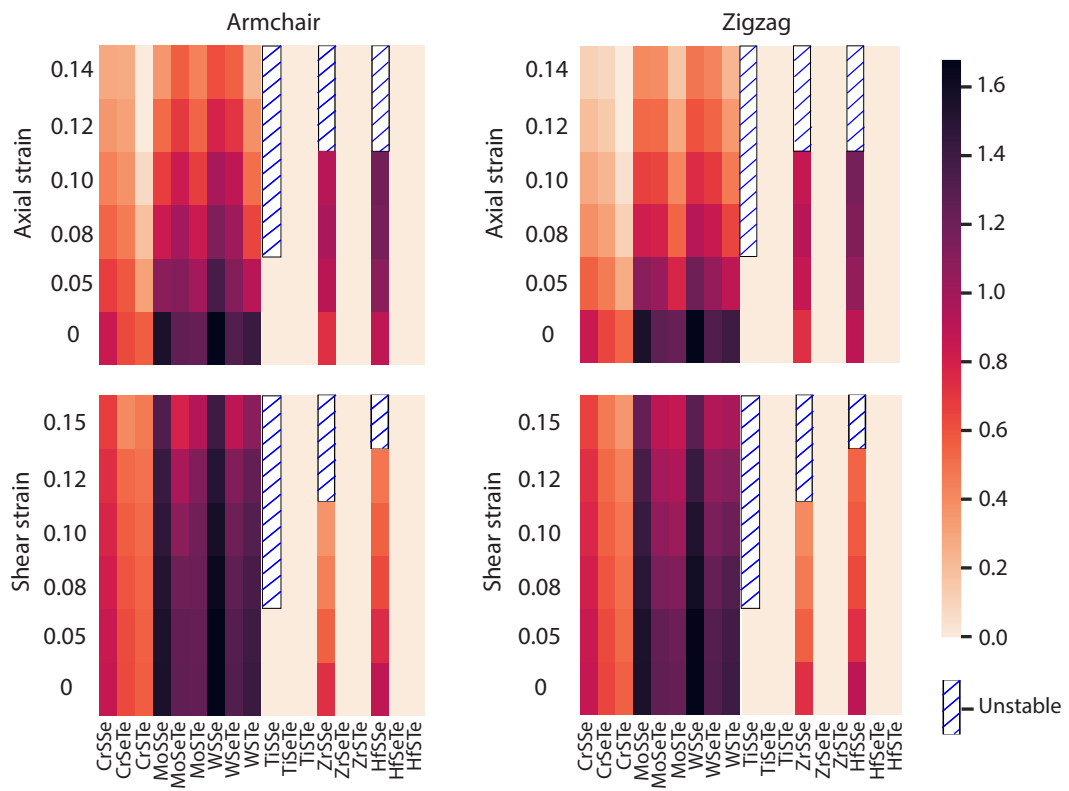


Figure 3.11: Variation of bandgap with axial and torsional deformations for the eighteen select armchair and zigzag Janus TMD nanotubes.

Table 3.7: Variation of bandgap with axial strain (ϵ) for the twenty-seven select Janus TMD nanotubes. (D: direct bandgap, I: indirect bandgap).

MXY	Bandgap (eV)											
	Armchair						Zigzag					
	$\epsilon = 0$	$\epsilon = 0.05$	$\epsilon = 0.08$	$\epsilon = 0.10$	$\epsilon = 0.12$	$\epsilon = 0.14$	$\epsilon = 0$	$\epsilon = 0.05$	$\epsilon = 0.08$	$\epsilon = 0.10$	$\epsilon = 0.12$	$\epsilon = 0.14$
TiSSe	0	0	0	0	0	0	0	0	0	0	0	0
TiSTe	0	0	0	0	0	0	0	0	0	0	0	0
TiSeTe	0	0	0	0	0	0	0	0	0	0	0	0
HfSSe	0.89 (D)	1.11 (D)	1.16 (D)	1.19 (D)	1.21 (D)	1.21 (D)	0.90 (I)	1.06 (I)	1.13 (I)	1.17 (I)	1.15 (I)	1.06 (I)
HfSTe	0	0	0	0	0	0	0	0	0	0	0	0
HfSeTe	0	0	0	0	0	0	0	0	0	0	0	0
ZrSSe	0.73 (I)	0.91 (I)	0.98 (I)	0.92 (I)	0.86 (I)	0.81 (I)	0.74 (I)	0.87 (I)	0.92 (I)	0.86 (I)	0.98 (I)	1.13 (I)
ZrSTe	0	0	0	0	0	0	0	0	0	0	0	0
ZrSeTe	0	0	0	0	0	0	0	0	0	0	0	0
CrSSe	0.86 (I)	0.68 (I)	0.54 (I)	0.44 (I)	0.36 (I)	0.29 (I)	0.86 (I)	0.56 (I)	0.39 (I)	0.29 (I)	0.20 (I)	0.12 (I)
CrSTe	0.57 (I)	0.32 (I)	0.19 (I)	0.08 (I)	0	0	0.56 (I)	0.27 (I)	0.12 (I)	0.05 (I)	0	0
CrSeTe	0.65 (D)	0.59 (D)	0.46 (I)	0.38 (I)	0.32 (I)	0.28 (I)	0.65 (I)	0.46 (I)	0.32 (I)	0.23 (I)	0.15 (I)	0.09 (I)
MoSSe	1.56 (I)	1.10 (I)	0.84 (I)	0.68 (I)	0.52 (I)	0.36 (I)	1.56 (I)	1.10 (I)	0.82 (I)	0.67 (I)	0.53 (I)	0.41 (I)
MoSTe	1.25 (I)	1.00 (I)	0.84 (I)	0.68 (I)	0.55 (I)	0.44 (I)	1.24 (I)	0.78 (I)	0.55 (I)	0.42 (I)	0.29 (I)	0.17 (I)
MoSeTe	1.27 (I)	1.12 (I)	1.00 (I)	0.84 (I)	0.70 (I)	0.57 (I)	1.26 (I)	1.04 (I)	0.80 (I)	0.65 (I)	0.52 (I)	0.40 (I)
WSSe	1.68 (D)	1.36 (I)	1.14 (I)	0.99 (I)	0.79 (I)	0.62 (I)	1.68 (I)	1.21 (I)	0.92 (I)	0.75 (I)	0.61 (I)	0.49 (I)
WSTe	1.42 (I)	0.92 (I)	0.65 (I)	0.51 (I)	0.39 (I)	0.23 (I)	1.41 (I)	0.89 (I)	0.65 (I)	0.47 (I)	0.35 (I)	0.23 (I)
WSeTe	1.32 (I)	1.12 (I)	1.02 (I)	0.89 (I)	0.71 (I)	0.56 (I)	1.32 (I)	1.05 (I)	0.85 (I)	0.69 (I)	0.55 (I)	0.43 (I)
VSSe	0	0	0	0	0	0	0	0	0	0	0	0
VSTe	0	0	0	0	0	0	0	0	0	0	0	0
VSeTe	0	0	0	0	0	0	0	0	0	0	0	0
NbSSe	0	0	0	0	0	0	0	0	0	0	0	0
NbSTe	0	0	0	0	0	0	0	0	0	0	0	0
NbSeTe	0	0	0	0	0	0	0	0	0	0	0	0
TaSSe	0	0	0	0	0	0	0	0	0	0	0	0
TaSTe	0	0	0	0	0	0	0	0	0	0	0	0
TaSeTe	0	0	0	0	0	0	0	0	0	0	0	0

Table 3.8: Variation of the effective mass of electrons with axial strain (ϵ) for the eleven semiconducting Janus TMD nanotubes.

MXY	Effective mass of electrons (a.u.)											
	Armchair						Zigzag					
	$\epsilon = 0$	$\epsilon = 0.05$	$\epsilon = 0.08$	$\epsilon = 0.10$	$\epsilon = 0.12$	$\epsilon = 0.14$	$\epsilon = 0$	$\epsilon = 0.05$	$\epsilon = 0.08$	$\epsilon = 0.10$	$\epsilon = 0.12$	$\epsilon = 0.14$
CrSSe	0.55	0.56	0.58	0.59	0.62	0.64	0.60	0.62	0.66	0.67	0.68	0.69
CrSTe	0.30	0.32	0.33	0.35	0.36	0.39	0.55	0.50	0.54	0.56	0.57	0.58
CrSeTe	0.80	0.80	0.82	0.84	0.84	0.81	0.51	0.58	0.65	0.71	0.73	0.75
MoSSe	0.38	0.39	0.44	0.46	0.50	0.51	0.27	0.28	0.29	0.33	0.37	0.39
MoSTe	0.50	0.54	0.55	0.56	0.62	0.65	0.23	0.24	0.29	0.31	0.35	0.34
MoSeTe	0.30	0.35	0.36	0.42	0.43	0.44	0.28	0.28	0.27	0.26	0.27	0.27
WSSe	0.18	0.18	0.19	0.20	0.21	0.21	0.14	0.16	0.17	0.17	0.18	0.16
WSTe	0.61	0.60	0.61	0.62	0.63	0.65	0.42	0.44	0.44	0.43	0.40	0.42
WSeTe	0.24	0.25	0.23	0.23	0.22	0.23	0.22	0.23	0.23	0.24	0.23	0.24
ZrSSe	0.31	0.33	0.33	0.34	0.36	0.38	0.30	0.31	0.35	0.36	0.34	0.33
HfSSe	0.50	0.58	0.59	0.61	0.60	0.61	0.33	0.36	0.36	0.41	0.40	0.40

Table 3.9: Variation of the effective mass of holes with axial strain (ϵ) for the eleven semiconducting Janus TMD nanotubes.

MXY	Effective mass of holes (a.u.)											
	Armchair						Zigzag					
	$\epsilon = 0$	$\epsilon = 0.05$	$\epsilon = 0.08$	$\epsilon = 0.10$	$\epsilon = 0.12$	$\epsilon = 0.14$	$\epsilon = 0$	$\epsilon = 0.05$	$\epsilon = 0.08$	$\epsilon = 0.10$	$\epsilon = 0.12$	$\epsilon = 0.14$
CrSSe	0.89	0.85	0.79	0.76	0.70	0.61	0.87	0.82	0.80	0.74	0.71	0.65
CrSTe	2.86	2.40	2.23	1.54	1.21	0.63	1.90	1.25	1.04	0.85	0.84	0.83
CrSeTe	1.72	1.64	1.23	1.17	1.01	0.75	0.94	0.81	0.73	0.71	0.70	0.72
MoSSe	0.58	0.52	0.52	0.50	0.44	0.45	0.57	0.50	0.49	0.49	0.47	0.36
MoSTe	2.31	1.63	1.34	1.11	0.71	0.62	1.03	0.63	0.51	0.37	0.33	0.32
MoSeTe	0.62	0.58	0.56	0.55	0.50	0.41	0.68	0.47	0.42	0.33	0.32	0.31
WSSe	0.38	0.36	0.36	0.37	0.37	0.36	0.40	0.41	0.38	0.38	0.37	0.35
WSTe	3.48	2.14	1.68	1.47	1.07	0.62	1.09	0.89	0.71	0.41	0.33	0.32
WSeTe	0.44	0.40	0.41	0.42	0.39	0.41	0.42	0.31	0.32	0.33	0.32	0.33
ZrSSe	0.51	0.44	0.42	0.34	0.36	0.34	0.21	0.20	0.21	0.20	0.21	0.22
HfSSe	0.62	0.58	0.57	0.56	0.55	0.58	0.73	0.33	0.30	0.32	0.30	0.31

Table 3.10: Variation of bandgap with shear strain (γ) for the twenty-seven select Janus TMD nanotubes. (D: direct bandgap, I: indirect bandgap).

MXY	Bandgap (eV)											
	Armchair						Zigzag					
	$\gamma = 0$	$\gamma = 0.05$	$\gamma = 0.08$	$\gamma = 0.10$	$\gamma = 0.12$	$\gamma = 0.15$	$\gamma = 0$	$\gamma = 0.05$	$\gamma = 0.08$	$\gamma = 0.10$	$\gamma = 0.12$	$\gamma = 0.15$
TiSSe	0	0	0	0	0	0	0	0	0	0	0	0
TiSTe	0	0	0	0	0	0	0	0	0	0	0	0
TiSeTe	0	0	0	0	0	0	0	0	0	0	0	0
HfSSe	0.89 (D)	0.75 (D)	0.64 (D)	0.56 (D)	0.48 (D)	0.36 (D)	0.90 (I)	0.73 (I)	0.64 (I)	0.58 (I)	0.54 (I)	0.48 (I)
HfSTe	0	0	0	0	0	0	0	0	0	0	0	0
HfSeTe	0	0	0	0	0	0	0	0	0	0	0	0
ZrSSe	0.73 (I)	0.56 (I)	0.45 (I)	0.37 (I)	0.30 (I)	0.22 (I)	0.74 (I)	0.55 (I)	0.47 (I)	0.41 (I)	0.37 (I)	0.37 (I)
ZrSTe	0	0	0	0	0	0	0	0	0	0	0	0
ZrSeTe	0	0	0	0	0	0	0	0	0	0	0	0
CrSSe	0.86 (I)	0.85 (I)	0.82 (I)	0.78 (I)	0.74 (I)	0.68 (I)	0.86 (I)	0.84 (I)	0.81 (I)	0.77 (I)	0.73 (I)	0.66 (I)
CrSTe	0.57 (I)	0.56 (I)	0.55 (I)	0.52 (I)	0.50 (I)	0.47 (I)	0.56 (I)	0.53 (I)	0.51 (I)	0.48 (I)	0.44 (I)	0.36 (I)
CrSeTe	0.65 (D)	0.64 (D)	0.61 (I)	0.57 (I)	0.53 (I)	0.41 (I)	0.65 (I)	0.64 (I)	0.60 (I)	0.56 (I)	0.53 (I)	0.47 (I)
MoSSe	1.56 (I)	1.55 (I)	1.52 (I)	1.47 (I)	1.43 (I)	1.33 (I)	1.56 (I)	1.55 (I)	1.49 (I)	1.43 (I)	1.36 (I)	1.24 (I)
MoSTe	1.25 (I)	1.24 (I)	1.22 (I)	1.19 (I)	1.13 (I)	0.93 (I)	1.24 (I)	1.22 (I)	1.13 (I)	1.03 (I)	0.95 (I)	0.86 (I)
MoSeTe	1.27 (I)	1.25 (I)	1.21 (I)	1.09 (I)	0.97 (I)	0.79 (I)	1.26 (I)	1.25 (I)	1.16 (I)	1.07 (I)	0.99 (I)	0.90 (I)
WSSe	1.68 (D)	1.67 (I)	1.64 (I)	1.58 (I)	1.51 (I)	1.40 (I)	1.68 (I)	1.67 (I)	1.61 (I)	1.53 (I)	1.43 (I)	1.28 (I)
WSTe	1.42 (I)	1.41 (I)	1.36 (I)	1.31 (I)	1.26 (I)	1.10 (I)	1.41 (I)	1.38 (I)	1.32 (I)	1.22 (I)	1.11 (I)	0.98 (I)
WSeTe	1.32 (I)	1.31 (I)	1.26 (I)	1.21 (I)	1.13 (I)	0.90 (I)	1.32 (I)	1.31 (I)	1.24 (I)	1.16 (I)	1.07 (I)	0.94 (I)
VSSe	0	0	0	0	0	0	0	0	0	0	0	0
VSTe	0	0	0	0	0	0	0	0	0	0	0	0
VSeTe	0	0	0	0	0	0	0	0	0	0	0	0
NbSSe	0	0	0	0	0	0	0	0	0	0	0	0
NbSTe	0	0	0	0	0	0	0	0	0	0	0	0
NbSeTe	0	0	0	0	0	0	0	0	0	0	0	0
TaSSe	0	0	0	0	0	0	0	0	0	0	0	0
TaSTe	0	0	0	0	0	0	0	0	0	0	0	0
TaSeTe	0	0	0	0	0	0	0	0	0	0	0	0

Table 3.11: Variation of the effective mass of electrons with shear strain (γ) for the eleven semiconducting Janus TMD nanotubes.

MXY	Effective mass of electrons (a.u.)											
	Armchair						Zigzag					
	$\gamma = 0$	$\gamma = 0.05$	$\gamma = 0.08$	$\gamma = 0.10$	$\gamma = 0.12$	$\gamma = 0.15$	$\gamma = 0$	$\gamma = 0.05$	$\gamma = 0.08$	$\gamma = 0.10$	$\gamma = 0.12$	$\gamma = 0.15$
CrSSe	0.55	0.57	0.60	0.68	0.70	0.71	0.60	0.60	0.61	0.63	0.63	0.64
CrSTe	0.30	0.35	0.36	0.37	0.38	0.40	0.55	0.54	0.56	0.58	0.60	0.61
CrSeTe	0.80	0.82	0.84	0.85	0.89	0.91	0.51	0.53	0.55	0.55	0.54	0.55
MoSSe	0.38	0.37	0.42	0.45	0.49	0.55	0.27	0.25	0.26	0.28	0.31	0.32
MoSTe	0.50	0.52	0.52	0.55	0.58	0.63	0.23	0.28	0.33	0.37	0.38	0.41
MoSeTe	0.30	0.32	0.38	0.36	0.37	0.38	0.28	0.27	0.30	0.30	0.31	0.31
WSSe	0.18	0.17	0.20	0.21	0.22	0.23	0.14	0.19	0.19	0.22	0.26	0.24
WSTe	0.61	0.62	0.65	0.66	0.70	0.75	0.42	0.43	0.45	0.46	0.48	0.58
WSeTe	0.24	0.21	0.22	0.23	0.24	0.25	0.22	0.21	0.23	0.23	0.22	0.25
ZrSSe	0.31	0.32	0.31	0.33	0.34	0.35	0.30	0.30	0.31	0.32	0.33	0.32
HfSSe	0.50	0.52	0.55	0.58	0.61	0.62	0.33	0.35	0.38	0.39	0.42	0.44

Table 3.12: Variation of the effective mass of holes with shear strain (γ) for the eleven semiconducting Janus TMD nanotubes.

MXY	Effective mass of holes (a.u.)											
	Armchair						Zigzag					
	$\gamma = 0$	$\gamma = 0.05$	$\gamma = 0.08$	$\gamma = 0.10$	$\gamma = 0.12$	$\gamma = 0.15$	$\gamma = 0$	$\gamma = 0.05$	$\gamma = 0.08$	$\gamma = 0.10$	$\gamma = 0.12$	$\gamma = 0.15$
CrSSe	0.89	0.87	0.81	0.78	0.75	0.63	0.87	0.84	0.82	0.75	0.71	0.67
CrSTe	2.86	2.50	2.29	2.22	2.15	0.87	1.90	1.45	1.44	1.40	1.38	1.37
CrSeTe	1.72	1.70	1.63	1.57	1.21	0.89	0.94	0.90	0.85	0.81	0.78	0.75
MoSSe	0.58	0.57	0.56	0.55	0.50	0.50	0.57	0.55	0.56	0.52	0.51	0.50
MoSTe	2.31	1.95	1.72	1.62	0.61	0.57	1.03	1.00	0.58	0.47	0.35	0.36
MoSeTe	0.62	0.60	0.58	0.55	0.56	0.54	0.68	0.67	0.57	0.35	0.37	0.34
WSSe	0.38	0.37	0.37	0.36	0.35	0.32	0.40	0.39	0.39	0.37	0.36	0.34
WSTe	3.48	1.72	1.48	1.37	1.27	0.68	1.09	1.05	1.01	0.33	0.30	0.38
WSeTe	0.44	0.41	0.41	0.40	0.36	0.47	0.42	0.41	0.34	0.33	0.32	0.35
ZrSSe	0.51	0.49	0.41	0.32	0.33	0.38	0.21	0.19	0.21	0.22	0.23	0.28
HfSSe	0.62	0.60	0.63	0.62	0.60	0.59	0.73	0.41	0.34	0.33	0.32	0.34

Observing a linear and quadratic variation of the semiconducting Janus TMD nanotubes' bandgap with axial and shear strains, respectively, we present results of the corresponding fits in Figure 3.12. It is clear that the fits are excellent, with the exception being

ZrSSe, where there is a non-monotonic variation of the bandgap, as discussed above. The linear dependence of the bandgap on axial strain, which has also been observed for the following TMD nanotubes: MoS₂, MoSe₂, WS₂, WSe₂, and CrS₂ [41, 43, 45, 44], is consistent with previous results for MoSSe [117, 105]. In particular, the slope computed here is -8.7 , which is in good agreement with the slope -7.1 predicted by Ref. [105]. Note that the exact values cannot be compared, since Refs. [117, 105] choose different diameters than the equilibrium values used here. To develop a simple model for the bandgap variation, we also perform linear regression with the features being metal-chalcogen bond lengths, chalcogens' electronegativity difference, axial strain, shear strain, and square of the shear strain, the results of which are presented in Figure 3.12. It is clear that, again with the exception of HfSSe and ZrSSe, there is very good agreement between the computed values and those predicted by the regression model, suggesting the importance of the metal-chalcogen bond lengths and the chalcogens' electronegativity difference in determining the bandgap at any given deformation.

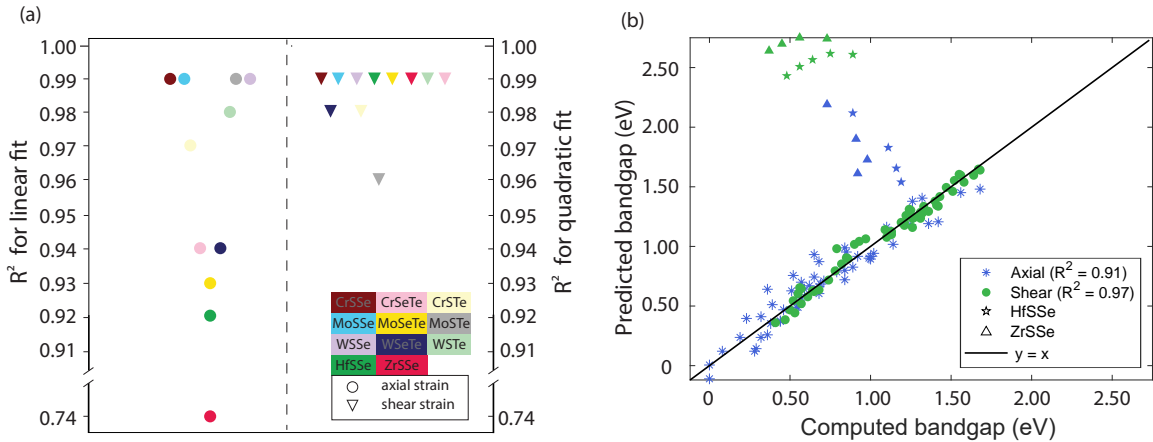


Figure 3.12: (a) The coefficient of determination of the linear regression (R^2) for the linear and quadratic fits of the bandgap vs. axial and shear strain, respectively. (b) The computed bandgap vs. that predicted using the linear regression model. The two outliers: HfSSe and ZrSSe, are not included in the regression. The systems under consideration are the eleven semiconducting armchair Janus TMD nanotubes, with results for the zigzag variants being nearly identical to those presented here.

Next, considering the eleven Janus TMD nanotubes (both armchair and zigzag con-

(figure 3.13) that have determined to be semiconducting, we summarize the variation of the difference between effective mass of holes and electrons with deformations in Figure 3.13. Note that this difference in the effective masses can be used to classify whether the material is a n-type or p-type semiconductor, i.e., if the effective mass of hole is greater than of the electron, then holes have lower mobility, resulting in n-type semiconductor behavior, and vice versa [204]. Here, all the nanotubes are n-type semiconductors in the undeformed configuration, the exception again being ZrSSe. The application of deformation is accompanied by the continuous decrease and increase in the effective mass of holes and electrons, respectively, culminating in an n-type to p-type semiconductor transition for armchair CrSSe, CrSeTe, MoSSe, MoSeTe, MoSTe, WSTe, ZrSSe, and HfSSe, and zigzag CrSSe, CrSeTe, MoSSe, MoSTe, WSTe, and HfSSe nanotubes with axial deformation; and armchair CrSSe, CrSeTe, MoSSe, MoSTe, WSTe, ZrSSe, and HfSSe, and zigzag MoSTe, WSTe, and HfSSe nanotubes with torsional deformation, for the range of strains considered. Indeed, similar to the case of bandgaps, larger strains are expected to introduce transitions for the remaining nanotubes as well, however stability considerations are likely to become important. Such transitions have applications as semiconductor switches [189, 190, 191, 192, 193, 194]. Note that on the application of compressive axial strains, the effective mass of both electrons and holes increases in MoSTe, WSeTe, CrSeTe, CrSTe, and HfSSe, while it decreases in MoSeTe, WSTe, and ZrSSe; and the effective mass of holes and electrons increases and decreases, respectively, for MoSSe, WSSe, and CrSSe.

To gain further physical understanding into the results presented above, considering the semiconducting Janus TMD nanotubes that undergo n-type to p-type transitions, we choose eight representative ones, i.e., four each for transitions resulting from axial and torsional deformations, and plot their electron density difference contours between the strained (smallest value at which transition has occurred) and unstrained nanotube configurations in Figure 3.14. In addition, we utilize Bader analysis [197, 198] to determine the amount of metal-chalcogen charge transfer that has occurred between the undeformed

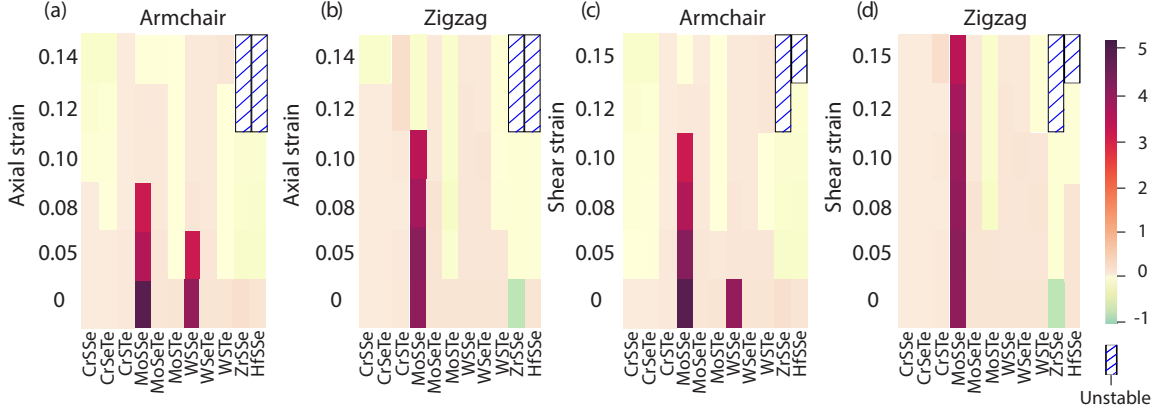


Figure 3.13: Variation of the effective mass of holes minus that of the electrons with axial and torsional deformations for the eleven semiconducting Janus TMD nanotubes.

and deformed nanotube configurations, results of which are also presented in Figure 3.14. We find that there is a minimal change in the Bader charge of atoms upon deformation, suggesting that the nature of the bonding between the atoms remains unaltered. However, there is a significant change in the electron density contours, leading to the conclusion that the observed behavior is a consequence of the rehybridization of orbitals.

3.2.3 Spintronic properties: Rashba and Zeeman effect

We now present the spin-splitting results for Janus TMD nanotubes with axial and shear strain. From Figure 3.15, we show the Zeeman spin-splitting in the Mo and W Janus TMD nanotubes. We consider the splittings at both VBM (Valence Band Maximum) and CBM (Conduction Band Minimum) with axial and shear strain. We observe that the application of mechanical deformation usually results in a decrease in the splitting at VBM (Valence Band Maximum) and CBM (Conduction Band Minimum). The effect of SOC almost dissipates with axial strain at VBM, with splitting reaching 0. The values of VBM and CBM splitting at no mechanical deformation are almost similar to its 2d analogs [199], owing to the large enough diameter considered for the nanotubes. The trend of decrease in splitting is similar to the study on Janus TMD bilayers subjected to biaxial strains [200]. The values for Janus TMDs are also in between their parent TMDs discussed in the last section.

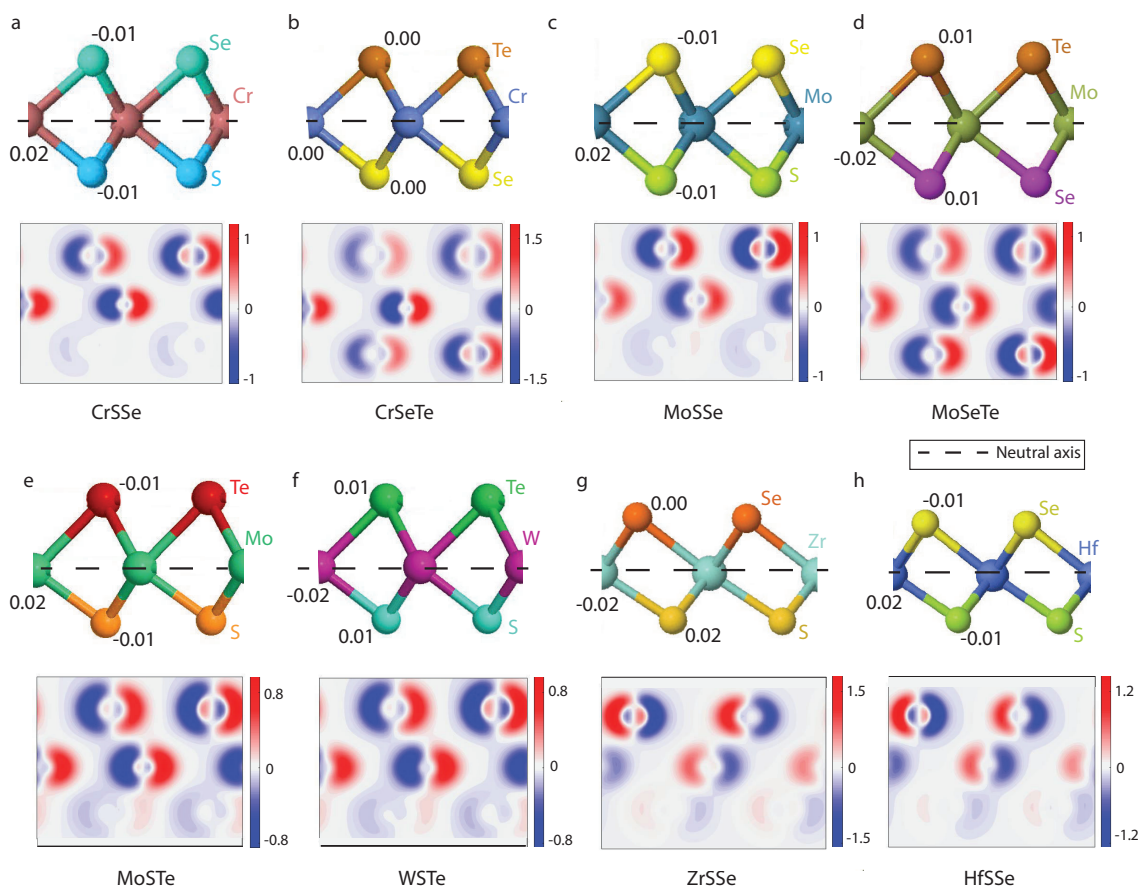


Figure 3.14: Contours of difference in electron density (integrated along the x_1 direction) between the strained — smallest value at which n-type to p-type semiconductor transition occurs — and unstrained armchair nanotube configurations. The top four panels (a, b, c, and d) correspond to axial deformations, and the bottom four panels (e, f, g, and h) correspond to torsional deformations. Contour plots are on x_2x_3 -plane w.r.t their monolayer flat sheet configuration. The numbers listed next to the atoms correspond to the amount of charge transfer, as determined by Bader analysis [197, 198].

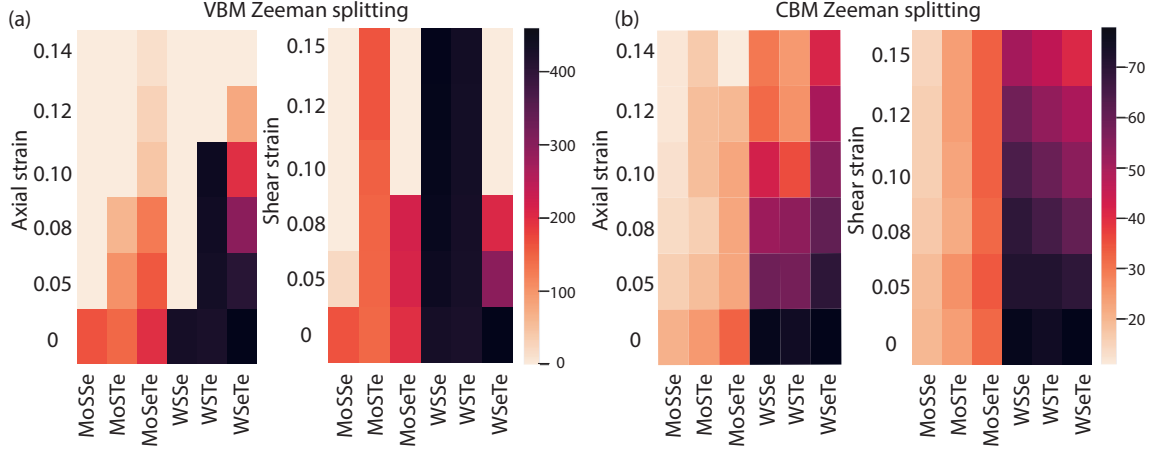


Figure 3.15: Zeeman spin splitting at (a) VBM (Valence Band Maximum) with axial and shear strain and (b) at CBM (Conduction Band Minimum) with axial and shear strain

In Figure 3.16, the Rashba effect is not observed without any shear strain. It is consistent with our theory of the Rashba effect being present in only non-inversion-symmetry materials. As soon as we introduce shear strain (twist) in the nanotube, we break the inversion symmetry and we can see the Rashba coefficient continuously increasing with the strain. The coefficient values at the highest strain are similar to their Janus monolayer analogs which are significant and can be used for spintronics applications. Note that we compute this change along momentum direction at the gamma point, similar to other Rashba effect studies [199, 200].

3.3 Janus Transition metal dihalide (TMH) nanotubes

3.3.1 Electromechanical properties

We now present and discuss the Janus TMH nanotubes' electronic response to axial and torsional deformations, the simulations having been performed using the symmetry-adapted ab initio framework based on Kohn-Sham DFT that has been described in the previous section. The results are compared with those available in literature.

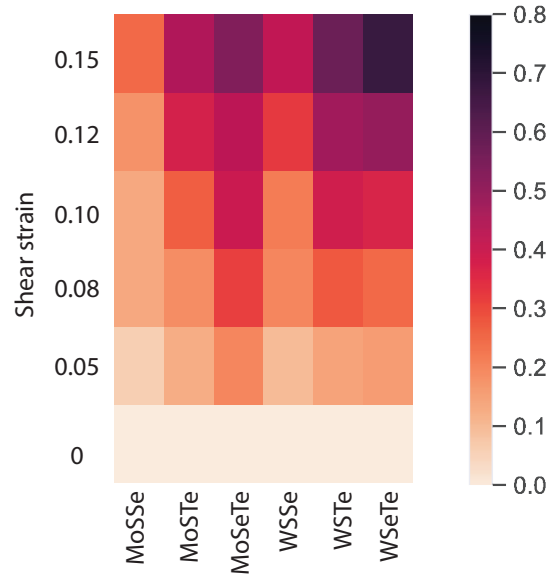


Figure 3.16: Rashba spin splitting coefficient at VBM (Valence Band Maximum) with shear strain (Gamma Point)

Table 3.13: Variation of bandgap with axial strain (ε) for the twelve Janus TMH nanotubes. (D: direct bandgap, I: indirect bandgap). Red colored data points are used for strains at which the nanotube is expected to be unstable, based on phonon calculations for the mono-layer counterparts.

MXY	Bandgap (eV)											
	Armchair						Zigzag					
	$\varepsilon = 0$	$\varepsilon = 0.05$	$\varepsilon = 0.08$	$\varepsilon = 0.10$	$\varepsilon = 0.12$	$\varepsilon = 0.14$	$\varepsilon = 0$	$\varepsilon = 0.05$	$\varepsilon = 0.08$	$\varepsilon = 0.10$	$\varepsilon = 0.12$	$\varepsilon = 0.14$
TiClI	0.80 (I)	0.77 (I)	0.66 (I)	0.59 (D)	0.50 (D)	0.41 (D)	0.77 (I)	0.71 (I)	0.66 (I)	0.62 (I)	0.58 (I)	0.55 (I)
TiBrI	0.75 (I)	0.72 (D)	0.67 (I)	0.61 (I)	0.53 (I)	0.45 (I)	0.74 (I)	0.70 (I)	0.63 (I)	0.59 (I)	0.54 (I)	0.49 (I)
TiClBr	0.86 (I)	0.79 (I)	0.68 (I)	0.59 (D)	0.49 (D)	0.41 (D)	0.86 (I)	0.79 (I)	0.70 (I)	0.65 (I)	0.62 (I)	0.60 (I)
ZrClI	0.92 (I)	0.88 (I)	0.78 (I)	0.69 (I)	0.61 (I)	0.52 (D)	0.90 (I)	0.89 (I)	0.80 (I)	0.74 (I)	0.69 (I)	0.65 (I)
ZrBrI	0.83 (I)	0.83 (I)	0.77 (I)	0.70 (I)	0.64 (I)	0.57 (I)	0.83 (I)	0.84 (I)	0.77 (I)	0.70 (I)	0.65 (I)	0.62 (I)
ZrClBr	0.94 (I)	0.85 (I)	0.72 (I)	0.63 (I)	0.56 (I)	0.50 (D)	0.94 (I)	0.86 (I)	0.74 (I)	0.68 (I)	0.64 (I)	0.62 (I)
HfClI	0.94 (I)	0.93 (I)	0.87 (I)	0.81 (I)	0.73 (I)	0.64 (D)	0.90 (I)	0.91 (I)	0.86 (I)	0.78 (I)	0.71 (I)	0.63 (I)
HfBrI	0.84 (I)	0.82 (I)	0.77 (I)	0.71 (I)	0.65 (I)	0.57 (I)	0.84 (I)	0.85 (I)	0.77 (I)	0.66 (I)	0.55 (I)	0.44 (I)
HfClBr	0.93 (I)	0.90 (I)	0.79 (I)	0.70 (I)	0.61 (I)	0.53 (I)	0.93 (I)	0.91 (I)	0.79 (I)	0.69 (I)	0.63 (I)	0.55 (I)
FeClI	0.55 (I)	0.55 (I)	0.51 (I)	0.44 (I)	0.38 (I)	0.31 (I)	0.55 (I)	0.51 (I)	0.43 (I)	0.41 (I)	0.38 (I)	0.36 (I)
FeBrI	0.62 (I)	0.56 (I)	0.50 (I)	0.45 (I)	0.38 (I)	0.31 (I)	0.62 (I)	0.52 (I)	0.44 (I)	0.38 (I)	0.34 (I)	0.30 (I)
FeClBr	0.67 (I)	0.57 (I)	0.49 (I)	0.42 (I)	0.35 (I)	0.29 (I)	0.66 (I)	0.52 (I)	0.44 (I)	0.39 (I)	0.33 (I)	0.27 (I)

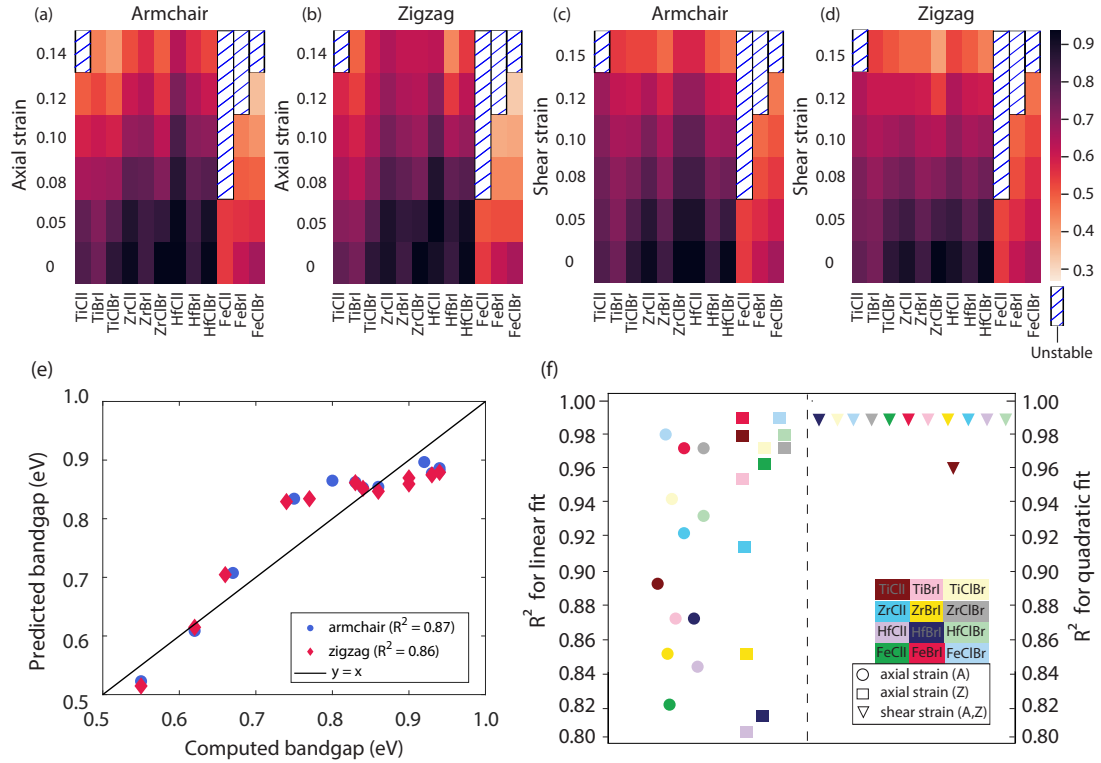


Figure 3.17: (a), (b): variation of bandgap with axial strains; and (c), (d): variation of bandgap with shear strains for the twelve armchair and zigzag Janus TMH nanotubes. (e): computed bandgap for the undeformed nanotubes vs. that predicted by the linear regression model. (f): coefficient of determination of the linear regression (R^2) for the linear and quadratic fits of the bandgap vs. axial and shear strains, respectively.

Table 3.14: Variation of the effective mass of electrons with axial strain (ϵ) for the twelve semiconducting Janus TMH nanotubes. Red colored data points are used for strains at which the nanotube is expected to be unstable, based on phonon calculations for the monolayer counterparts.

MXY	Effective mass of electrons (a.u.)											
	Armchair						Zigzag					
	$\epsilon = 0$	$\epsilon = 0.05$	$\epsilon = 0.08$	$\epsilon = 0.10$	$\epsilon = 0.12$	$\epsilon = 0.14$	$\epsilon = 0$	$\epsilon = 0.05$	$\epsilon = 0.08$	$\epsilon = 0.10$	$\epsilon = 0.12$	$\epsilon = 0.14$
TiClI	1.66	1.71	1.86	1.87	1.92	1.86	1.62	1.70	1.87	1.88	1.93	1.86
TiBrI	1.76	1.22	1.37	1.52	1.55	1.59	1.74	1.21	1.31	1.50	1.52	1.57
TiClBr	1.23	1.31	1.45	1.51	1.55	1.61	1.23	1.32	1.47	1.53	1.58	1.62
ZrClI	0.82	2.27	2.55	3.26	3.55	3.55	0.84	2.29	2.54	3.21	3.35	3.45
ZrBrI	0.95	2.11	3.11	3.41	3.56	3.78	0.95	2.02	2.91	3.12	3.44	3.68
ZrClBr	0.53	0.66	0.77	0.86	0.97	0.85	0.50	0.61	0.71	0.89	0.98	0.93
HfClI	0.62	1.31	1.89	4.55	4.54	4.54	0.62	1.35	1.96	4.23	4.27	4.35
HfBrI	1.01	1.40	1.56	1.63	2.11	2.20	1.01	1.60	1.66	1.78	2.16	2.43
HfClBr	0.70	1.76	2.41	2.54	2.74	2.85	0.70	1.42	2.21	2.66	2.73	2.87
FeClI	2.11	2.32	2.35	2.41	2.45	2.45	2.05	2.17	2.18	2.19	2.25	2.33
FeBrI	0.70	0.72	0.75	1.62	1.72	1.88	0.70	0.79	0.86	1.51	1.87	1.97
FeClBr	0.74	0.75	1.65	1.66	1.77	1.87	0.74	0.78	1.67	1.68	1.86	1.99

Table 3.15: Variation of the effective mass of holes with axial strain (ε) for the twelve semi-conducting Janus TMH nanotubes. Red colored data points are used for strains at which the nanotube is expected to be unstable, based on phonon calculations for the monolayer counterparts.

MXY	Effective mass of holes (a.u.)											
	Armchair						Zigzag					
	$\varepsilon = 0$	$\varepsilon = 0.05$	$\varepsilon = 0.08$	$\varepsilon = 0.10$	$\varepsilon = 0.12$	$\varepsilon = 0.14$	$\varepsilon = 0$	$\varepsilon = 0.05$	$\varepsilon = 0.08$	$\varepsilon = 0.10$	$\varepsilon = 0.12$	$\varepsilon = 0.14$
TiClI	0.58	0.58	0.57	0.55	0.54	0.55	0.59	0.55	0.54	0.53	0.52	0.54
TiBrI	0.53	0.53	0.54	0.53	0.51	0.49	0.52	0.53	0.52	0.53	0.51	0.51
TiClBr	0.56	0.55	0.57	0.54	0.53	0.52	0.56	0.56	0.55	0.54	0.54	0.55
ZrClI	0.41	0.40	0.35	0.34	0.33	0.32	0.40	0.40	0.39	0.38	0.39	0.36
ZrBrI	0.83	0.82	0.83	0.81	0.81	0.80	0.84	0.85	0.84	0.84	0.85	0.83
ZrClBr	0.38	0.34	0.33	0.31	0.30	0.30	0.35	0.31	0.32	0.30	0.31	0.31
HfClI	0.33	0.32	0.31	0.31	0.27	0.28	0.34	0.35	0.34	0.33	0.31	0.30
HfBrI	0.31	0.32	0.30	0.28	0.25	0.26	0.36	0.32	0.29	0.28	0.28	0.27
HfClBr	0.33	0.33	0.30	0.34	0.35	0.33	0.30	0.32	0.27	0.28	0.28	0.27
FeClI	1.57	1.55	1.49	1.46	1.45	1.47	1.55	1.57	1.51	1.49	1.45	1.33
FeBrI	0.50	0.52	0.54	0.52	0.52	0.52	0.54	0.53	0.53	0.51	0.47	0.47
FeClBr	0.54	0.54	0.55	0.54	0.53	0.53	0.54	0.48	0.49	0.47	0.48	0.49

Table 3.16: Variation of bandgap with shear strain (γ) for the twelve select Janus TMH nanotubes. (D: direct bandgap, I: indirect bandgap). Red colored data points are used for strains at which the nanotube is expected to be unstable, based on phonon calculations for the monolayer counterparts.

MXY	Bandgap (eV)											
	Armchair						Zigzag					
	$\gamma = 0$	$\gamma = 0.05$	$\gamma = 0.08$	$\gamma = 0.10$	$\gamma = 0.12$	$\gamma = 0.15$	$\gamma = 0$	$\gamma = 0.05$	$\gamma = 0.08$	$\gamma = 0.10$	$\gamma = 0.12$	$\gamma = 0.15$
TiClI	0.80 (I)	0.77 (I)	0.75 (I)	0.72 (I)	0.68 (I)	0.61 (I)	0.77 (I)	0.74 (I)	0.73 (I)	0.68 (I)	0.65 (I)	0.56 (I)
TiBrI	0.75 (I)	0.72 (I)	0.70 (I)	0.66 (I)	0.62 (I)	0.55 (I)	0.74 (I)	0.73 (I)	0.69 (I)	0.65 (I)	0.61 (I)	0.54 (I)
TiClBr	0.86 (I)	0.80 (I)	0.73 (I)	0.67 (I)	0.61 (I)	0.53 (I)	0.86 (I)	0.80 (I)	0.73 (I)	0.67 (I)	0.61 (I)	0.51 (I)
ZrClI	0.92 (I)	0.87 (I)	0.79 (I)	0.73 (I)	0.65 (I)	0.53 (I)	0.90 (I)	0.83 (I)	0.75 (I)	0.69 (I)	0.61 (I)	0.48 (I)
ZrBrI	0.83 (I)	0.78 (I)	0.71 (I)	0.66 (I)	0.59 (I)	0.48 (I)	0.83 (I)	0.77 (I)	0.70 (I)	0.65 (I)	0.60 (I)	0.48 (I)
ZrClBr	0.94 (I)	0.89 (I)	0.82 (I)	0.77 (I)	0.69 (I)	0.58 (I)	0.94 (I)	0.82 (I)	0.72 (I)	0.64 (I)	0.54 (I)	0.40 (I)
HfClI	0.94 (I)	0.89 (I)	0.82 (I)	0.77 (I)	0.69 (I)	0.58 (I)	0.90 (I)	0.84 (I)	0.76 (I)	0.70 (I)	0.65 (I)	0.53 (I)
HfBrI	0.84 (I)	0.78 (I)	0.73 (I)	0.67 (I)	0.61 (I)	0.50 (I)	0.84 (I)	0.78 (I)	0.72 (I)	0.66 (I)	0.61 (I)	0.50 (I)
HfClBr	0.93 (I)	0.84 (I)	0.75 (I)	0.68 (I)	0.60 (I)	0.47 (I)	0.93 (I)	0.84 (I)	0.75 (I)	0.68 (I)	0.60 (I)	0.45 (I)
FeClI	0.55 (I)	0.54 (I)	0.51 (I)	0.48 (I)	0.44 (I)	0.38 (I)	0.55 (I)	0.53 (I)	0.49 (I)	0.47 (I)	0.43 (I)	0.38 (I)
FeBrI	0.62 (I)	0.57 (I)	0.52 (I)	0.48 (I)	0.44 (I)	0.36 (I)	0.62 (I)	0.57 (I)	0.52 (I)	0.49 (I)	0.45 (I)	0.39 (I)
FeClBr	0.67 (I)	0.60 (I)	0.55 (I)	0.51 (I)	0.46 (I)	0.36 (I)	0.66 (I)	0.61 (I)	0.57 (I)	0.53 (I)	0.47 (I)	0.39 (I)

Table 3.17: Variation of the effective mass of electrons with shear strain (γ) for the twelve semiconducting Janus TMH nanotubes. Red colored data points are used for strains at which the nanotube is expected to be unstable, based on phonon calculations for the mono-layer counterparts.

MXY	Effective mass of electrons (a.u.)											
	Armchair						Zigzag					
	$\gamma = 0$	$\gamma = 0.05$	$\gamma = 0.08$	$\gamma = 0.10$	$\gamma = 0.12$	$\gamma = 0.15$	$\gamma = 0$	$\gamma = 0.05$	$\gamma = 0.08$	$\gamma = 0.10$	$\gamma = 0.12$	$\gamma = 0.15$
TiClI	1.66	1.73	1.88	1.86	1.90	1.96	1.62	1.71	1.97	1.96	1.99	1.98
TiBrI	1.76	1.52	1.86	1.87	1.88	1.96	1.74	1.59	1.67	1.78	1.79	1.87
TiClBr	1.23	1.37	1.43	1.57	1.59	1.71	1.23	1.34	1.42	1.58	1.65	1.63
ZrClI	0.82	2.08	2.45	3.58	3.85	3.95	0.84	2.09	2.26	3.12	3.55	3.54
ZrBrI	0.95	1.82	3.24	3.21	3.44	3.46	0.95	2.47	2.45	3.04	3.17	3.28
ZrClBr	0.53	0.61	0.70	0.89	0.98	0.92	0.50	0.62	0.69	0.81	0.88	0.94
HfClI	0.62	1.22	1.56	3.15	4.01	4.61	0.62	1.06	1.91	4.74	4.75	4.75
HfBrI	1.01	1.39	1.65	1.62	1.64	1.65	1.01	1.40	1.46	1.49	1.56	1.53
HfClBr	0.70	1.26	2.01	2.14	2.14	2.16	0.70	1.23	2.02	2.44	2.53	2.77
FeClI	2.11	2.05	2.06	2.11	2.15	2.29	2.05	2.14	2.19	2.21	2.22	2.03
FeBrI	0.70	0.71	0.74	1.22	1.52	1.66	0.70	0.83	0.85	1.53	1.97	1.99
FeClBr	0.74	0.76	1.25	1.26	1.37	1.44	0.74	0.82	0.99	1.18	1.16	1.49

Table 3.18: Variation of the effective mass of holes with shear strain (γ) for the twelve semiconducting Janus TMH nanotubes. Red colored data points are used for strains at which the nanotube is expected to be unstable, based on phonon calculations for the mono-layer counterparts.

MXY	Effective mass of holes (a.u.)											
	Armchair						Zigzag					
	$\gamma = 0$	$\gamma = 0.05$	$\gamma = 0.08$	$\gamma = 0.10$	$\gamma = 0.12$	$\gamma = 0.15$	$\gamma = 0$	$\gamma = 0.05$	$\gamma = 0.08$	$\gamma = 0.10$	$\gamma = 0.12$	$\gamma = 0.15$
TiClI	0.58	0.57	0.56	0.55	0.55	0.55	0.59	0.59	0.57	0.56	0.51	0.52
TiBrI	0.53	0.55	0.52	0.51	0.50	0.50	0.52	0.54	0.51	0.50	0.50	0.48
TiClBr	0.56	0.54	0.55	0.53	0.51	0.51	0.56	0.57	0.56	0.53	0.52	0.51
ZrClI	0.41	0.38	0.39	0.38	0.37	0.36	0.40	0.38	0.37	0.36	0.37	0.37
ZrBrI	0.83	0.81	0.82	0.80	0.81	0.81	0.84	0.84	0.83	0.82	0.82	0.81
ZrClBr	0.38	0.36	0.34	0.33	0.33	0.32	0.35	0.33	0.30	0.31	0.30	0.28
HfClI	0.33	0.31	0.29	0.30	0.29	0.29	0.34	0.36	0.33	0.32	0.30	0.30
HfBrI	0.31	0.31	0.31	0.29	0.28	0.28	0.36	0.34	0.27	0.28	0.27	0.25
HfClBr	0.33	0.32	0.32	0.33	0.34	0.34	0.30	0.31	0.28	0.29	0.29	0.29
FeClI	1.57	1.57	1.59	1.56	1.54	1.55	1.55	1.51	1.50	1.51	1.49	1.42
FeBrI	0.50	0.51	0.52	0.51	0.51	0.51	0.54	0.52	0.51	0.50	0.48	0.48
FeClBr	0.54	0.53	0.54	0.55	0.54	0.52	0.54	0.49	0.51	0.52	0.49	0.50

In Figure 3.17(a)–(d), we present the variation in bandgap with applied axial and shear strains for the Janus TMH nanotubes. We observe that in the undeformed (i.e., equilibrium) configuration, all the nanotubes are semiconducting, with bandgaps ranging from 0.55 (FeClI) to 0.94 eV (ZrClBr and HfClI). For predicting the bandgap variation between the different materials, we develop a regression model using the bond lengths and electronegativity difference between the halogens as features. We find that this simple model is able to capture the bandgaps of the undeformed nanotubes reasonably accurately (Figure 3.17(e)). Upon the application of axial/torsional deformations, the value of the bandgap reduces monotonically. In particular, the bandgap decreases linearly and quadratically with axial and shear strains, respectively, the average coefficient of determination of linear regression for the linear and quadratic fits being 0.92 and 0.99, respectively (Figure 3.17(f)). Similar trends have recently been predicted for the response of transition metal dichalcogenide (TMD) nanotubes [49] and their Janus counterparts [152]. In the case of TMD nanotubes, the linear decrease of bandgap with axial strains has also been predicted in Refs. [41, 43, 44, 45]. Considering three armchair representative cases (HfBrI, TiClBr and ZrBrI) at the same radius, we also find that the bandgap of unstrained and shear strained MXY TMH Janus nanotubes lie between (some cases on the extremities ± 0.02 eV) their MX₂ and MY₂ counterparts — similar to TMDs [49, 152]. Similar to MXY nanotubes, the bandgap for MX₂ and MY₂ follows quadratic decrease with shear strain. Axially strained MX₂ and MY₂ nanotubes for HfBrI and ZrBrI cases experience an increase in bandgap at smaller strains and then monotonically decreases at higher strains, different to MXY nanotubes (observed also in HfSSe and ZrSSe nanotubes [152]). Although, for the case of TiClBr, the bandgap undergoes a linear decrease for TiCl₂ and TiBr₂ — similar to MXY nanotubes — with the bandgap of TiClBr in between them. The results indicate that semiconductor to metal transitions are likely to occur when larger strains are considered, however the stability of the nanotubes under such conditions warrants a more careful analysis. The ability to strain engineer the bandgap in Janus TMH nanotubes has potential applications in devices,

e.g., mechanical sensors [75, 76, 42].

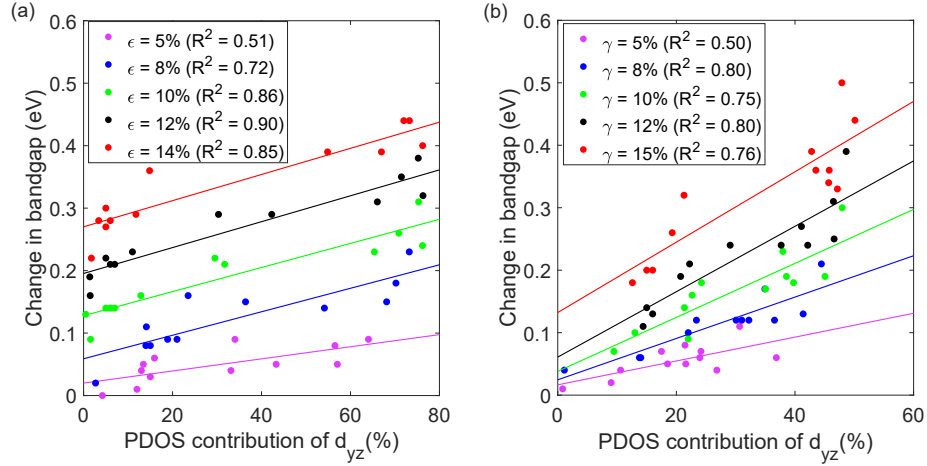


Figure 3.18: The change in bandgap for the twelve armchair Janus TMH nanotubes vs. the percentage contribution of the transition metal's d_{yz} orbital to the PDOS at the bottom of the conduction band.

To correlate the bandgap variation with changes in the electronic structure, we compute the atomic orbital projected density of states (PDOS) for the Janus TMH nanotubes at all the configurations studied in this work, i.e., equilibrium and axially/torsionally deformed. For armchair nanotubes, we find that the transition metal's in-plane d orbital, i.e., d_{yz} orbital, is dominant near the edges of the bandgap — exception being when the transition metal is iron, for which the d_{xz} orbital is dominant — making it the focus of study here. In addition, the changes that occur with deformation are more significant at the upper edge of the bandgap, i.e., bottom of the conduction band, therefore the analysis here is restricted to that region. In Figure 3.18, for each of the five axial and shear strains considered, we plot the change in bandgap vs. the contribution of the transition metal's d_{yz} orbital to the PDOS at the bottom of the conduction band. We observe that for a given strain, the change in bandgap is well correlated with the transition metal's d_{yz} 's contribution to the PDOS, with the average coefficient of determination of the linear regression for axial and shear strains being 0.77 and 0.72, respectively. The importance of d_{yz} in determining the response is to be expected, given its in-plane nature, which means that it is the most likely to undergo significant changes upon the application of axial and torsional deformations. We also observe

that the total contribution of different orbitals remains same with the application of strains and the only change is within those orbitals (e.g. p_x , p_y , p_z). This leads to the fact that the hybridization of orbitals in the Janus TMH nanotubes are not changing with the application of strains.

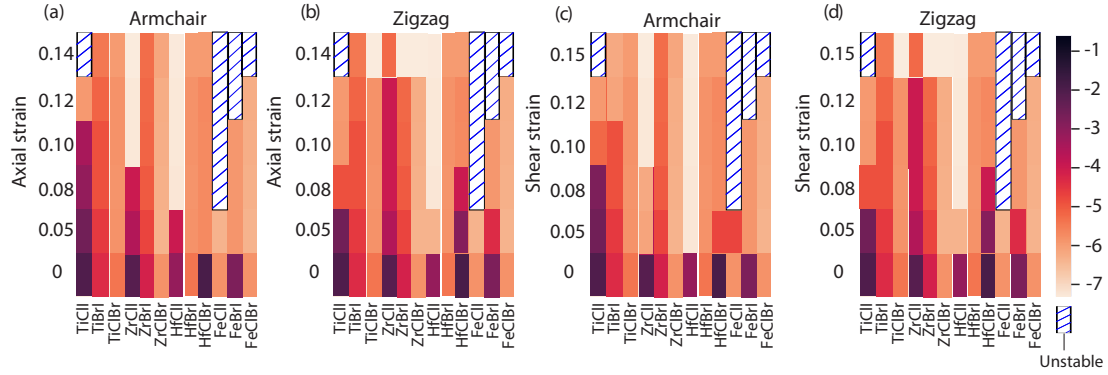


Figure 3.19: Variation of the difference in charge carriers' effective mass (holes minus electrons) with axial and shear strains for the twelve armchair and zigzag Janus TMH nanotubes.

In Figure 3.19, we present the variation in the difference between the effective mass of holes and electrons (holes minus electrons) with axial and shear strains for the Janus TMH nanotubes. Based on whether this quantity is positive or negative, the material can be classified as a n-type or p-type semiconductor, respectively. In particular, if the effective mass of electron is greater than of the hole, then the mobility of electrons is lower, translating to a lower conduction of electrons, making it a p-type semiconductor, and vice versa [204]. We observe from the figure that all the Janus TMH nanotubes are p-type semiconductors in their undeformed state, differing from TMD and Janus TMD nanotubes, which are generally n-type semiconductors [49, 152]. On the application of axial and torsional deformations, there is a continuous increase and decrease in the effective mass of electrons and holes, respectively, similar to that observed for TMD and Janus TMD nanotubes [49, 152]. This hole mobility enhancement [205, 206] makes the Janus TMH nanotubes more dominant p-type semiconductors, which has applications in devices such as MOSFET transistors [207, 208]. Considering the above three armchair representative cases (HfBrI,

TiClBr and ZrBrI) at the same radius, we also find that the effective mass of charge carriers of unstrained and shear strained MXY TMH Janus nanotubes lie between their MX₂ and MY₂ counterparts — similar to TMDs [49, 152]. However it is only true for axially strained MX₂ and MY₂ nanotubes of TiClBr case with HfBrI and ZrBrI cases as exceptions similar to the bandgap.

CHAPTER 4

CONCLUSION

4.1 Transition metal dichalcogenide (TMD) nanotubes

4.1.1 Elastic properties

We have calculated the torsional moduli of forty-five select single-walled TMD nanotubes using *ab initio* DFT simulations. Specifically, we have computed torsional moduli for the armchair and zigzag variants of the chosen TMD nanotubes at practically relevant twists and nanotube diameters, while considering materials that have been synthesized or are likely to be synthesized. We have found that the variation of the torsional moduli values between the different nanotubes follows the trend: $MS_2 > MSe_2 > MTe_2$. In addition, we have found that the moduli display a power law dependence on the diameter, with the scaling generally close to cubic, as predicted by the isotropic elastic continuum model. In particular, the shear moduli so determined have been found to be in good agreement with that predicted by the isotropic relation in terms of the Young's modulus and Poisson's ratio, both of which have also been calculated in this work from DFT simulations. Finally, we have developed a linear regression model for the torsional moduli of TMD nanotubes that is based on the nature and characteristics of the metal-chalcogen bond, and have shown that it is capable of making reasonably accurate predictions.

4.1.2 Electromechanical response

We have studied the electronic response of single-walled TMD nanotubes to torsional deformations. In particular, using symmetry-adapted first principles DFT simulations, we have determined the variation in bandgap and effective mass of charge carriers with twist for forty-five select armchair and zigzag TMD nanotubes. We have found that whereas the

nature of originally metallic nanotubes remains unaltered, there is a continuous decrease in bandgap — changes to indirect for systems that are originally direct — with increasing twist for semiconducting TMD nanotubes, culminating in semiconductor to metal transitions. In addition, we have found that the effective mass of holes and electrons continuously decrease and increase with twist, respectively, culminating in transitions from n-type to p-type semiconducting behavior. We have found that these changes can be attributed to rehybridization of orbitals in the metal and chalcogen atoms, rather than charge transfer between them. Overall, we conclude that torsional deformations represent a powerful tool to tailor the electronic properties of semiconducting TMD nanotubes, with applications to devices such as sensors and semiconductor switches.

4.1.3 Spintronic properties: Rashba and Zeeman effect

We investigated the response of single-walled TMD nanotubes to axial and torsional deformations while accounting for spin-orbit coupling. Through symmetry-adapted first-principles DFT simulations, we determined the splitting of eigenvalues at VBM and CBM for Zeeman effect and Rashba effect with twist for twelve synthesized armchair TMD nanotubes. Our results show that the introduction of spin-orbital coupling (SOC) has no effect on metallic nanotubes, such as NbS₂, NbSe₂, TaS₂, TiSe₂, and other TMD nanotubes such as TiS₂, HfS₂, and ZrS₂. However, Mo and W TMD nanotubes exhibit significant SOC effects, with mechanical deformation typically resulting in a decrease in the Zeeman splitting at VBM and CBM. The effect of SOC diminishes with axial strain at VBM, with the splitting reaching 0. Furthermore, we introduced twist in these TMD nanotubes, breaking the inversion symmetry, and observed that the Rashba coefficient continuously increases with strain. At the highest strain, the coefficient values become significant and could have applications in spintronics. Our findings contribute to a better understanding of the role of spin-orbit coupling in TMD nanotubes and have potential implications for the design of novel electronic and spintronic devices.

4.2 Janus TMD nanotubes

4.2.1 Elastic properties

We have calculated the elastic properties of select single-walled Janus TMD nanotubes from first principles DFT. In particular, considering the twenty-seven Janus TMD nanotubes that have previously been predicted to be thermodynamically stable, we have performed symmetry-adapted Kohn-Sham DFT simulations to compute the torsional moduli, Young's moduli, and Poisson's ratios for the armchair and zigzag variants of these materials at their equilibrium diameters. We have found the following trend in the moduli: $MSSe > MSTe > MSeTe$, while their anisotropy with respect to armchair and zigzag configurations has the ordering: $MSTe > MSeTe > MSSe$. We have confirmed this anisotropy and ordering between the different groups by computing the shear modulus from the torsional modulus using an isotropic elastic continuum model, and comparing it with the value predicted from the isotropic relation written in terms of the Young's modulus and Poisson's ratio. We have also developed a reasonably accurate linear regression model for the torsional and Young's moduli of Janus TMD nanotubes based on the metal-chalcogen bonds' nature/characteristics and the difference in electronegativity between the chalcogens.

4.2.2 Electromechanical response

We have investigated the electronic response of Janus TMD nanotubes to mechanical deformations using ab-initio simulations. In particular, considering the full set of eighteen such nanotubes that are identified to be stable, we have performed Kohn-Sham calculations to determine the change in bandgap and charge carriers' effective mass upon axial and torsional deformations, for both the armchair and zigzag variants. We have found that the metallic nanotubes continue to remain metallic even upon deformation, whereas semiconducting nanotubes' bandgap generally decreases with axial and shear strains, in linear and quadratic fashion, respectively, leading to semiconductor–metal transitions. In addi-

tion, we have observed a continual decrease and increase in mass of holes and electrons, respectively, with strains, leading to transitions from n-type to p-type semiconducting behavior. We have used electronic and charge transfer analysis to show that the response is determined by the rehybridization of orbitals, instead of charge transfer between the atoms. Overall, mechanical deformations represent powerful tools for tailoring the electronic response of semiconducting Janus TMD nanotubes, which has a number of applications, including devices such as semiconductor switches and mechanical sensors.

4.2.3 Spintronic properties: Rashba and Zeeman effect

We investigated the response of single-walled Janus TMD nanotubes to axial and torsional deformations while accounting for spin-orbit coupling. Using symmetry-adapted first-principles DFT simulations, we determined the Zeeman and Rashba splittings at VBM and CBM for six armchair Janus TMD nanotubes. Our results indicate that spin-orbit coupling has significant effects, with mechanical deformation typically resulting in a decrease in the Zeeman splitting at VBM and CBM. The effect of SOC diminishes with axial strain at VBM, with the splitting reaching 0. Furthermore, by introducing twist in these Janus TMD nanotubes, we broke the inversion symmetry and observed a continuous increase in the Rashba coefficient with strain. At the highest strain, the coefficient values became significant and could have applications in spintronics. Notably, the coefficient values for Janus TMDs were found to be intermediate to their parent TMDs, as discussed in the previous section. These values were also similar to their Janus monolayer analogs, which have significant potential for spintronics applications. Our findings contribute to a better understanding of the role of spin-orbit coupling in TMD nanotubes and have potential implications for the design of novel electronic and spintronic devices.

4.3 Janus Transition metal dihalide (TMH) nanotubes

4.3.1 Electromechanical properties

We have performed ab initio Kohn-Sham DFT calculations to study the electronic response of Janus TMH nanotubes to mechanical deformations. Specifically, considering twelve armchair and zigzag Janus TMH nanotubes at their equilibrium diameters — predicted to be stable based on the phonon analysis of flat monolayer counterparts — we have determined the variation in bandgap and effective mass of charge carriers with the application of tensile and torsional deformations. We have found that the nanotubes undergo a linear and quadratic decrease in bandgap with tensile and shear strain, respectively. Simultaneously, there is a continual increase and decrease in the effective mass of electrons and holes, respectively. We have found that for a given strain, the change in bandgap for armchair nanotubes can be correlated with the transition metal's in-plane d orbital's contribution to the projected density of states at the bottom of the conduction band. Overall, the current work shows that mechanical deformations represent a powerful tool to control the electronic properties of Janus TMH nanotubes, with applications in devices such as sensors and MOSFET transistors.

CHAPTER 5

FUTURE WORK

The present study provides promising avenues for further research. One such direction is the exploration of the electromechanical response of multi-walled transition metal nanotubes. These nanotubes are important for practical applications due to their ease of synthesis and could offer a deeper understanding of the behavior of transition metal nanotubes under mechanical deformation. In particular, studying the influence of spin-orbit coupling on the electromechanical response of these nanotubes would be of great interest. Additionally, extending such studies to large twists could reveal unexpected nonlinear behavior and provide valuable insights into the mechanical response of these systems.

Another exciting avenue for future research is to investigate the flexoelectric coefficients of transition metal and Janus transition metal nanotubes under mechanical deformation. Flexoelectricity is an electromechanical property that introduces dipole moment in a system on the application of a strain gradient. In addition, the thermal and optical response of these nanotubes to mechanical deformation presents itself as another fascinating subject for future investigation. To further enhance our understanding of Janus transition metal nanotubes, it would be beneficial to determine their mechanical stability from phonon analyses. While we have calculated the phonon spectra for their monolayers and identified stable monolayers and maximum stable strains, using symmetry-adapted density functional perturbation theory [209] to compute the phonon band structure of Janus transition metal nanotubes could verify their mechanical stability in both undeformed and deformed configurations. Using this, we can also study electron-phonon interactions and their optical properties. This would provide crucial insights into the mechanical behavior of these materials and their potential for future applications.

We also plan to implement linear SQ (Spectral Quadrature) [210, 211, 212] and coarse-

graining methods [213] in the Cyclix code to study large systems with defects [214]. CISS (Chiral-induced spin-selectivity) effect [215] can also be studied in these materials with the implementation of non-collinear spin. We can also perform symmetry-adapted ab-initio molecular dynamics [216] simulations with Cyclix-DFT to study the non-equilibrium configurations and dynamic properties such as thermal conductivity. Overall, the results of this study open up several new directions for future research on the transition metal and Janus transition metal nanotubes, which have the potential to lead to significant advancements in the field of nanotechnology.

Appendices

APPENDIX A
NANOTUBE GEOMETRY

Table A1. Equilibrium geometry for the forty-five TMD nanotubes. The atom positions are $\hat{\mathbf{R}} = r\mathbf{a}_1 + r\mathbf{a}_2 + z\mathbf{a}_3$, where $\mathbf{a}_1 = \cos \frac{2\pi\theta}{\eta} \hat{\mathbf{e}}_1$, $\mathbf{a}_2 = \sin \frac{2\pi\theta}{\eta} \hat{\mathbf{e}}_2$, and $\mathbf{a}_3 = H\hat{\mathbf{e}}_3$, with $\hat{\mathbf{e}}_1$, $\hat{\mathbf{e}}_2$, and $\hat{\mathbf{e}}_3$ being the unit vectors along the x_1 , x_2 , and x_3 directions, respectively. For the armchair and zigzag nanotubes, $\eta = \frac{2\pi R}{\sqrt{3}a}$ and $\eta = \frac{2\pi R}{a}$, respectively. The radius of the nanotube is R . $\alpha = \frac{\pi}{\eta H}$

MX ₂	Armchair			Zigzag		
	Unit cell <i>H</i> (Bohr)	<i>R</i> (nm)	Atom positions (<i>r</i> − <i>R</i> (Bohr), θ , <i>z</i>)	Unit cell <i>H</i> (Bohr)	<i>R</i> (nm)	Atom positions (<i>r</i> − <i>R</i> (Bohr), θ , <i>z</i>)
WS ₂	3.01	2.5	W: (0.00, 0.00, 0.00) S: (−2.98, 0.33, 0.00) (2.98, 0.33, 0.00)	5.21	2.5	W: (0.00, 0.00, 0.00) S: (−2.98, 0.00, 0.67) (2.98, 0.00, 0.68)
WSe ₂	3.14	2.5	W: (0.00, 0.00, 0.00) Se: (−3.17, 0.33, 0.00) (3.17, 0.33, 0.00)	5.43	2.5	W: (0.00, 0.00, 0.00) Se: (−3.17, 0.00, 0.67) (3.17, 0.00, 0.68)
WTe ₂	3.34	2.5	W: (0.00, 0.00, 0.00) Te: (−3.46, 0.34, 0.00) (3.46, 0.33, 0.00)	5.78	2.5	W: (0.00, 0.00, 0.00) Te: (−3.46, 0.00, 0.67) (3.46, 0.00, 0.67)
MoS ₂	3.01	2.5	Mo: (0.00, 0.00, 0.00) S: (−2.96, 0.33, 0.00) (2.96, 0.33, 0.00)	5.21	2.5	Mo: (0.00, 0.00, 0.00) S: (−2.96, 0.00, 0.67) (2.96, 0.00, 0.67)
MoSe ₂	3.14	2.5	Mo: (0.00, 0.00, 0.00) Se: (−3.15, 0.34, 0.00) (3.15, 0.33, 0.00)	5.43	2.5	Mo: (0.00, 0.00, 0.00) Se: (−3.15, 0.00, 0.67) (3.15, 0.00, 0.67)
MoTe ₂	3.34	2.5	Mo: (0.00, 0.00, 0.00) Te: (−3.45, 0.34, 0.00) (3.45, 0.33, 0.00)	5.79	2.5	Mo: (0.00, 0.00, 0.00) Te: (−3.45, 0.00, 0.67) (3.45, 0.00, 0.67)
CrS ₂	2.88	4.0	Cr: (0.00, 0.00, 0.00) S: (−2.79, 0.33, 0.00) (2.79, 0.33, 0.00)	4.99	4.0	Cr: (0.00, 0.00, 0.00) S: (−2.79, 0.00, 0.67) (2.79, 0.00, 0.67)
CrSe ₂	3.04	4.0	Cr: (0.00, 0.00, 0.00) Se: (−2.97, 0.33, 0.00) (2.97, 0.33, 0.00)	5.26	4.0	Cr: (0.00, 0.00, 0.00) Se: (−2.97, 0.00, 0.67) (2.97, 0.00, 0.67)

Table A1. - *continued.*

MX ₂	Armchair			Zigzag		
	Unit cell <i>H</i> (Bohr)	<i>R</i> (nm)	Atom positions (<i>r</i> - <i>R</i> (Bohr), θ , <i>z</i>)	Unit cell <i>H</i> (Bohr)	<i>R</i> (nm)	Atom positions (<i>r</i> - <i>R</i> (Bohr), θ , <i>z</i>)
CrTe ₂	3.29	4.0	Cr: (0.00, 0.00, 0.00) Te: (-3.22, 0.34, 0.00) (3.22, 0.33, 0.00)	5.71	3.5	Cr: (0.00, 0.00, 0.00) Te: (-3.22, 0.00, 0.67) (3.22, 0.00, 0.67)
VS ₂	2.99	4.0	V: (0.00, 0.00, 0.00) S: (-2.82, 0.33, 0.00) (2.82, 0.33, 0.00)	5.18	3.5	V: (0.00, 0.00, 0.00) S: (-2.82, 0.00, 0.67) (2.82, 0.00, 0.67)
VSe ₂	3.14	3.5	V: (0.00, 0.00, 0.00) Se: (-3.03, 0.34, 0.00) (3.03, 0.33, 0.00)	5.44	4.0	V: (0.00, 0.00, 0.00) Se: (-3.03, 0.00, 0.67) (3.03, 0.00, 0.67)
VTe ₂	3.40	3.5	V: (0.00, 0.00, 0.00) Te: (-3.31, 0.34, 0.00) (3.31, 0.33, 0.00)	5.89	3.5	V: (0.00, 0.00, 0.00) Te: (-3.31, 0.00, 0.67) (3.31, 0.00, 0.67)
TaS ₂	3.16	20.0	Ta: (0.00, 0.00, 0.00) S: (-2.96, 0.33, 0.00) (2.96, 0.33, 0.00)	5.46	20.0	Ta: (0.00, 0.00, 0.00) S: (-2.96, 0.00, 0.67) (2.96, 0.00, 0.67)
TaSe ₂	3.28	20.0	Ta: (0.00, 0.00, 0.00) Se: (-3.17, 0.33, 0.00) (3.17, 0.33, 0.00)	5.68	20.0	Ta: (0.00, 0.00, 0.00) Se: (-3.17, 0.00, 0.67) (3.17, 0.00, 0.67)
TaTe ₂	3.46	20.0	Ta: (0.00, 0.00, 0.00) Te: (-3.50, 0.33, 0.00) (3.50, 0.33, 0.00)	5.99	20.0	Ta: (0.00, 0.00, 0.00) Te: (-3.50, 0.00, 0.67) (3.50, 0.00, 0.67)
NbS ₂	3.17	7.5	Nb: (0.00, 0.00, 0.00) S: (-2.96, 0.33, 0.00) (2.96, 0.33, 0.00)	5.48	7.5	Nb: (0.00, 0.00, 0.00) S: (-2.96, 0.00, 0.67) (2.96, 0.00, 0.68)
NbSe ₂	3.29	7.5	Nb: (0.00, 0.00, 0.00) Se: (-3.17, 0.33, 0.00) (3.17, 0.33, 0.00)	5.69	7.5	Nb: (0.00, 0.00, 0.00) Se: (-3.17, 0.00, 0.67) (3.17, 0.00, 0.68)
NbTe ₂	3.49	7.5	Nb: (0.00, 0.00, 0.00) Te: (-3.50, 0.33, 0.00) (3.50, 0.33, 0.00)	6.05	7.5	Nb: (0.00, 0.00, 0.00) Te: (-3.50, 0.00, 0.67) (3.50, 0.00, 0.68)
PtS ₂	3.38	3.0	Pt: (0.00, 0.00, 0.00) S: (-2.33, 0.33, 0.00) (2.33, 0.67, 0.00)	5.85	3.0	Pt: (0.00, 0.00, 0.00) S: (-2.33, 0.50, 0.33) (2.33, 0.00, 0.67)

Table A1. - *continued.*

MX ₂	Armchair			Zigzag		
	Unit cell <i>H</i> (Bohr)	<i>R</i> (nm)	Atom positions (<i>r</i> - <i>R</i> (Bohr), θ , <i>z</i>)	Unit cell <i>H</i> (Bohr)	<i>R</i> (nm)	Atom positions (<i>r</i> - <i>R</i> (Bohr), θ , <i>z</i>)
PtSe ₂	3.54	2.5	Pt: (0.00, 0.00, 0.00) Se: (-2.47, 0.33, 0.00) (2.47, 0.67, 0.00)	6.13	2.5	Pt: (0.00, 0.00, 0.00) Se: (-2.47, 0.50, 0.33) (2.47, 0.00, 0.67)
PtTe ₂	3.80	2.5	Pt: (0.00, 0.00, 0.00) Te: (-2.62, 0.33, 0.00) (2.62, 0.67, 0.00)	6.57	2.5	Pt: (0.00, 0.00, 0.00) Te: (-2.62, 0.50, 0.33) (2.62, 0.00, 0.67)
HfS ₂	3.45	9.5	Hf: (0.00, 0.00, 0.00) S: (-2.74, 0.33, 0.00) (2.74, 0.67, 0.00)	5.98	10.0	Hf: (0.00, 0.00, 0.00) S: (-2.74, 0.50, 0.33) (2.74, 0.00, 0.67)
HfSe ₂	3.56	10.0	Hf: (0.00, 0.00, 0.00) Se: (-2.98, 0.33, 0.00) (2.98, 0.67, 0.00)	6.17	9.5	Hf: (0.00, 0.00, 0.00) Se: (-2.98, 0.50, 0.33) (2.98, 0.00, 0.67)
HfTe ₂	3.76	9.5	Hf: (0.00, 0.00, 0.00) Te: (-3.34, 0.33, 0.00) (3.34, 0.67, 0.00)	6.51	10.0	Hf: (0.00, 0.00, 0.00) Te: (-3.34, 0.50, 0.33) (3.34, 0.00, 0.67)
ZrS ₂	3.48	10.0	Zr: (0.00, 0.00, 0.00) S: (-2.73, 0.33, 0.00) (2.73, 0.67, 0.00)	6.02	10.0	Zr: (0.00, 0.00, 0.00) S: (-2.73, 0.50, 0.33) (2.73, 0.00, 0.67)
ZrSe ₂	3.59	10.0	Zr: (0.00, 0.00, 0.00) Se: (-2.99, 0.33, 0.00) (2.99, 0.67, 0.00)	6.21	9.5	Zr: (0.00, 0.00, 0.00) Se: (-2.99, 0.50, 0.33) (2.99, 0.00, 0.67)
ZrTe ₂	3.75	9.5	Zr: (0.00, 0.00, 0.00) Te: (-3.40, 0.33, 0.00) (3.40, 0.67, 0.00)	6.50	10.0	Zr: (0.00, 0.00, 0.00) Te: (-3.40, 0.50, 0.33) (3.40, 0.00, 0.67)
TiS ₂	3.22	5.5	Ti: (0.00, 0.00, 0.00) S: (-2.69, 0.33, 0.00) (2.69, 0.67, 0.00)	5.59	6.0	Ti: (0.00, 0.00, 0.00) S: (-2.69, 0.50, 0.33) (2.69, 0.00, 0.67)
TiSe ₂	3.34	6.0	Ti: (0.00, 0.00, 0.00) Se: (-2.93, 0.33, 0.00) (2.93, 0.67, 0.00)	5.78	5.5	Ti: (0.00, 0.00, 0.00) Se: (-2.93, 0.50, 0.33) (2.93, 0.00, 0.67)
TiTe ₂	3.54	5.0	Ti: (0.00, 0.00, 0.00) Te: (-3.30, 0.33, 0.00) (3.30, 0.67, 0.00)	6.13	5.5	Ti: (0.00, 0.00, 0.00) Te: (-3.30, 0.50, 0.33) (3.30, 0.00, 0.67)

Table A1. - *continued.*

MX ₂	Armchair			Zigzag		
	Unit cell <i>H</i> (Bohr)	<i>R</i> (nm)	Atom positions (<i>r</i> - <i>R</i> (Bohr), θ , <i>z</i>)	Unit cell <i>H</i> (Bohr)	<i>R</i> (nm)	Atom positions (<i>r</i> - <i>R</i> (Bohr), θ , <i>z</i>)
NiS ₂	3.17	3.5	Ni: (0.00, 0.00, 0.00) S: (-2.22, 0.33, 0.00) (2.22, 0.67, 0.00)	5.49	4.0	Ni: (0.00, 0.00, 0.00) S: (-2.22, 0.50, 0.33) (2.22, 0.00, 0.67)
NiSe ₂	3.34	3.5	Ni: (0.00, 0.00, 0.00) Se: (-2.35, 0.33, 0.00) (2.35, 0.67, 0.00)	5.79	3.5	Ni: (0.00, 0.00, 0.00) Se: (-2.35, 0.50, 0.33) (2.35, 0.00, 0.67)
NiTe ₂	3.58	4.0	Ni: (0.00, 0.00, 0.00) Te: (-2.56, 0.34, 0.00) (2.56, 0.67, 0.00)	6.19	4.0	Ni: (0.00, 0.00, 0.00) Te: (-2.56, 0.50, 0.33) (2.56, 0.00, 0.67)
PdS ₂	3.36	4.0	Pd: (0.00, 0.00, 0.00) S: (-2.35, 0.33, 0.00) (2.35, 0.67, 0.00)	5.81	4.0	Pd: (0.00, 0.00, 0.00) S: (-2.35, 0.50, 0.33) (2.35, 0.00, 0.67)
PdSe ₂	3.53	3.5	Pd: (0.00, 0.00, 0.00) Se: (-2.48, 0.33, 0.00) (2.48, 0.67, 0.00)	6.11	3.5	Pd: (0.00, 0.00, 0.00) Se: (-2.48, 0.50, 0.33) (2.48, 0.00, 0.67)
PdTe ₂	3.79	4.0	Pd: (0.00, 0.00, 0.00) Te: (-2.60, 0.33, 0.00) (2.60, 0.67, 0.00)	6.57	4.0	Pd: (0.00, 0.00, 0.00) Te: (-2.60, 0.50, 0.33) (2.60, 0.00, 0.67)
MnS ₂	2.83	4.0	Mn: (0.00, 0.00, 0.00) S: (-2.50, 0.33, 0.00) (2.50, 0.67, 0.00)	4.91	4.0	Mn: (0.00, 0.00, 0.00) S: (-2.50, 0.50, 0.33) (2.50, 0.00, 0.67)
MnSe ₂	3.06	4.0	Mn: (0.00, 0.00, 0.00) Se: (-2.71, 0.33, 0.00) (2.71, 0.67, 0.00)	5.29	4.0	Mn: (0.00, 0.00, 0.00) Se: (-2.71, 0.50, 0.33) (2.71, 0.00, 0.67)
MnTe ₂	3.32	3.5	Mn: (0.00, 0.00, 0.00) Te: (-2.96, 0.33, 0.00) (2.96, 0.67, 0.00)	5.74	4.0	Mn: (0.00, 0.00, 0.00) Te: (-2.96, 0.50, 0.33) (2.96, 0.00, 0.67)
FeS ₂	2.98	4.0	Fe: (0.00, 0.00, 0.00) S: (-2.59, 0.33, 0.00) (2.59, 0.33, 0.00)	5.16	3.5	Fe: (0.00, 0.00, 0.00) S: (-2.59, 0.00, 0.67) (2.59, 0.00, 0.67)
FeSe ₂	3.13	4.0	Fe: (0.00, 0.00, 0.00) Se: (-2.85, 0.33, 0.00) (2.85, 0.33, 0.00)	5.41	4.0	Fe: (0.00, 0.00, 0.00) Se: (-2.85, 0.00, 0.67) (2.85, 0.00, 0.67)

Table A1. - *continued.*

MX ₂	Armchair			Zigzag		
	Unit cell <i>H</i> (Bohr)	<i>R</i> (nm)	Atom positions (<i>r</i> - <i>R</i> (Bohr), <i>θ</i> , <i>z</i>)	Unit cell <i>H</i> (Bohr)	<i>R</i> (nm)	Atom positions (<i>r</i> - <i>R</i> (Bohr), <i>θ</i> , <i>z</i>)
FeTe ₂	3.38	3.5	Fe: (0.00, 0.00, 0.00) Te: (-3.03, 0.34, 0.00) (3.03, 0.33, 0.00)	5.85	3.5	Fe: (0.00, 0.00, 0.00) Te: (-3.03, 0.00, 0.67) (3.03, 0.00, 0.68)
CuS ₂	3.52	3.5	Cu: (0.00, 0.00, 0.00) S: (-2.03, 0.33, 0.00) (2.03, 0.33, 0.00)	6.10	3.5	Cu: (0.00, 0.00, 0.00) S: (-2.03, 0.00, 0.67) (2.03, 0.00, 0.67)
CuSe ₂	3.63	4.0	Cu: (0.00, 0.00, 0.00) Se: (-2.30, 0.33, 0.00) (2.30, 0.33, 0.00)	6.29	4.0	Cu: (0.00, 0.00, 0.00) Se: (-2.30, 0.00, 0.67) (2.30, 0.00, 0.67)
CuTe ₂	3.70	4.0	Cu: (0.00, 0.00, 0.00) Te: (-2.74, 0.33, 0.00) (2.74, 0.33, 0.00)	6.41	4.0	Cu: (0.00, 0.00, 0.00) Te: (-2.74, 0.00, 0.67) (2.74, 0.00, 0.67)

Table A2. Equilibrium geometry for the twenty-seven Janus TMD nanotubes. The atom positions are $\hat{\mathbf{R}} = r\mathbf{a}_1 + r\mathbf{a}_2 + z\mathbf{a}_3$, where $\mathbf{a}_1 = \cos \frac{2\pi\theta}{\eta} \hat{\mathbf{e}}_1$, $\mathbf{a}_2 = \sin \frac{2\pi\theta}{\eta} \hat{\mathbf{e}}_2$, and $\mathbf{a}_3 = H\hat{\mathbf{e}}_3$, with $\hat{\mathbf{e}}_1$, $\hat{\mathbf{e}}_2$, and $\hat{\mathbf{e}}_3$ being the unit vectors along the x_1 , x_2 , and x_3 directions, respectively. For the armchair and zigzag nanotubes, $\eta = \frac{2\pi R}{\sqrt{3}a}$ and $\eta = \frac{2\pi R}{a}$ respectively. The radius of the nanotube is R . The twist parameter in Cyclix-DFT is $\alpha = \frac{\pi}{\eta H}$

Material	Armchair			Zigzag		
	Unit cell H (Bohr)	R (nm)	Atom positions $(r - R$ (Bohr), θ , z)	Unit cell H (Bohr)	R (nm)	Atom positions $(r - R$ (Bohr), θ , z)
VSSe	3.06	7.3	V: (0.00, 0.00, 0.00) S: (-2.69, 0.33, 0.00) Se: (3.14, 0.33, 0.00)	5.31	7.1	V: (0.00, 0.00, 0.00) S: (-2.69, 0.00, 0.67) Se: (3.14, 0.00, 0.67)
VSTe	3.19	2.2	V: (0.00, 0.00, 0.00) S: (-2.48, 0.33, 0.00) Te: (3.57, 0.33, 0.00)	5.53	2.2	V: (0.00, 0.00, 0.00) S: (-2.48, 0.00, 0.67) Te: (3.57, 0.00, 0.67)
VSeTe	3.26	4.2	V: (0.00, 0.00, 0.00) Se: (-2.75, 0.33, 0.00) Te: (3.46, 0.33, 0.00)	5.65	4.1	V: (0.00, 0.00, 0.00) Se: (-2.75, 0.00, 0.67) Te: (3.46, 0.00, 0.67)
NbSSe	3.22	6.5	Nb: (0.00, 0.00, 0.00) S: (-2.83, 0.33, 0.00) Se: (3.27, 0.33, 0.00)	5.58	7.1	Nb: (0.00, 0.00, 0.00) S: (-2.83, 0.00, 0.67) Se: (3.27, 0.00, 0.67)
NbSTe	3.33	2.2	Nb: (0.00, 0.00, 0.00) S: (-2.64, 0.33, 0.00) Te: (3.70, 0.33, 0.00)	5.77	2.2	Nb: (0.00, 0.00, 0.00) S: (-2.64, 0.00, 0.67) Te: (3.70, 0.00, 0.67)
NbSeTe	3.39	4.3	Nb: (0.00, 0.00, 0.00) Se: (-2.99, 0.33, 0.00) Te: (3.62, 0.33, 0.00)	5.87	4.4	Nb: (0.00, 0.00, 0.00) Se: (-2.99, 0.00, 0.67) Te: (3.62, 0.00, 0.67)
TaSSe	3.22	5.5	Ta: (0.00, 0.00, 0.00) S: (-2.85, 0.33, 0.00) Se: (3.26, 0.33, 0.00)	5.58	5.6	Ta: (0.00, 0.00, 0.00) S: (-2.85, 0.00, 0.67) Se: (3.26, 0.00, 0.67)
TaSTe	3.33	2.0	Ta: (0.00, 0.00, 0.00) S: (-2.68, 0.33, 0.00) Te: (3.68, 0.33, 0.00)	5.76	2.0	Ta: (0.00, 0.00, 0.00) S: (-2.68, 0.00, 0.67) Te: (3.68, 0.00, 0.67)
TaSeTe	3.39	3.8	Ta: (0.00, 0.00, 0.00) Se: (-3.00, 0.33, 0.00) Te: (3.60, 0.33, 0.00)	5.87	3.8	Ta: (0.00, 0.00, 0.00) Se: (-3.00, 0.00, 0.67) Te: (3.60, 0.00, 0.67)
CrSSe	2.96	3.6	Cr: (0.00, 0.00, 0.00) S: (-2.71, 0.33, 0.00) Se: (3.05, 0.33, 0.00)	5.12	3.7	Cr: (0.00, 0.00, 0.00) S: (-2.71, 0.00, 0.67) Se: (3.05, 0.00, 0.67)

Table A2. - *continued.*

Material	Armchair			Zigzag		
	Unit cell	R	Atom positions	Unit cell	R	Atom positions
	H (Bohr)	(nm)	$(r - R \text{ (Bohr)}, \theta, z)$	H (Bohr)	(nm)	$(r - R \text{ (Bohr)}, \theta, z)$
CrSTe	3.07	1.6	Cr: (0.00, 0.00, 0.00) S: (-2.58, 0.33, 0.00) Te: (3.42, 0.33, 0.00)	5.32	1.6	Cr: (0.00, 0.00, 0.00) S: (-2.58, 0.00, 0.67) Te: (3.42, 0.00, 0.67)
CrSeTe	3.16	2.8	Cr: (0.00, 0.00, 0.00) Se: (-2.85, 0.33, 0.00) Te: (3.34, 0.33, 0.00)	5.48	2.8	Cr: (0.00, 0.00, 0.00) Se: (-2.85, 0.00, 0.67) Te: (3.34, 0.00, 0.67)
MoSSe	3.07	4.2	Mo: (0.00, 0.00, 0.00) S: (-2.89, 0.33, 0.00) Se: (3.22, 0.33, 0.00)	5.32	4.2	Mo: (0.00, 0.00, 0.00) S: (-2.89, 0.00, 0.67) Se: (3.22, 0.00, 0.67)
MoSTe	3.18	1.9	Mo: (0.00, 0.00, 0.00) S: (-2.79, 0.33, 0.00) Te: (3.59, 0.33, 0.00)	5.50	1.9	Mo: (0.00, 0.00, 0.00) S: (-2.79, 0.00, 0.67) Te: (3.59, 0.00, 0.67)
MoSeTe	3.24	3.3	Mo: (0.00, 0.00, 0.00) Se: (-3.05, 0.33, 0.00) Te: (3.52, 0.33, 0.00)	5.62	3.2	Mo: (0.00, 0.00, 0.00) Se: (-3.05, 0.00, 0.67) Te: (3.52, 0.00, 0.67)
WSSe	3.07	4.4	W: (0.00, 0.00, 0.00) S: (-2.91, 0.33, 0.00) Se: (3.24, 0.33, 0.00)	5.32	4.5	W: (0.00, 0.00, 0.00) S: (-2.91, 0.00, 0.67) Se: (3.24, 0.00, 0.67)
WSTe	3.18	1.9	W: (0.00, 0.00, 0.00) S: (-2.80, 0.33, 0.00) Te: (3.60, 0.33, 0.00)	5.5	1.9	W: (0.00, 0.00, 0.00) S: (-2.80, 0.00, 0.67) Te: (3.60, 0.00, 0.67)
WSeTe	3.24	3.3	W: (0.00, 0.00, 0.00) Se: (-3.07, 0.33, 0.00) Te: (3.53, 0.33, 0.00)	5.62	3.6	W: (0.00, 0.00, 0.00) Se: (-3.07, 0.00, 0.67) Te: (3.53, 0.00, 0.67)
TiSSe	3.29	21.9	Ti: (0.00, 0.00, 0.00) S: (-2.53, 0.33, 0.00) Se: (3.07, 0.67, 0.00)	5.69	22.4	Ti: (0.00, 0.00, 0.00) S: (-2.53, 0.50, 0.33) Se: (3.07, 0.00, 0.67)
TiSTe	3.39	5.0	Ti: (0.00, 0.00, 0.00) S: (-2.31, 0.33, 0.00) Te: (3.59, 0.67, 0.00)	5.88	4.8	Ti: (0.00, 0.00, 0.00) S: (-2.31, 0.50, 0.33) Te: (3.59, 0.00, 0.67)
TiSeTe	3.44	19.6	Ti: (0.00, 0.00, 0.00) Se: (-2.69, 0.33, 0.00) Te: (3.51, 0.67, 0.00)	5.97	14.3	Ti: (0.00, 0.00, 0.00) Se: (-2.69, 0.50, 0.33) Te: (3.51, 0.00, 0.67)
ZrSSe	3.53	7.7	Zr: (0.00, 0.00, 0.00) S: (-2.62, 0.33, 0.00) Se: (3.10, 0.67, 0.00)	6.12	7.5	Zr: (0.00, 0.00, 0.00) S: (-2.62, 0.50, 0.33) Se: (3.10, 0.00, 0.67)

Table A2. - *continued.*

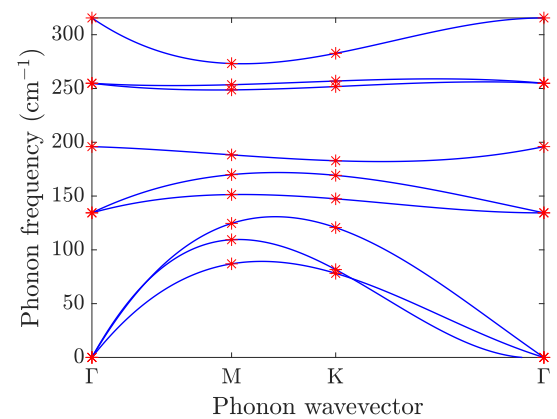
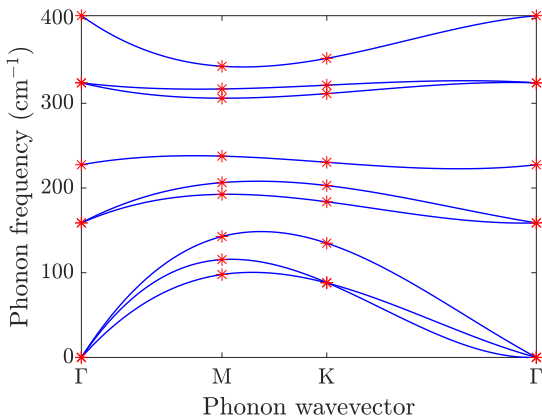
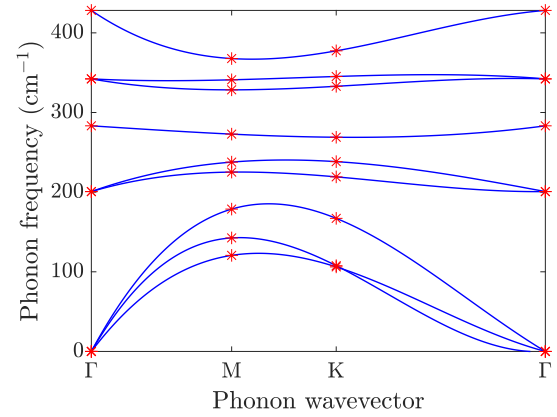
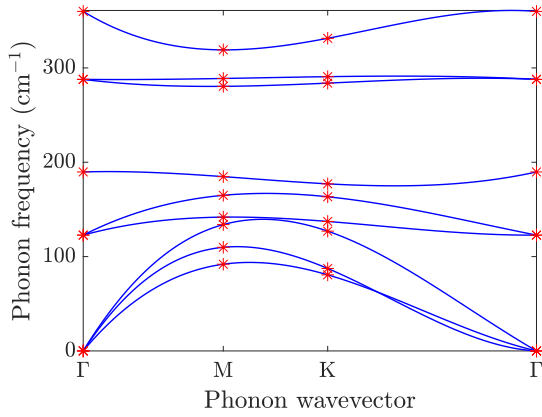
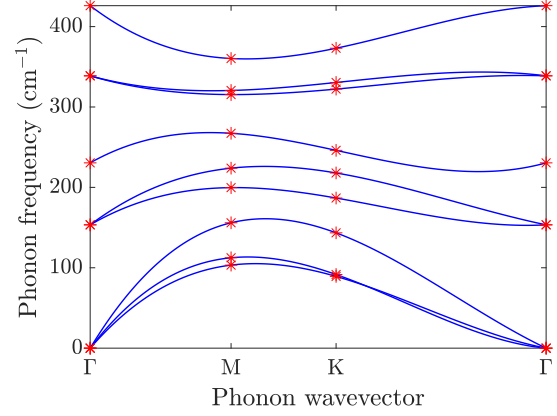
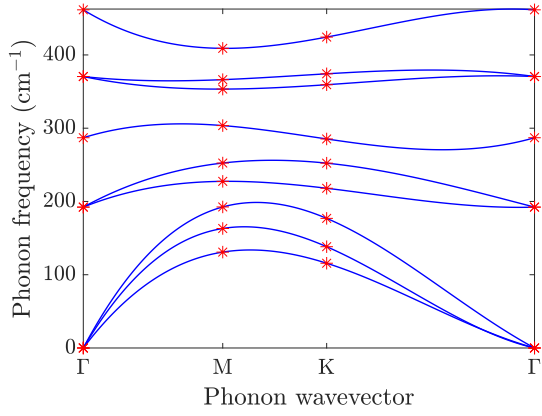
Material	Armchair			Zigzag		
	Unit cell H (Bohr)	R (nm)	Atom positions $(r - R \text{ (Bohr)}, \theta, z)$	Unit cell H (Bohr)	R (nm)	Atom positions $(r - R \text{ (Bohr)}, \theta, z)$
ZrSTe	3.61	3.1	Zr: (0.00, 0.00, 0.00) S: (-2.43, 0.33, 0.00) Te: (3.64, 0.67, 0.00)	6.26	3.1	Zr: (0.00, 0.00, 0.00) S: (-2.43, 0.50, 0.33) Te: (3.64, 0.00, 0.67)
ZrSeTe	3.67	8.3	Zr: (0.00, 0.00, 0.00) Se: (-2.80, 0.33, 0.00) Te: (3.56, 0.67, 0.00)	6.36	7.9	Zr: (0.00, 0.00, 0.00) Se: (-2.80, 0.50, 0.33) Te: (3.56, 0.00, 0.67)
HfSSe	3.51	4.8	Hf: (0.00, 0.00, 0.00) S: (-2.63, 0.33, 0.00) Se: (3.08, 0.67, 0.00)	6.07	5.2	Hf: (0.00, 0.00, 0.00) S: (-2.63, 0.50, 0.33) Se: (3.08, 0.00, 0.67)
HfSTe	3.60	2.2	Hf: (0.00, 0.00, 0.00) S: (-2.45, 0.33, 0.00) Te: (3.59, 0.67, 0.00)	6.23	2.2	Hf: (0.00, 0.00, 0.00) S: (-2.45, 0.50, 0.33) Te: (3.59, 0.00, 0.67)
HfSeTe	3.66	4.1	Hf: (0.00, 0.00, 0.00) Se: (-2.80, 0.33, 0.00) Te: (3.51, 0.67, 0.00)	6.34	4.0	Hf: (0.00, 0.00, 0.00) Se: (-2.80, 0.50, 0.33) Te: (3.51, 0.00, 0.67)

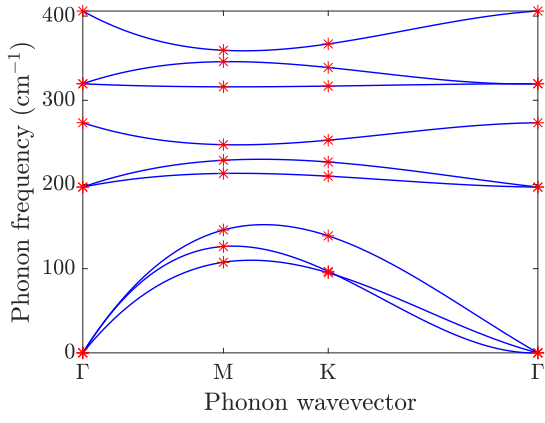
Table A3. Equilibrium geometry for the twelve Janus TMH nanotubes. The atom positions are $\hat{R} = r\mathbf{a}_1 + r\mathbf{a}_2 + z\mathbf{a}_3$, where $\mathbf{a}_1 = \cos \frac{2\pi\theta}{\eta} \hat{e}_1$, $\mathbf{a}_2 = \sin \frac{2\pi\theta}{\eta} \hat{e}_2$, and $\mathbf{a}_3 = H\hat{e}_3$, with \hat{e}_1 , \hat{e}_2 , and \hat{e}_3 being the unit vectors along the x_1 , x_2 , and x_3 directions, respectively. For the armchair and zigzag nanotubes, $\eta = \frac{2\pi R}{\sqrt{3}a}$ and $\frac{2\pi R}{a}$, respectively. The radius of the nanotube is R . The twist parameter in Cyclix-DFT is $\alpha = \frac{\pi}{\eta H}$.

Material	Armchair			Zigzag		
	Unit cell	R	Atom positions	Unit cell	R	Atom positions
	H (Bohr)	(nm)	$(r - R$ (Bohr), θ , z)	H (Bohr)	(nm)	$(r - R$ (Bohr), θ , z)
TiClI	3.35	1.6 ± 0.1	Ti: (0.00, 0.00, 0.00) Cl: (-2.83, 0.33, 0.00) I: (3.54, 0.33, 0.00)	5.77	1.6 ± 0.1	Ti: (0.00, 0.00, 0.00) Cl: (-2.83, 0.00, 0.67) I: (3.54, 0.00, 0.67)
TiBrI	3.43	3.1 ± 0.2	Ti: (0.00, 0.00, 0.00) Br: (-3.11, 0.33, 0.00) I: (3.49, 0.33, 0.00)	5.94	3.0 ± 0.1	Ti: (0.00, 0.00, 0.00) Br: (-3.11, 0.00, 0.67) I: (3.49, 0.00, 0.67)
TiClBr	3.19	3.7 ± 0.2	Ti: (0.00, 0.00, 0.00) Cl: (-2.93, 0.33, 0.00) Br: (3.25, 0.33, 0.00)	5.53	3.9 ± 0.2	Ti: (0.00, 0.00, 0.00) Cl: (-2.93, 0.00, 0.67) Br: (3.25, 0.00, 0.67)
ZrClI	3.43	2.0 ± 0.1	Zr: (0.00, 0.00, 0.00) Cl: (-3.08, 0.33, 0.00) I: (3.79, 0.33, 0.00)	5.92	1.9 ± 0.1	Zr: (0.00, 0.00, 0.00) Cl: (-3.08, 0.00, 0.67) I: (3.79, 0.00, 0.67)
ZrBrI	3.50	3.5 ± 0.2	Zr: (0.00, 0.00, 0.00) Br: (-3.36, 0.33, 0.00) I: (3.74, 0.33, 0.00)	6.06	3.3 ± 0.2	Zr: (0.00, 0.00, 0.00) Br: (-3.36, 0.00, 0.67) I: (3.74, 0.00, 0.67)
ZrClBr	3.29	4.3 ± 0.4	Zr: (0.00, 0.00, 0.00) Cl: (-3.18, 0.33, 0.00) Br: (3.50, 0.33, 0.00)	5.71	4.4 ± 0.4	Zr: (0.00, 0.00, 0.00) Cl: (-3.18, 0.00, 0.67) Br: (3.50, 0.00, 0.67)
HfClI	3.38	1.9 ± 0.1	Hf: (0.00, 0.00, 0.00) Cl: (-3.12, 0.33, 0.00) I: (3.81, 0.33, 0.00)	5.82	1.9 ± 0.1	Hf: (0.00, 0.00, 0.00) Cl: (-3.12, 0.00, 0.67) I: (3.81, 0.00, 0.67)
HfBrI	3.44	3.4 ± 0.2	Hf: (0.00, 0.00, 0.00) Br: (-3.40, 0.33, 0.00) I: (3.76, 0.33, 0.00)	5.96	3.4 ± 0.2	Hf: (0.00, 0.00, 0.00) Br: (-3.40, 0.00, 0.67) I: (3.76, 0.00, 0.67)
HfClBr	3.24	4.3 ± 0.3	Hf: (0.00, 0.00, 0.00) Cl: (-3.22, 0.33, 0.00) Br: (3.53, 0.33, 0.00)	5.61	4.3 ± 0.2	Hf: (0.00, 0.00, 0.00) Cl: (-3.22, 0.00, 0.67) Br: (3.53, 0.00, 0.67)
FeClI	3.46	1.5 ± 0.1	Fe: (0.00, 0.00, 0.00) Cl: (-2.30, 0.33, 0.00) I: (2.59, 0.67, 0.00)	5.99	1.4 ± 0.1	Fe: (0.00, 0.00, 0.00) Cl: (-2.30, 0.50, 0.33) I: (2.59, 0.00, 0.67)
FeBrI	3.54	2.9 ± 0.1	Fe: (0.00, 0.00, 0.00) Br: (-2.49, 0.33, 0.00) I: (2.60, 0.67, 0.00)	6.13	3.0 ± 0.1	Fe: (0.00, 0.00, 0.00) Br: (-2.49, 0.50, 0.33) I: (2.60, 0.00, 0.67)
FeClBr	3.31	2.5 ± 0.2	Fe: (0.00, 0.00, 0.00) Cl: (-2.28, 0.33, 0.00) Br: (2.46, 0.67, 0.00)	5.73	2.4 ± 0.2	Fe: (0.00, 0.00, 0.00) Cl: (-2.28, 0.50, 0.33) Br: (2.46, 0.00, 0.67)

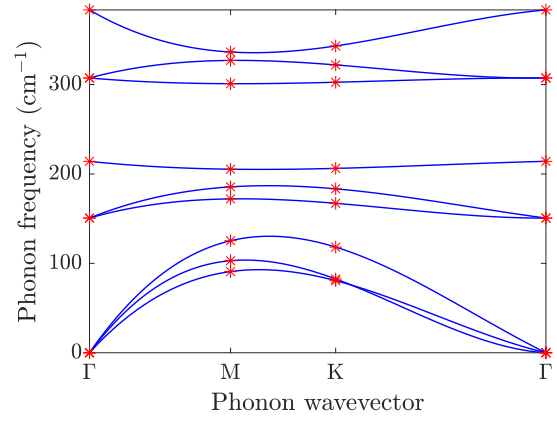
APPENDIX B

MONOLAYER STABILITY

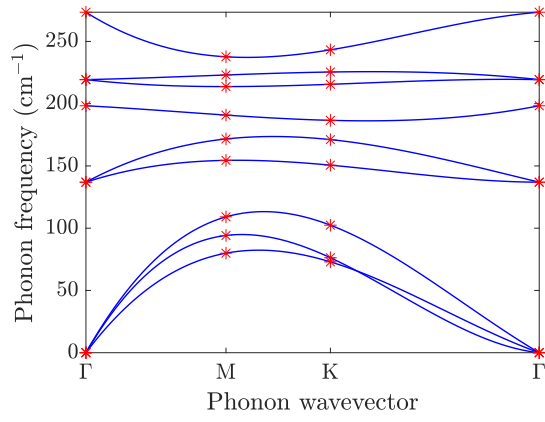




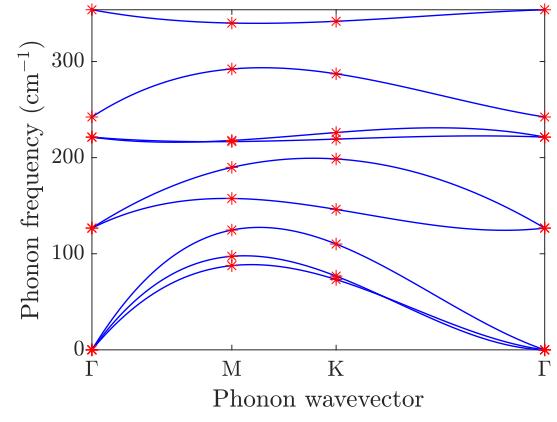
(7) WSSe



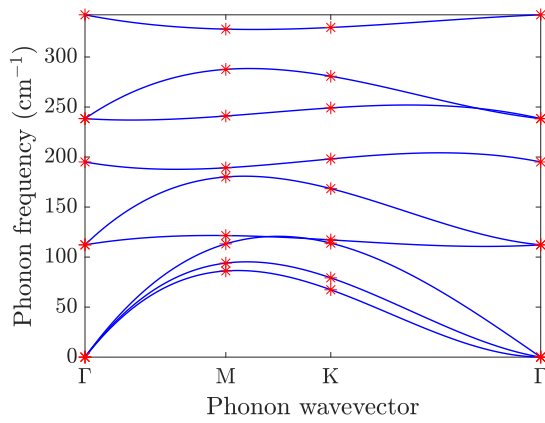
(8) WSTe



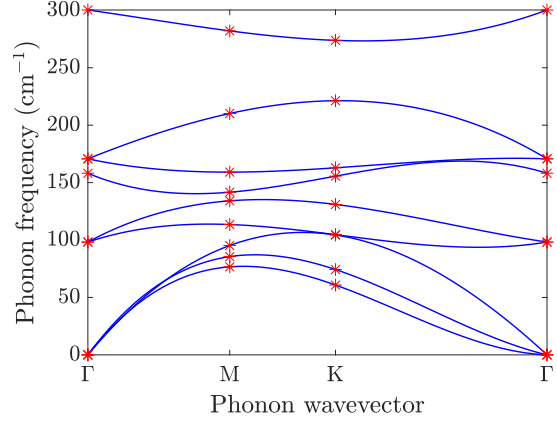
(9) WSeTe



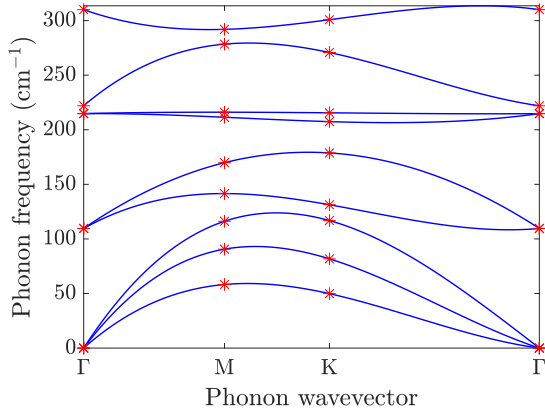
(10) TiSSe



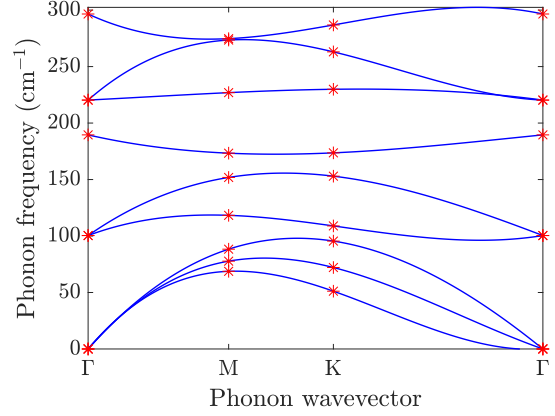
(11) TiSTe



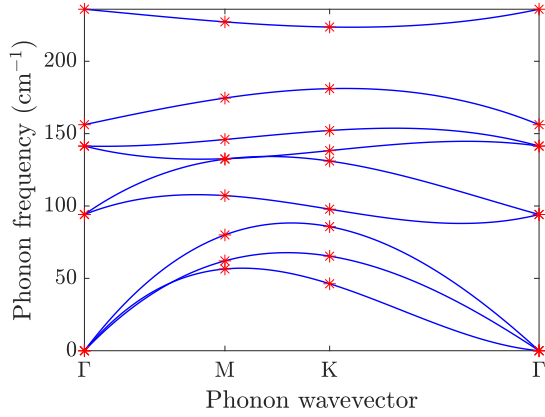
(12) TiSeTe



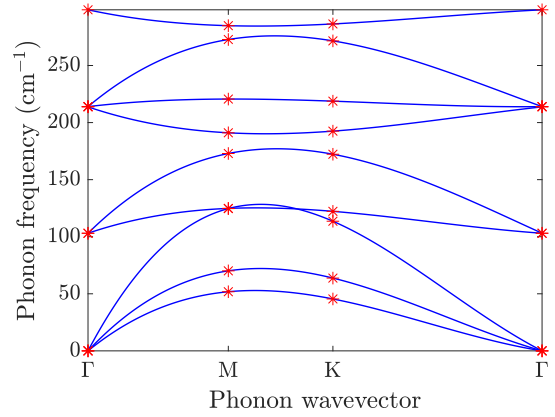
(13) ZrSSe



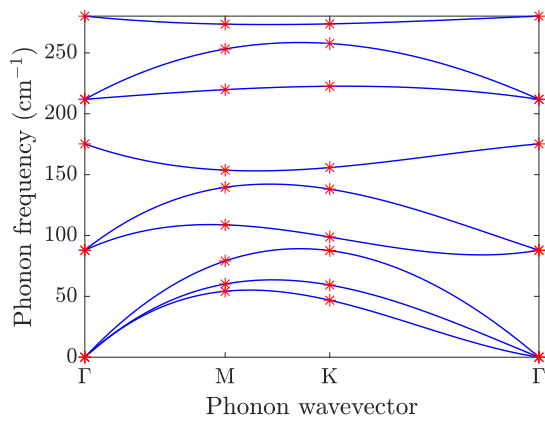
(14) ZrSTe



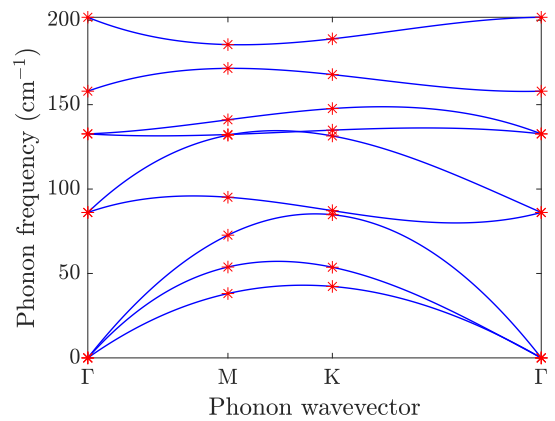
(15) ZrSeTe



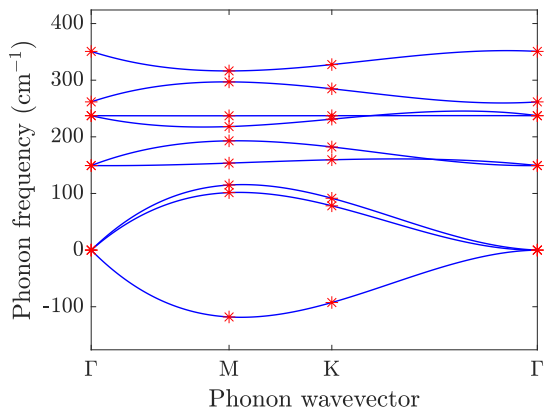
(16) HfSTe



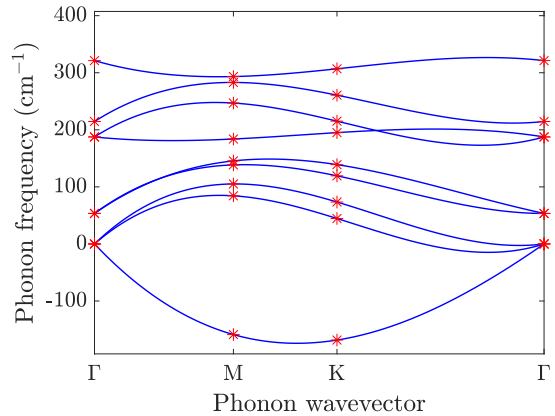
(17) HfSTe



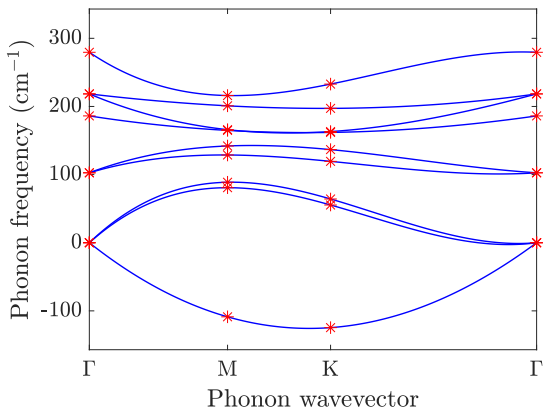
(18) HfSeTe



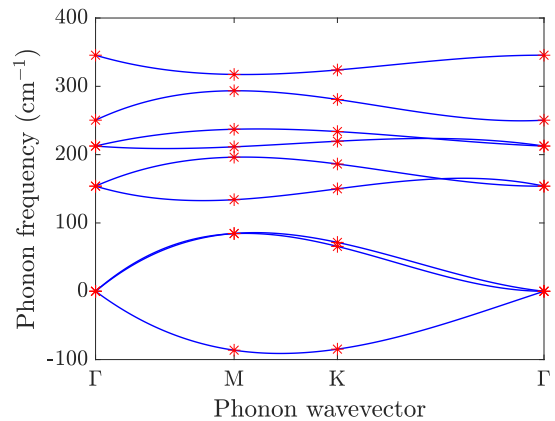
(19) NbSSe



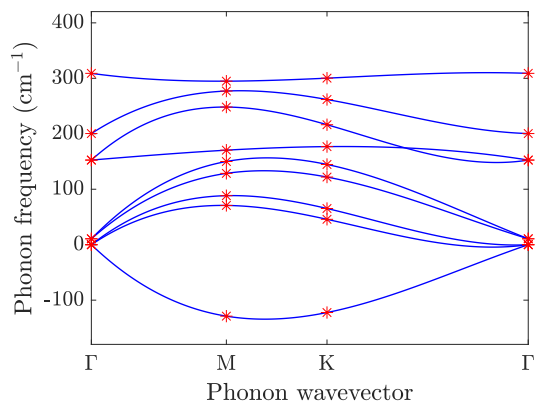
(20) NbSTe



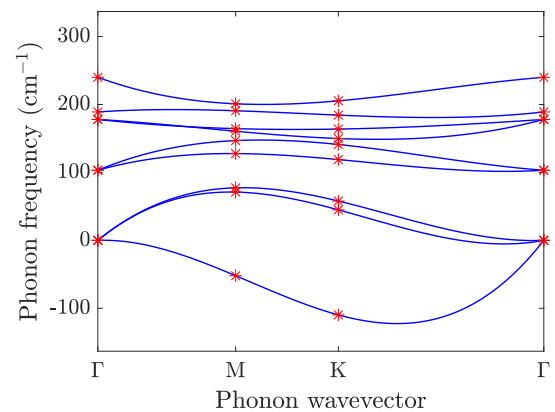
(21) NbSeTe



(22) TaSSe



(23) TaSTe



(24) TaSeTe

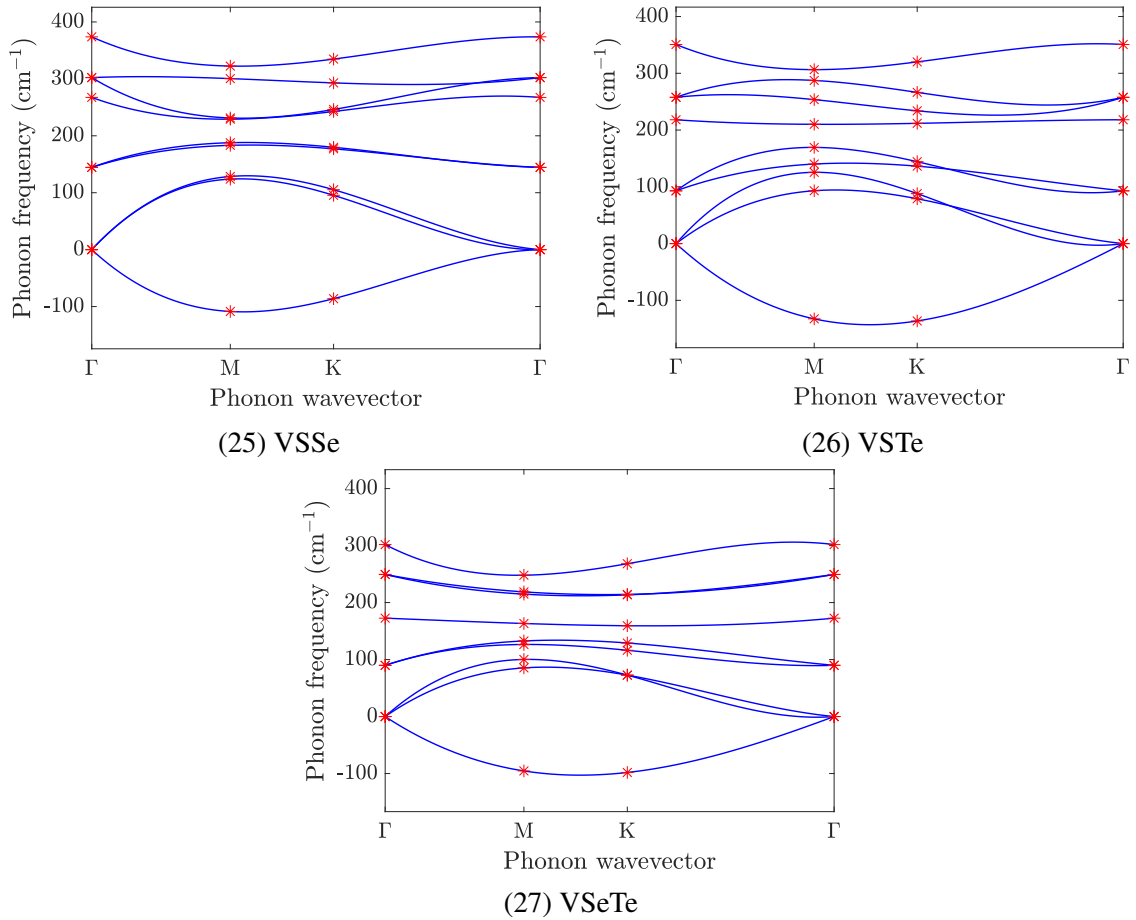
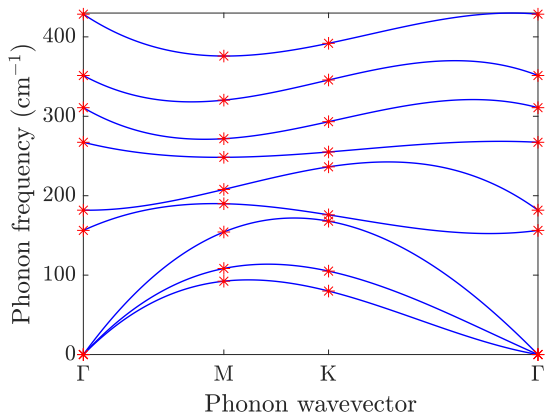
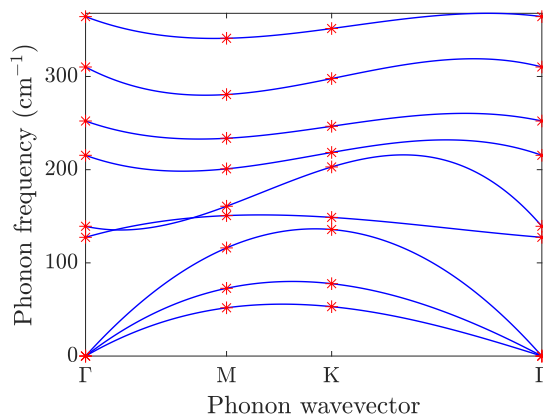


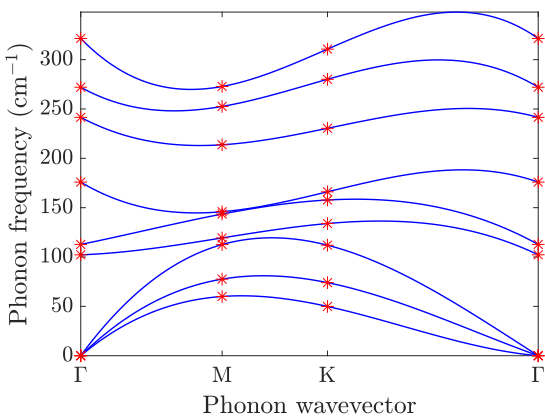
Figure B1: Phonon band structure plots for the twenty-seven select Janus TMD monolayers at their equilibrium configuration.



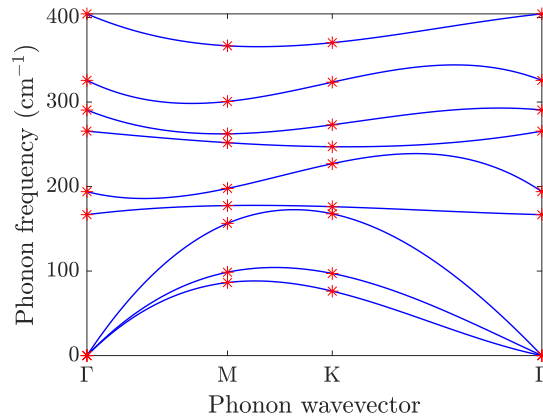
(1) CrSSe ($\epsilon = 0.14$)



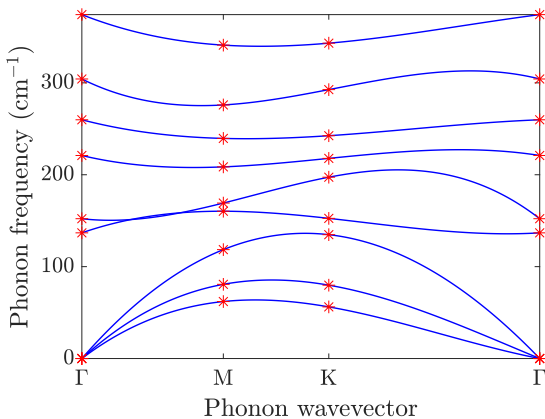
(2) CrSTe ($\epsilon = 0.14$)



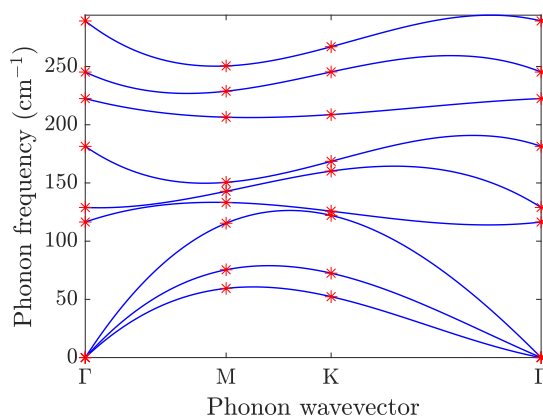
(3) CrSeTe ($\epsilon = 0.14$)



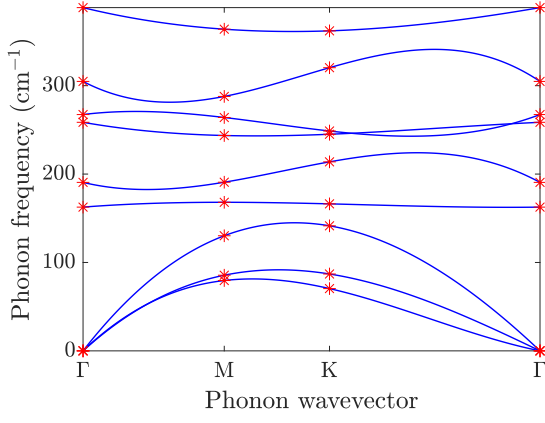
(4) MoSSe ($\epsilon = 0.14$)



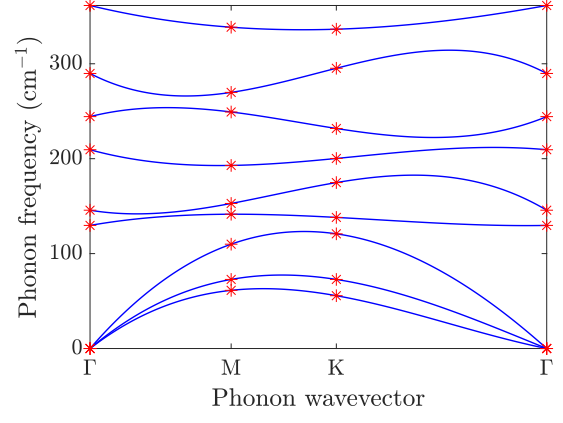
(5) MoSTe ($\epsilon = 0.14$)



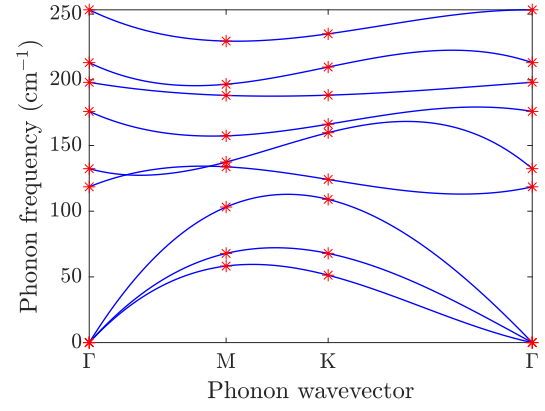
(6) MoSeTe ($\epsilon = 0.14$)



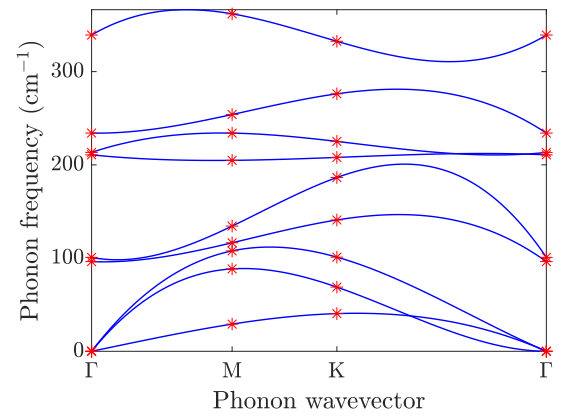
(7) WSSe ($\varepsilon = 0.14$)



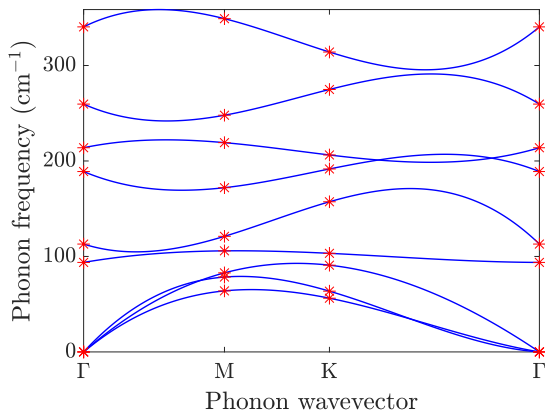
(8) WSTe ($\varepsilon = 0.14$)



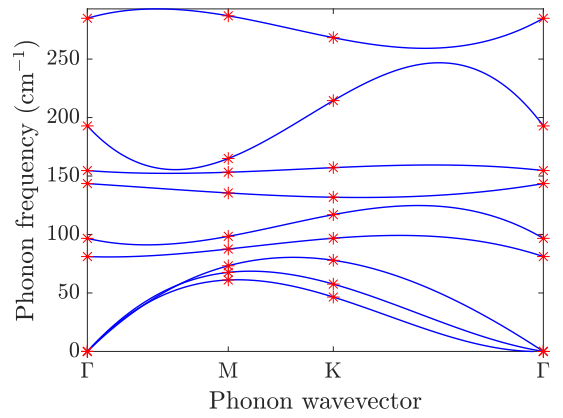
(9) WSeTe ($\varepsilon = 0.14$)



(10) TiSSe ($\varepsilon = 0.05$)



(11) TiSTe ($\varepsilon = 0.14$)



(12) TiSeTe ($\varepsilon = 0.14$)

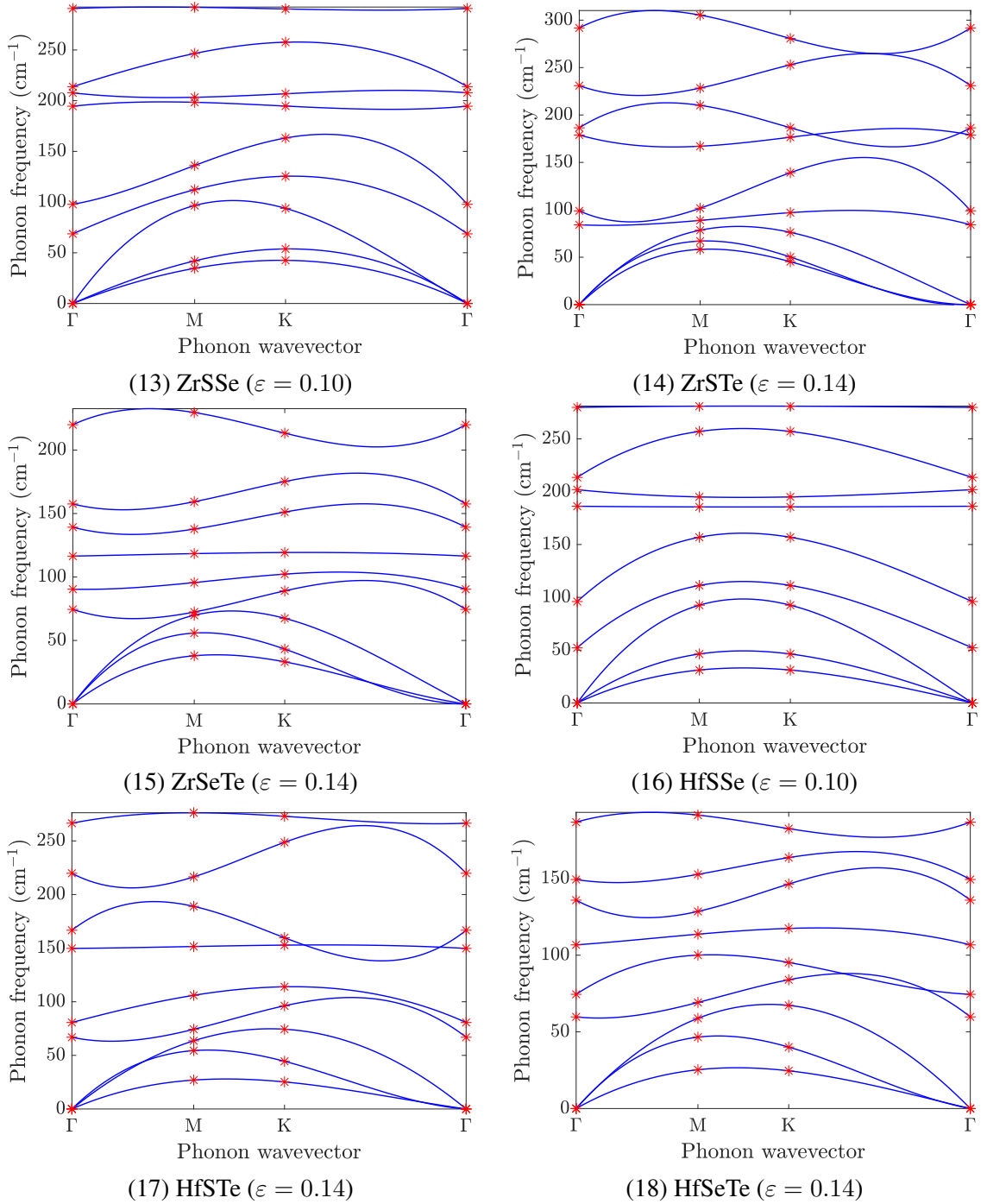
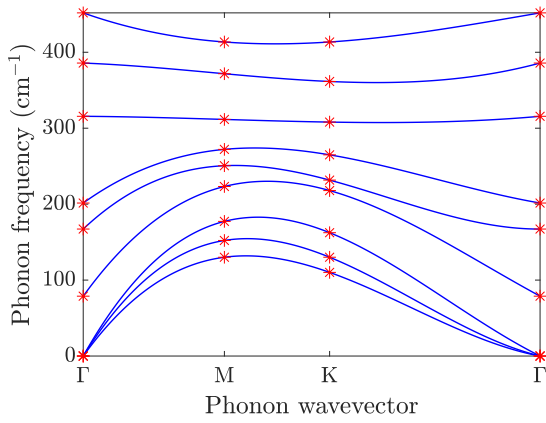
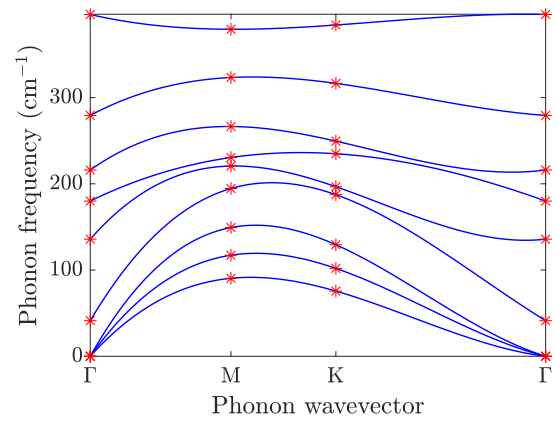


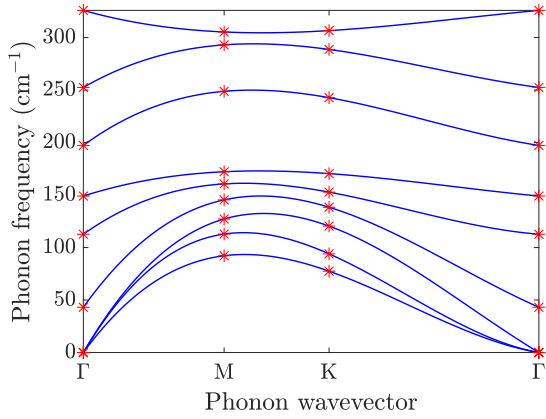
Figure B2: Phonon band structure plots for the eighteen select Janus TMD monolayers at the maximum tensile strain for which they are stable.



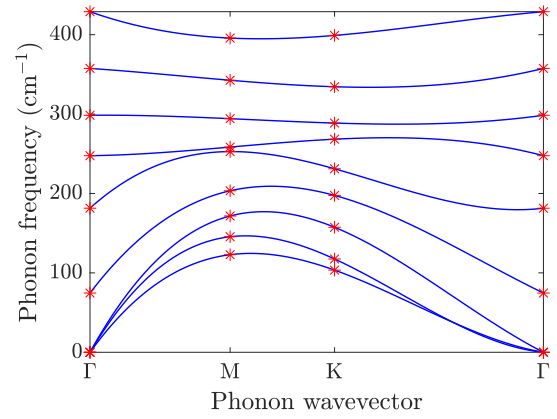
(1) CrSSe ($\gamma = 0.15$)



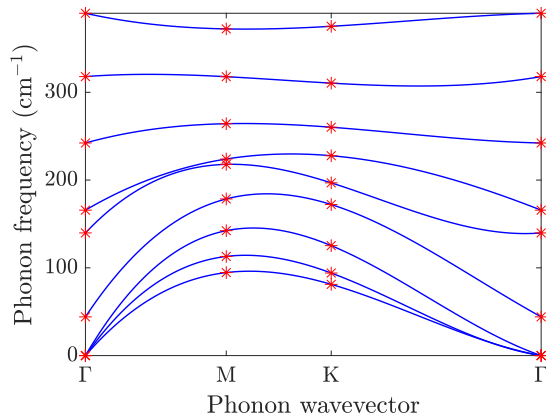
(2) CrSTe ($\gamma = 0.15$)



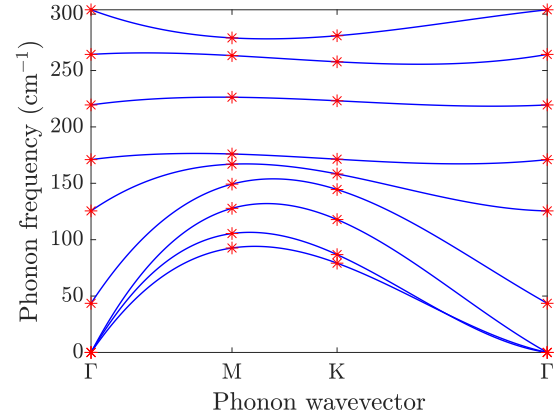
(3) CrSeTe ($\gamma = 0.15$)



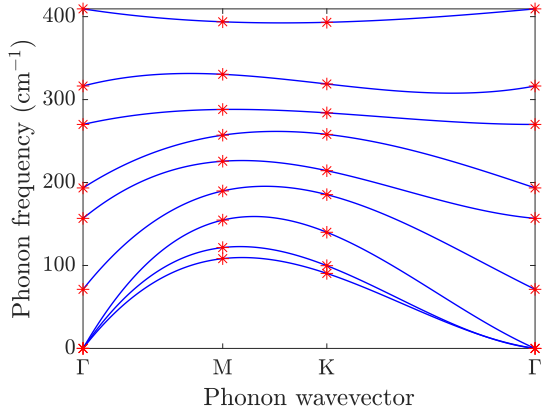
(4) MoSSe ($\gamma = 0.15$)



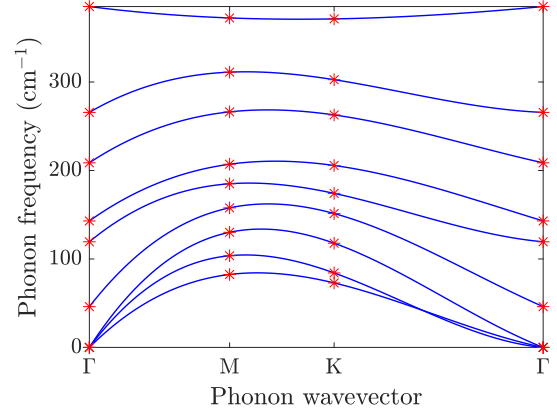
(5) MoSTe ($\gamma = 0.15$)



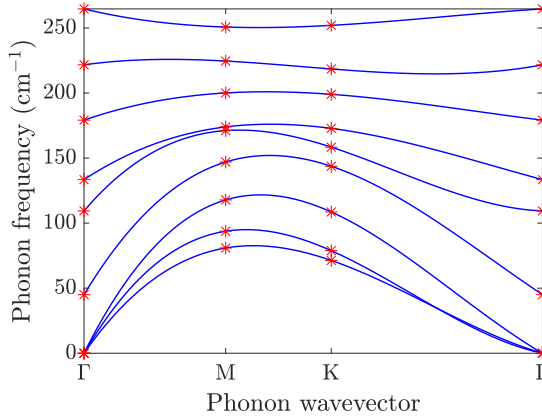
(6) MoSeTe ($\gamma = 0.15$)



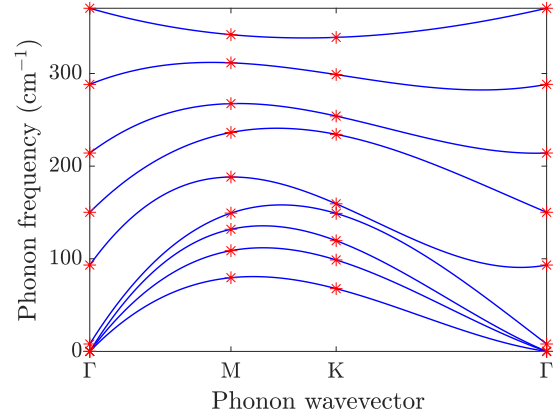
(7) WSSe ($\gamma = 0.15$)



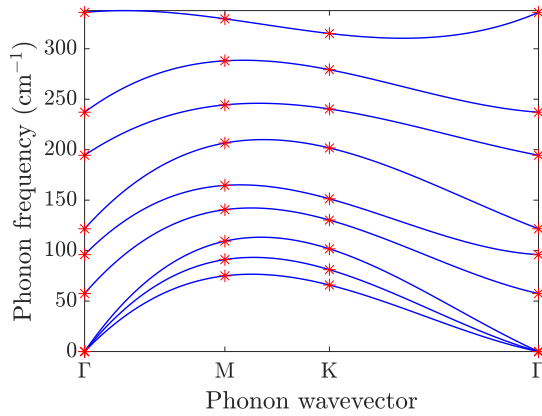
(8) WSTe ($\gamma = 0.15$)



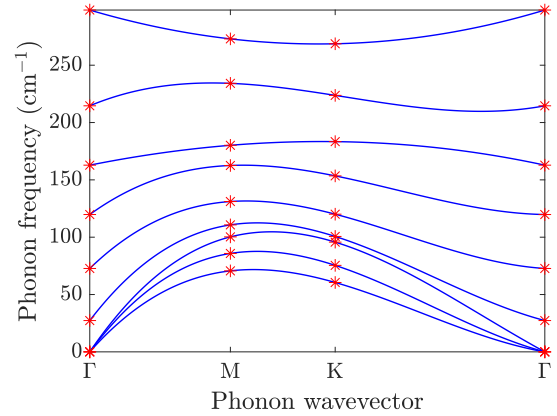
(9) WSeTe ($\gamma = 0.15$)



(10) TiSSe ($\gamma = 0.05$)



(11) TiSTe ($\gamma = 0.15$)



(12) TiSeTe ($\gamma = 0.15$)

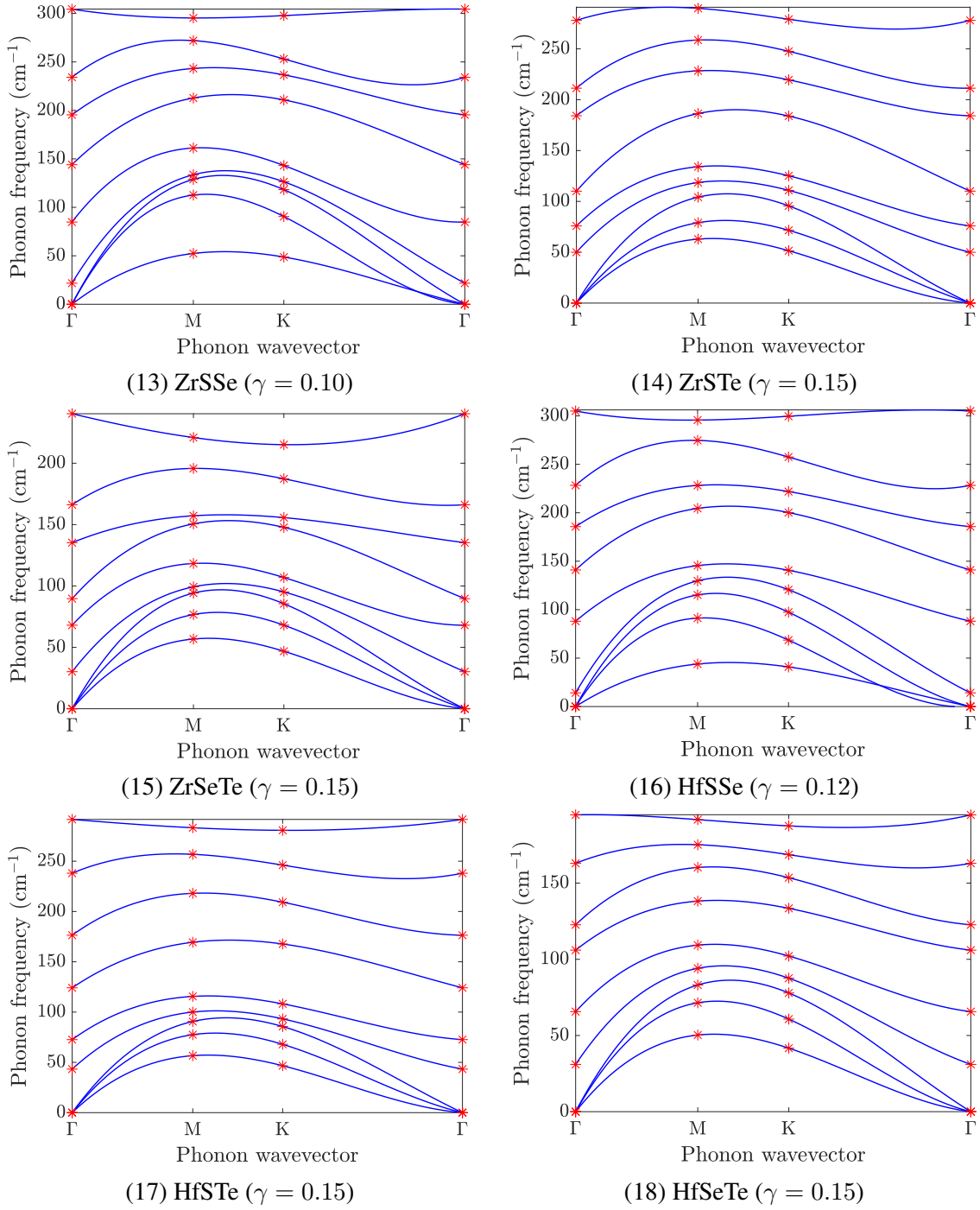


Figure B3: Phonon band structure plots for the eighteen select Janus TMD monolayers at the maximum shear strain for which they are stable.

REFERENCES

- [1] S. Iijima, "Helical microtubules of graphitic carbon," *Nature*, vol. 354, no. 6348, pp. 56–58, 1991.
- [2] R. Tenne, "Advances in the synthesis of inorganic nanotubes and fullerene-like nanoparticles," *Angewandte Chemie International Edition*, vol. 42, no. 42, pp. 5124–5132, 2003.
- [3] C. N. R. Rao and M. Nath, "Inorganic nanotubes," in *Advances In Chemistry: A Selection of CNR Rao's Publications (1994–2003)*, World Scientific, 2003, pp. 310–333.
- [4] M. Serra, R. Arenal, and R. Tenne, "An overview of the recent advances in inorganic nanotubes," *Nanoscale*, vol. 11, no. 17, pp. 8073–8090, 2019.
- [5] S. Haastrup, M. Strange, M. Pandey, T. Deilmann, P. S. Schmidt, N. F. Hinsche, M. N. Gjerding, D. Torelli, P. M. Larsen, A. C. Riis-Jensen, *et al.*, "The Computational 2D Materials Database: high-throughput modeling and discovery of atomically thin crystals," *2D Materials*, vol. 5, no. 4, p. 042 002, 2018.
- [6] J. Zhou, L. Shen, M. D. Costa, K. A. Persson, S. P. Ong, P. Huck, Y. Lu, X. Ma, Y. Chen, H. Tang, *et al.*, "2D MatPedia, an open computational database of two-dimensional materials from top-down and bottom-up approaches," *Scientific Data*, vol. 6, no. 1, pp. 1–10, 2019.
- [7] M. N. Gjerding, A. Taghizadeh, A. Rasmussen, S. Ali, F. Bertoldo, T. Deilmann, U. P. Holguin, N. R. Knøsgaard, M. Kruse, S. Manti, *et al.*, "Recent Progress of the Computational 2D Materials Database (C2DB)," *2D Materials*, vol. 8, no. 4, p. 044 002, 2021.
- [8] S. Ghosh, A. S. Banerjee, and P. Suryanarayana, "Symmetry-adapted real-space density functional theory for cylindrical geometries: Application to large group-IV nanotubes," *Physical Review B*, vol. 100, no. 12, p. 125 143, 2019.
- [9] A. Maiti, "Bandgap engineering with strain," *Nature Materials*, vol. 2, no. 7, pp. 440–442, 2003.
- [10] D.-B. Zhang, E. Akatyeva, and T. Dumitrică, "Helical bn and zno nanotubes with intrinsic twisting: An objective molecular dynamics study," *Physical Review B*, vol. 84, no. 11, p. 115 431, 2011.
- [11] G. Y. Guo and J. C. Lin, "Systematic ab initio study of the optical properties of BN nanotubes," *Physical Review B*, vol. 71, no. 16, p. 165 402, 2005.

- [12] J.-F. Jia, H.-S. Wu, and H. Jiao, "The structure and electronic property of BN nanotube," *Physica B: Condensed Matter*, vol. 381, no. 1-2, pp. 90–95, 2006.
- [13] X. Yang and J. Ni, "Electronic properties of single-walled silicon nanotubes compared to carbon nanotubes," *Physical Review B*, vol. 72, no. 19, p. 195 426, 2005.
- [14] J. W. Mintmire, D. H. Robertson, and C. T. White, "Properties of fullerene nanotubules," *Journal of Physics and Chemistry of Solids*, vol. 54, no. 12, pp. 1835–1840, 1993.
- [15] C. Wang, X. Fu, Y. Guo, Z. Guo, C. Xia, and Y. Jia, "Band gap scaling laws in group IV nanotubes," *Nanotechnology*, vol. 28, no. 11, p. 115 202, 2017.
- [16] J. W. Ding, X. H. Yan, and J. X. Cao, "Analytical relation of band gaps to both chirality and diameter of single-wall carbon nanotubes," *Physical Review B*, vol. 66, no. 7, p. 073 401, 2002.
- [17] M. Ouyang, J.-L. Huang, and C. M. Lieber, "Fundamental electronic properties and applications of single-walled carbon nanotubes," *Accounts of Chemical Research*, vol. 35, no. 12, pp. 1018–1025, 2002.
- [18] H. Wang, N. Ding, T. Jiang, X. Zhao, W. Liu, and F. Zai, "Investigation on mechanical and electronic properties of graphene-doped boron nitride nanotubes," *Materials Research Express*, vol. 6, no. 11, p. 1150c5, 2019.
- [19] V. Parashar, C. P. Durand, B. Hao, R. G. Amorim, R. Pandey, B. Tiwari, D. Zhang, Y. Liu, A.-P. Li, and Y. K. Yap, "Switching behaviors of graphene-boron nitride nanotube heterojunctions," *Scientific Reports*, vol. 5, no. 1, pp. 1–6, 2015.
- [20] B. Akdim and R. Pachter, "Bandgap Tuning of a (6, 6) Boron Nitride Nanotube by Analyte Physisorption and Application of a Transverse Electric Field: A DFT Study," *IEEE Transactions on Nanotechnology*, vol. 10, no. 5, pp. 1089–1092, 2011.
- [21] L.-G. Tien, C.-H. Tsai, F.-Y. Li, and M.-H. Lee, "Band-gap modification of defective carbon nanotubes under a transverse electric field," *Physical Review B*, vol. 72, no. 24, p. 245 417, 2005.
- [22] C.-W. Chen, M.-H. Lee, and S. J. Clark, "Band gap modification of single-walled carbon nanotube and boron nitride nanotube under a transverse electric field," *Nanotechnology*, vol. 15, no. 12, p. 1837, 2004.
- [23] L. Yang and J. Han, "Electronic structure of deformed carbon nanotubes," *Physical Review Letters*, vol. 85, no. 1, p. 154, 2000.

- [24] A. Rochefort, P. Avouris, F. Lesage, and D. R. Salahub, "Electrical and mechanical properties of distorted carbon nanotubes," *Physical Review B*, vol. 60, no. 19, p. 13 824, 1999.
- [25] T. W. Tombler, C. Zhou, L. Alexseyev, J. Kong, H. Dai, L. Liu, C. S. Jayanthi, M. Tang, and S.-Y. Wu, "Reversible electromechanical characteristics of carbon nanotubes under local-probe manipulation," *Nature*, vol. 405, no. 6788, pp. 769–772, 2000.
- [26] L. Yang, M. P. Anantram, J. Han, and J. P. Lu, "Band-gap change of carbon nanotubes: Effect of small uniaxial and torsional strain," *Physical Review B*, vol. 60, no. 19, p. 13 874, 1999.
- [27] Y.-H. Kim, K.-J. Chang, and S. G. Louie, "Electronic structure of radially deformed BN and BC₃ nanotubes," *Physical Review B*, vol. 63, no. 20, p. 205 408, 2001.
- [28] Y. Kinoshita and N. Ohno, "Electronic structures of boron nitride nanotubes subjected to tension, torsion, and flattening: A first-principles DFT study," *Physical Review B*, vol. 82, no. 8, p. 085 433, 2010.
- [29] S. S. Coutinho, V. Lemos, and S. Guerini, "Band-gap tunability of a (6, 0) BN nanotube bundle under pressure: Ab initio calculations," *Physical Review B*, vol. 80, no. 19, p. 193 408, 2009.
- [30] H. M. Ghassemi, C. H. Lee, Y. K. Yap, and R. S. Yassar, "Field emission and strain engineering of electronic properties in boron nitride nanotubes," *Nanotechnology*, vol. 23, no. 10, p. 105 702, 2012.
- [31] G. Seifert, H. Terrones, M. Terrones, G. Jungnickel, and T. Frauenheim, "Structure and electronic properties of MoS₂ nanotubes," *Physical Review Letters*, vol. 85, no. 1, p. 146, 2000.
- [32] G. Seifert, H. Terrones, M. Terrones, G. Jungnickel, and T. Frauenheim, "On the electronic structure of WS₂ nanotubes," *Solid State Communications*, vol. 114, no. 5, pp. 245–248, 2000.
- [33] G. Seifert, H. Terrones, M. Terrones, and T. Frauenheim, "Novel NbS₂ metallic nanotubes," *Solid State Communications*, vol. 115, no. 12, pp. 635–638, 2000.
- [34] A. N. Enyashin, I. R. Shein, N. I. Medvedeva, and A. L. Ivanovskii, "Computational studies of 1T and 2H TaS₂ in crystalline and nanotubular forms: structural and electronic properties," *Internet Electronic Journal of Molecular Design*, vol. 4, pp. 316–328, 2005.

- [35] M. Nath, S. Kar, A. K. Raychaudhuri, and C. N. R. Rao, “Superconducting NbSe₂ nanostructures,” *Chemical Physics Letters*, vol. 368, no. 5-6, pp. 690–695, 2003.
- [36] T. Tsuneta, T. Toshima, K. Inagaki, T. Shibayama, S. Tanda, S. Uji, M. Ahlskog, P. Hakonen, and M. Paalanen, “Formation of metallic NbSe₂ nanotubes and nanofibers,” *Current Applied Physics*, vol. 3, no. 6, pp. 473–476, 2003.
- [37] A. Kis, D. Mihailovic, M. Remskar, A. Mrzel, A. Jesih, I. Piwonski, A. J. Kulik, W. Benoit, and L. Forró, “Shear and Young’s moduli of MoS₂ nanotube ropes,” *Advanced Materials*, vol. 15, no. 9, pp. 733–736, 2003.
- [38] I. Kaplan-Ashiri and R. Tenne, “Mechanical properties of WS₂ nanotubes,” *Journal of Cluster Science*, vol. 18, no. 3, pp. 549–563, 2007.
- [39] I. Kaplan-Ashiri, S. R. Cohen, K. Gartsman, V. Ivanovskaya, T. Heine, G. Seifert, I. Wiesel, H. D. Wagner, and R. Tenne, “On the mechanical behavior of WS₂ nanotubes under axial tension and compression,” *Proceedings of the National Academy of Sciences*, vol. 103, no. 3, pp. 523–528, 2006.
- [40] D.-M. Tang, X. Wei, M.-S. Wang, N. Kawamoto, Y. Bando, C. Zhi, M. Mitome, A. Zak, R. Tenne, and D. Golberg, “Revealing the anomalous tensile properties of WS₂ nanotubes by in situ transmission electron microscopy,” *Nano Letters*, vol. 13, no. 3, pp. 1034–1040, 2013.
- [41] N. Zibouche, M. Ghorbani-Asl, T. Heine, and A. Kuc, “Electromechanical properties of small transition-metal dichalcogenide nanotubes,” *Inorganics*, vol. 2, no. 2, pp. 155–167, 2014.
- [42] S. Oshima, M. Toyoda, and S. Saito, “Geometrical and electronic properties of unstrained and strained transition metal dichalcogenide nanotubes,” *Physical Review Materials*, vol. 4, no. 2, p. 026 004, 2020.
- [43] W. Li, G. Zhang, M. Guo, and Y.-W. Zhang, “Strain-tunable electronic and transport properties of MoS₂ nanotubes,” *Nano Research*, vol. 7, no. 4, pp. 518–527, 2014.
- [44] Y. Z. Wang, R. Huang, X. Q. Wang, Q. F. Zhang, B. L. Gao, L. Zhou, and G. Hua, “Strain-tunable electronic properties of CrS₂ nanotubes,” *Chalcogenide Letters*, vol. 13, no. 7, pp. 301–307, 2016.
- [45] M. Ghorbani-Asl, N. Zibouche, M. Wahiduzzaman, A. F. Oliveira, A. Kuc, and T. Heine, “Electromechanics in MoS₂ and WS₂: nanotubes vs. monolayers,” *Scientific Reports*, vol. 3, p. 2961, 2013.

- [46] P. Lu, X. Wu, W. Guo, and X. C. Zeng, “Strain-dependent electronic and magnetic properties of MoS₂ monolayer, bilayer, nanoribbons and nanotubes,” *Physical Chemistry Chemical Physics*, vol. 14, no. 37, pp. 13 035–13 040, 2012.
- [47] R. Ansari, S. Malakpour, M. Faghinasiri, and S. Sahmani, “An ab initio investigation into the elastic, structural and electronic properties of MoS₂ nanotubes,” *Superlattices and Microstructures*, vol. 82, pp. 188–200, 2015.
- [48] R. Levi, J. Garel, D. Teich, G. Seifert, R. Tenne, and E. Joselevich, “Nanotube electromechanics beyond carbon: the case of WS₂,” *ACS Nano*, vol. 9, no. 12, pp. 12 224–12 232, 2015.
- [49] A. Bhardwaj, A. Sharma, and P. Suryanarayana, “Torsional strain engineering of transition metal dichalcogenide nanotubes: An ab initio study,” *Nanotechnology*, vol. 32, no. 47, 47LT01, 2021.
- [50] M. Pardo, T. Shuster-Meiseles, S. Levin-Zaidman, A. Rudich, and Y. Rudich, “Low cytotoxicity of inorganic nanotubes and fullerene-like nanostructures in human bronchial epithelial cells: relation to inflammatory gene induction and antioxidant response,” *Environmental Science & Technology*, vol. 48, no. 6, pp. 3457–3466, 2014.
- [51] V. V. Ivanovskaya, A. N. Enyashin, N. I. Medvedeva, Y. N. Makurin, and A. L. Ivanovskii, “Computational studies of electronic properties of ZrS₂ nanotubes,” *Internet Electronic Journal of Molecular Design*, vol. 2, pp. 499–510, 2003.
- [52] V. V. Ivanovskaya and G. Seifert, “Tubular structures of titanium disulfide TiS₂,” *Solid State Communications*, vol. 130, no. 3-4, pp. 175–180, 2004.
- [53] B.-L. Gao, S.-H. Ke, G. Song, J. Zhang, L. Zhou, G.-N. Li, F. Liang, Y. Wang, and C. Dang, “Structural and electronic properties of zigzag and armchair WSe₂ nanotubes,” *Journal of Alloys and Compounds*, vol. 695, pp. 2751–2756, 2017.
- [54] D. Yin, M. Wu, Y. Yang, W. Cen, and H. Fang, “Chiral vectors-tunable electronic property of MoS₂ nanotubes,” *Physica E: Low-dimensional Systems and Nanostructures*, vol. 84, pp. 196–201, 2016.
- [55] I. Milošević, B. Nikolić, E. Dobardžić, M. Damnjanović, I. Popov, and G. Seifert, “Electronic properties and optical spectra of MoS₂ and WS₂ nanotubes,” *Physical Review B*, vol. 76, no. 23, p. 233 414, 2007.
- [56] D. Teich, T. Lorenz, J.-O. Joswig, G. Seifert, D.-B. Zhang, and T. Dumitrica, “Structural and electronic properties of helical TiS₂ nanotubes studied with objective molecular dynamics,” *The Journal of Physical Chemistry C*, vol. 115, no. 14, pp. 6392–6396, 2011.

- [57] L. Scheffer, R. Rosentzveig, A. Margolin, R. Popovitz-Biro, G. Seifert, S. R. Cohen, and R. Tenne, "Scanning tunneling microscopy study of WS₂ nanotubes," *Physical Chemistry Chemical Physics*, vol. 4, no. 11, pp. 2095–2098, 2002.
- [58] N. Zibouche, A. Kuc, and T. Heine, "From layers to nanotubes: Transition metal disulfides TMS₂," *The European Physical Journal B*, vol. 85, no. 1, p. 49, 2012.
- [59] O. Tal, M. Remskar, R. Tenne, and G. Haase, "The effect of substrate topography on the local electronic structure of WS₂ nanotubes," *Chemical Physics Letters*, vol. 344, no. 5-6, pp. 434–440, 2001.
- [60] N. Li, G. Lee, Y. H. Jeong, and K. S. Kim, "Tailoring electronic and magnetic properties of MoS₂ nanotubes," *The Journal of Physical Chemistry C*, vol. 119, no. 11, pp. 6405–6413, 2015.
- [61] Y. Z. Wang, B. L. Wang, Q. F. Zhang, R. Huang, B. L. Gao, F. J. Kong, and X. Q. Wang, "Tuning structural and electronic properties of MoS₂ nanotubes by transverse electric field," *Chalcogenide Letters*, vol. 11, no. 10, pp. 493–502, 2014.
- [62] N. Zibouche, P. Philipsen, and A. Kuc, "Strong variation of electronic properties of MoS₂ and WS₂ nanotubes in the presence of external electric fields," *The Journal of Physical Chemistry C*, vol. 123, no. 6, pp. 3892–3899, 2019.
- [63] M. Shtein, R. Nativ, N. Lachman, H. D. Wagner, and O. Regev, "Fracture behavior of nanotube–polymer composites: Insights on surface roughness and failure mechanism," *Composites Science and Technology*, vol. 87, pp. 157–163, 2013.
- [64] G. Otorgust, H. Dodiuk, S. Kenig, and R. Tenne, "Important insights into polyurethane nanocomposite-adhesives; a comparative study between INT-WS₂ and CNT," *European Polymer Journal*, vol. 89, pp. 281–300, 2017.
- [65] D. M. Simić, D. B. Stojanović, M. Dimić, K. Mišković, M. Marjanović, Z. Burzić, P. S. Uskoković, A. Zak, and R. Tenne, "Impact resistant hybrid composites reinforced with inorganic nanoparticles and nanotubes of WS₂," *Composites Part B: Engineering*, vol. 176, p. 107 222, 2019.
- [66] R. Nativ, M. Shtein, M. Refaeli, A. Peled, and O. Regev, "The critical role of nanotube shape in cement composites," *Cement and Concrete Composites*, vol. 71, pp. 166–174, 2016.
- [67] S.-J. Huang, C.-H. Ho, Y. Feldman, and R. Tenne, "Advanced AZ31 Mg alloy composites reinforced by WS₂ nanotubes," *Journal of Alloys and Compounds*, vol. 654, pp. 15–22, 2016.

- [68] M. Naffakh, A. M. Diez-Pascual, and C. Marco, “Polymer blend nanocomposites based on poly (l-lactic acid), polypropylene and WS₂ inorganic nanotubes,” *RSC Advances*, vol. 6, no. 46, pp. 40 033–40 044, 2016.
- [69] D. Yudilevich, R. Levi, I. Nevo, R. Tenne, A. Ya’akobovitz, and E. Joselevich, “Self-sensing torsional resonators based on inorganic nanotubes,” *ICME*, pp. 1–4, 2018.
- [70] Y. Divon, R. Levi, J. Garel, D. Golberg, R. Tenne, A. Ya’akobovitz, and E. Joselevich, “Torsional resonators based on inorganic nanotubes,” *Nano Letters*, vol. 17, no. 1, pp. 28–35, 2017.
- [71] G. Lalwani, A. M. Henslee, B. Farshid, P. Parmar, L. Lin, Y.-X. Qin, F. K. Kasper, A. G. Mikos, and B. Sitharaman, “Tungsten disulfide nanotubes reinforced biodegradable polymers for bone tissue engineering,” *Acta Biomaterialia*, vol. 9, no. 9, pp. 8365–8373, 2013.
- [72] H. E. Unalan, Y. Yang, Y. Zhang, P. Hiralal, D. Kuo, S. Dalal, T. Butler, S. N. Cha, J. E. Jang, K. Chremmou, *et al.*, “ZnO Nanowire and WS₂ nanotubes Electronics,” *IEEE Transactions on Electron Devices*, vol. 55, no. 11, pp. 2988–3000, 2008.
- [73] C. Zhang, S. Wang, L. Yang, Y. Liu, T. Xu, Z. Ning, A. Zak, Z. Zhang, R. Tenne, and Q. Chen, “High-performance photodetectors for visible and near-infrared lights based on individual WS₂ nanotubes,” *Applied Physics Letters*, vol. 100, no. 24, p. 243 101, 2012.
- [74] Y. J. Zhang, T. Ideue, M. Onga, F. Qin, R. Suzuki, A. Zak, R. Tenne, J. H. Smet, and Y. Iwasa, “Enhanced intrinsic photovoltaic effect in tungsten disulfide nanotubes,” *Nature*, vol. 570, no. 7761, pp. 349–353, 2019.
- [75] B. L. Li, J. Wang, H. L. Zou, S. Garaj, C. T. Lim, J. Xie, N. B. Li, and D. T. Leong, “Low-dimensional transition metal dichalcogenide nanostructures based sensors,” *Advanced Functional Materials*, vol. 26, no. 39, pp. 7034–7056, 2016.
- [76] V. Sorkin, H. Pan, H. Shi, S. Y. Quek, and Y. W. Zhang, “Nanoscale transition metal dichalcogenides: structures, properties, and applications,” *Critical Reviews in Solid State and Materials Sciences*, vol. 39, no. 5, pp. 319–367, 2014.
- [77] S. Barua, H. S. Dutta, R. Gogoi S Devi, and R. Khan, “Nanostructured MoS₂-based advanced biosensors: a review,” *ACS Applied Nano Materials*, vol. 1, no. 1, pp. 2–25, 2017.
- [78] S. Kumar and P. Suryanarayana, “Bending moduli for forty-four select atomic monolayers from first principles,” *Nanotechnology*, vol. 31, no. 43, 43LT01, 2020.

- [79] M. Yagmurcukardes, Y. Qin, S. Ozen, M. Sayyad, F. M. Peeters, S. Tongay, and H. Sahin, “Quantum properties and applications of 2D Janus crystals and their superlattices,” *Applied Physics Reviews*, vol. 7, no. 1, p. 011 311, 2020.
- [80] Q.-L. Xiong, J. Zhou, J. Zhang, T. Kitamura, and Z.-H. Li, “Spontaneous curling of freestanding Janus monolayer transition-metal dichalcogenides,” *Physical Chemistry Chemical Physics*, vol. 20, no. 32, pp. 20 988–20 995, 2018.
- [81] A. Bhardwaj and P. Suryanarayana, “Elastic properties of Janus transition metal dichalcogenide nanotubes from first principles,” *The European Physical Journal B*, vol. 95, no. 1, pp. 1–8, 2022.
- [82] A.-Y. Lu, H. Zhu, J. Xiao, C.-P. Chuu, Y. Han, M.-H. Chiu, C.-C. Cheng, C.-W. Yang, K.-H. Wei, Y. Yang, *et al.*, “Janus monolayers of transition metal dichalcogenides,” *Nature Nanotechnology*, vol. 12, no. 8, pp. 744–749, 2017.
- [83] J. Zhang, S. Jia, I. Kholmanov, L. Dong, D. Er, W. Chen, H. Guo, Z. Jin, V. B. Shenoy, L. Shi, *et al.*, “Janus monolayer transition-metal dichalcogenides,” *ACS Nano*, vol. 11, no. 8, pp. 8192–8198, 2017.
- [84] D. B. Trivedi, G. Turgut, Y. Qin, M. Y. Sayyad, D. Hajra, M. Howell, L. Liu, S. Yang, N. H. Patoary, H. Li, *et al.*, “Room-Temperature Synthesis of 2D Janus Crystals and their Heterostructures,” *Advanced Materials*, vol. 32, no. 50, p. 2 006 320, 2020.
- [85] Y.-C. Lin, C. Liu, Y. Yu, E. Zarkadoula, M. Yoon, A. A. Puretzky, L. Liang, Y. Kong Xand Gu, A. Strasser, *et al.*, “Low energy implantation into transition-metal dichalcogenide monolayers to form Janus structures,” *ACS Nano*, vol. 14, no. 4, pp. 3896–3906, 2020.
- [86] Z.-K. Tang, B. Wen, M. Chen, and L.-M. Liu, “Janus MoSSe nanotubes: tunable band gap and excellent optical properties for surface photocatalysis,” *Advanced Theory and Simulations*, vol. 1, no. 10, p. 1 800 082, 2018.
- [87] S. Xie, H. Jin, Y. Wei, and S. Wei, “Theoretical investigation on stability and electronic properties of Janus MoSSe nanotubes for optoelectronic applications,” *Optik*, vol. 227, p. 166 105, 2021.
- [88] L. Ju, P. Liu, Y. Yang, L. Shi, G. Yang, and L. Sun, “Tuning the photocatalytic water-splitting performance with the adjustment of diameter in an armchair WSSe nanotube,” *Journal of Energy Chemistry*, vol. 61, pp. 228–235, 2021.
- [89] L. Ju, J. Qin, G. Shi Land Yang, J. Zhang, and L. Sun, “Rolling the WSSe bilayer into double-walled nanotube for the enhanced photocatalytic water-splitting performance,” *Nanomaterials*, vol. 11, no. 3, p. 705, 2021.

- [90] S. Zhang, H. Jin, C. Long, T. Wang, R. Peng, B. Huang, and Y. Dai, “MoSSe nanotube: a promising photocatalyst with an extremely long carrier lifetime,” *Journal of Materials Chemistry A*, vol. 7, no. 13, pp. 7885–7890, 2019.
- [91] F. T. Bølle, A. E. G. Mikkelsen, K. S. Thygesen, T. Vegge, and I. E. Castelli, “Structural and chemical mechanisms governing stability of inorganic Janus nanotubes,” *npj Computational Materials*, vol. 7, no. 1, pp. 1–8, 2021.
- [92] C.-C. Chiu, C.-Y. Wang, B.-J. Huang, and J.-L. Kuo, “Electronic properties of 3 d transition metal dihalide monolayers predicted by DFT methods: Is there a pattern or are the results random?” *Journal of the Chinese Chemical Society*, 2023.
- [93] K. Saritas and S. Ismail-Beigi, “Piezoelectric ferromagnetism in two-dimensional materials via materials screening,” *Physical Review B*, vol. 106, no. 13, p. 134 421, 2022.
- [94] R. Li, J. Jiang, W. Mi, and H. Bai, “Room temperature spontaneous valley polarization in two-dimensional FeClBr monolayer,” *Nanoscale*, vol. 13, no. 35, pp. 14 807–14 813, 2021.
- [95] S.-D. Guo, J.-X. Zhu, M.-Y. Yin, and B.-G. Liu, “Substantial electronic correlation effects on the electronic properties in a Janus FeClF monolayer,” *Physical Review B*, vol. 105, no. 10, p. 104 416, 2022.
- [96] I. Kaplan-Ashiri, S. R. Cohen, K. Gartsman, R. Rosentsveig, G. Seifert, and R. Tenne, “Mechanical behavior of individual WS₂ nanotubes,” *Journal of Materials Research*, vol. 19, no. 2, pp. 454–459, 2004.
- [97] M. S. Wang, I. Kaplan-Ashiri, X. L. Wei, R. Rosentsveig, H. D. Wagner, R. Tenne, and L. M. Peng, “In situ TEM measurements of the mechanical properties and behavior of WS₂ nanotubes,” *Nano Research*, vol. 1, no. 1, p. 22, 2008.
- [98] A. Grillo, M. Passacantando, A. Zak, A. Pelella, and A. D. Bartolomeo, “WS₂ Nanotubes: Electrical conduction and field emission under electron irradiation and mechanical stress,” *Small*, vol. 16, no. 35, p. 2 002 880, 2020.
- [99] A. V. Bandura, S. I. Lukyanov, R. A. Evarestov, and D. D. Kuruch, “Calculation of Young’s modulus of MoS₂-based single-wall nanotubes using force-field and hybrid density functional theory,” *Physics of the Solid State*, vol. 60, no. 12, pp. 2551–2558, 2018.
- [100] Q.-L. Xiong, J. Zhang, C. Xiao, and Z.-H. Li, “Effects of atomic vacancies and temperature on the tensile properties of single-walled MoS₂ nanotubes,” *Physical Chemistry Chemical Physics*, vol. 19, no. 30, pp. 19 948–19 958, 2017.

- [101] P. Ying, J. Zhang, J. Zhou, Q. Liang, and Z. Zhong, “Mechanical behaviors of MoS nanowires under tension from molecular dynamics simulations,” *Computational Materials Science*, vol. 179, p. 109 691, 2020.
- [102] J. Xiao, M. Long, X. Li, H. Xu, H. Huang, and Y. Gao, “Theoretical prediction of electronic structure and carrier mobility in single-walled MoS₂ nanotubes,” *Scientific Reports*, vol. 4, no. 1, pp. 1–7, 2014.
- [103] T. Lorenz, D. Teich, J.-O. Joswig, and G. Seifert, “Theoretical study of the mechanical behavior of individual TiS₂ and MoS₂ nanotubes,” *The Journal of Physical Chemistry C*, vol. 116, no. 21, pp. 11 714–11 721, 2012.
- [104] E. Kalfon-Cohen, D. Barlam, O. Tevet, and S. R. Cohen, “Insights on uniaxial compression of WS₂ inorganic fullerenes: A finite element study,” *Journal of Materials Research*, vol. 27, no. 1, p. 161, 2012.
- [105] Y. Z. Wang, R. Huang, B. L. Gao, G. Hu, F. Liang, and Y. L. Ma, “Mechanical and strain-tunable electronic properties of Janus MoSSe nanotubes,” *Chalcogenide Letters*, vol. 15, no. 11, pp. 535–543, 2018.
- [106] K. S. Nagapriya, O. Goldbart, I. Kaplan-Ashiri, G. Seifert, R. Tenne, and E. Joselevich, “Torsional stick-slip behavior in WS₂ nanotubes,” *Physical Review Letters*, vol. 101, no. 19, p. 195 501, 2008.
- [107] D.-B. Zhang, T. Dumitrică, and G. Seifert, “Helical nanotube structures of MoS₂ with intrinsic twisting: an objective molecular dynamics study,” *Physical Review Letters*, vol. 104, no. 6, p. 065 502, 2010.
- [108] E. W. Bucholz and S. B. Sinnott, “Mechanical behavior of MoS₂ nanotubes under compression, tension, and torsion from molecular dynamics simulations,” *Journal of Applied Physics*, vol. 112, no. 12, p. 123 510, 2012.
- [109] P. Hohenberg and W. Kohn, “Inhomogeneous electron gas,” *Physical Review*, vol. 136, no. 3B, B864, 1964.
- [110] W. Kohn and L. J. Sham, “Self-consistent equations including exchange and correlation effects,” *Physical Review*, vol. 140, no. 4A, A1133, 1965.
- [111] A. Sharma and P. Suryanarayana, “Real-space density functional theory adapted to cyclic and helical symmetry: Application to torsional deformation of carbon nanotubes,” *Physical Review B*, vol. 103, no. 3, p. 035 101, 2021.
- [112] H.-H. Wu, Q. Meng, H. Huang, C. T. Liu, and X.-L. Wang, “Tuning the indirect–direct band gap transition in the MoS_{2-x}Se_x armchair nanotube by diameter modulation,” *Physical Chemistry Chemical Physics*, vol. 20, no. 5, pp. 3608–3613, 2018.

- [113] A. E. G. Mikkelsen, F. T. Bølle, K. S. Thygesen, T. Vegge, and I. E. Castelli, “Band structure of MoSTe Janus nanotubes,” *Physical Review Materials*, vol. 5, no. 1, p. 014 002, 2021.
- [114] W. Zhao, Y. Li, W. Duan, and F. Ding, “Ultra-stable small diameter hybrid transition metal dichalcogenide nanotubes X–M–Y (X, Y= S, Se, Te; M= Mo, W, Nb, Ta): a computational study,” *Nanoscale*, vol. 7, no. 32, pp. 13 586–13 590, 2015.
- [115] L. Tao, Y.-Y. Zhang, J. Sun, S. Du, and H.-J. Gao, “Band engineering of double-wall Mo-based hybrid nanotubes,” *Chinese Physics B*, vol. 27, no. 7, p. 076 104, 2018.
- [116] R. A. Evarestov, A. V. Kovalenko, and A. V. Bandura, “First-principles study on stability, structural and electronic properties of monolayers and nanotubes based on pure Mo(W)S(Se)₂ and mixed (Janus)Mo(W)SSe dichalcogenides,” *Physica E: Low-dimensional Systems and Nanostructures*, vol. 115, p. 113 681, 2020.
- [117] Y. F. Luo, Y. Pang, M. Tang, Q. Song, and M. Wang, “Electronic properties of Janus MoSSe nanotubes,” *Computational Materials Science*, vol. 156, pp. 315–320, 2019.
- [118] M. Nath and C. N. R. Rao, “Nanotubes of group 4 metal disulfides,” *Angewandte Chemie International Edition*, vol. 41, no. 18, pp. 3451–3454, 2002.
- [119] A. V. Bandura and R. A. Evarestov, “TiS₂ and ZrS₂ single- and double-wall nanotubes: First-principles study,” *Journal of Computational Chemistry*, vol. 35, no. 5, pp. 395–405, 2014.
- [120] M. Nath and C. N. R. Rao, “MoSe₂ and WSe₂ nanotubes and related structures,” *Chemical Communications*, vol. 1, no. 21, pp. 2236–2237, 2001.
- [121] M. Nath, A. Govindaraj, and C. N. R. Rao, “Simple synthesis of MoS₂ and WS₂ nanotubes,” *Advanced Materials*, vol. 13, no. 4, pp. 283–286, 2001.
- [122] J. Chen, S.-L. Li, Z.-L. Tao, Y.-T. Shen, and C.-X. Cui, “Titanium disulfide nanotubes as hydrogen-storage materials,” *Journal of the American Chemical Society*, vol. 125, no. 18, pp. 5284–5285, 2003.
- [123] M. Nath and C. N. R. Rao, “New metal disulfide nanotubes,” *Journal of the American Chemical Society*, vol. 123, no. 20, pp. 4841–4842, 2001.
- [124] A. R. Tenne, L. Margulis, M. Genut, and G. Hodes, “Polyhedral and cylindrical structures of tungsten disulphide,” *Nature*, vol. 360, no. 6403, pp. 444–446, 1992.

- [125] J. M. Gordon, E. A. Katz, D. Feuermann, A. Albu-Yaron, M. Levy, and R. Tenne, “Singular MoS₂, SiO₂ and Si nanostructures—synthesis by solar ablation,” *Journal of Materials Chemistry*, vol. 18, no. 4, pp. 458–462, 2008.
- [126] V. Brüser, R. Popovitz-Biro, A. Albu-Yaron, T. Lorenz, G. Seifert, R. Tenne, and A. Zak, “Single-to triple-wall WS₂ nanotubes obtained by high-power plasma ablation of WS₂ multiwall nanotubes,” *Inorganics*, vol. 2, no. 2, pp. 177–190, 2014.
- [127] M. Remskar, A. Mrzel, Z. Skraba, A. Jesih, M. Ceh, J. Demšar, P. Stadelmann, F. Lévy, and D. Mihailovic, “Self-assembly of subnanometer-diameter single-wall MoS₂ nanotubes,” *Science*, vol. 292, no. 5516, pp. 479–481, 2001.
- [128] T. Heine, “Transition metal chalcogenides: ultrathin inorganic materials with tunable electronic properties,” *Accounts of Chemical Research*, vol. 48, no. 1, pp. 65–72, 2015.
- [129] H. Guo, N. Lu, L. Wang, X. Wu, and X. C. Zeng, “Tuning electronic and magnetic properties of early transition-metal dichalcogenides via tensile strain,” *The Journal of Physical Chemistry C*, vol. 118, no. 13, pp. 7242–7249, 2014.
- [130] Q. Xu, A. Sharma, B. Comer, H. Huang, E. Chow, A. J. Medford, J. E. Pask, and P. Suryanarayana, “SPARC: Simulation package for ab-initio real-space calculations,” *SoftwareX*, vol. 15, p. 100709, 2021.
- [131] S. Ghosh and P. Suryanarayana, “SPARC: Accurate and efficient finite-difference formulation and parallel implementation of Density Functional Theory: Isolated clusters,” *Computer Physics Communications*, vol. 212, pp. 189–204, 2017.
- [132] S. Ghosh and P. Suryanarayana, “SPARC: Accurate and efficient finite-difference formulation and parallel implementation of Density Functional Theory: Extended systems,” *Computer Physics Communications*, vol. 216, pp. 109–125, 2017.
- [133] A. S. Banerjee and P. Suryanarayana, “Cyclic density functional theory: A route to the first principles simulation of bending in nanostructures,” *Journal of the Mechanics and Physics of Solids*, vol. 96, pp. 605–631, 2016.
- [134] P. Suryanarayana and D. Phanish, “Augmented Lagrangian formulation of orbital-free density functional theory,” *Journal of Computational Physics*, vol. 275, no. 0, pp. 524–538, 2014.
- [135] S. Ghosh and P. Suryanarayana, “Higher-order finite-difference formulation of periodic Orbital-free Density Functional Theory,” *Journal of Computational Physics*, vol. 307, pp. 634–652, 2016.

- [136] P. P. Pratapa, P. Suryanarayana, and J. E. Pask, “Anderson acceleration of the Jacobi iterative method: An efficient alternative to Krylov methods for large, sparse linear systems,” *Journal of Computational Physics*, vol. 306, pp. 43–54, 2016.
- [137] P. Suryanarayana, P. P. Pratapa, and J. E. Pask, “Alternating Anderson–Richardson method: An efficient alternative to preconditioned Krylov methods for large, sparse linear systems,” *Computer Physics Communications*, vol. 234, pp. 278–285, 2019.
- [138] S. Kumar, Q. Xu, and P. Suryanarayana, “On preconditioning the self-consistent field iteration in real-space Density Functional Theory,” *Chemical Physics Letters*, vol. 739, p. 136 983, 2020.
- [139] P. P. Pratapa and P. Suryanarayana, “Restarted Pulay mixing for efficient and robust acceleration of fixed-point iterations,” *Chemical Physics Letters*, vol. 635, pp. 69–74, 2015.
- [140] A. S. Banerjee, P. Suryanarayana, and J. E. Pask, “Periodic Pulay method for robust and efficient convergence acceleration of self-consistent field iterations,” *Chemical Physics Letters*, vol. 647, pp. 31–35, 2016.
- [141] R. Jinnouchi, K. Miwa, F. Karsai, G. Kresse, and R. Asahi, “On-the-fly active learning of interatomic potentials for large-scale atomistic simulations,” *The Journal of Physical Chemistry Letters*, vol. 11, no. 17, pp. 6946–6955, 2020.
- [142] O. T. Unke, S. Chmiela, H. E. Sauceda, M. Gastegger, I. Poltavsky, K. T. Schütt, A. Tkatchenko, and K.-R. Müller, “Machine learning force fields,” *Chemical Reviews*, vol. 121, no. 16, pp. 10 142–10 186, 2021.
- [143] B. Thapa, X. Jing, J. E. Pask, P. Suryanarayana, and I. I. Mazin, “Assessing the source of error in local orbital-free density functionals,” *arXiv preprint arXiv:2302.05376*, 2023.
- [144] S. Kumar, E. L. Borda, B. Sadigh, S. Zhu, S. Hamel, B. Gallagher, V. Bulatov, J. Klepeis, and A. Samanta, “Accurate parameterization of the kinetic energy functional,” *The Journal of Chemical Physics*, vol. 156, no. 2, p. 024 110, 2022.
- [145] S. Kumar, E. L. Borda, B. Sadigh, S. Zhu, S. Hamel, B. Gallagher, V. Bulatov, J. Klepeis, and A. Samanta, “Accurate parameterization of the kinetic energy functional,” *The Journal of Chemical Physics*, vol. 156, no. 2, p. 024 110, 2022.
- [146] L. Fiedler, Z. A. Moldabekov, X. Shao, K. Jiang, T. Dornheim, M. Pavanello, and A. Cangi, “Accelerating equilibration in first-principles molecular dynamics with orbital-free density functional theory,” *Physical Review Research*, vol. 4, no. 4, p. 043 033, 2022.

- [147] A. S. Banerjee, L. Lin, P. Suryanarayana, C. Yang, and J. E. Pask, “Two-level Chebyshev filter based complementary subspace method: pushing the envelope of large-scale electronic structure calculations,” *Journal of Chemical Theory and Computation*, vol. 14, no. 6, pp. 2930–2946, 2018.
- [148] P. Motamarri, S. Das, S. Rudraraju, K. Ghosh, D. Davydov, and V. Gavini, “DFT-FE—A massively parallel adaptive finite-element code for large-scale density functional theory calculations,” *Computer Physics Communications*, vol. 246, p. 106 853, 2020.
- [149] D. Codony, I. Arias, and P. Suryanarayana, “Transversal flexoelectric coefficient for nanostructures at finite deformations from first principles,” *Physical Review Materials*, vol. 5, no. 3, p. L030801, 2021.
- [150] S. Kumar, D. Codony, I. Arias, and P. Suryanarayana, “Flexoelectricity in atomic monolayers from first principles,” *Nanoscale*, vol. 13, no. 3, pp. 1600–1607, 2021.
- [151] A. Bhardwaj, A. Sharma, and P. Suryanarayana, “Torsional moduli of transition metal dichalcogenide nanotubes from first principles,” *Nanotechnology*, vol. 32, no. 28, 28LT02, 2021.
- [152] A. Bhardwaj and P. Suryanarayana, “Strain engineering of Janus transition metal dichalcogenide nanotubes: an ab initio study,” *The European Physical Journal B*, vol. 95, no. 3, pp. 1–9, 2022.
- [153] S. Kumar and P. Suryanarayana, “On the bending of rectangular atomic monolayers along different directions: an ab initio study,” *Nanotechnology*, vol. 34, no. 8, p. 085 701, 2022.
- [154] A. Bhardwaj and P. S., “Ab initio study on the electromechanical response of Janus transition metal dihalide nanotubes,” *The European Physical Journal B*, vol. 96, no. 3, p. 36, 2023.
- [155] D. R. Hamann, “Optimized norm-conserving Vanderbilt pseudopotentials,” *Physical Review B*, vol. 88, no. 8, p. 085 117, 2013.
- [156] M. Schlipf and F. Gygi, “Optimization algorithm for the generation of ONCV pseudopotentials,” *Computer Physics Communications*, vol. 196, pp. 36–44, 2015.
- [157] J. P. Perdew, K. Burke, and M. Ernzerhof, “Generalized gradient approximation made simple,” *Physical Review Letters*, vol. 77, no. 18, p. 3865, 1996.
- [158] *The Elk Code*, <http://elk.sourceforge.net/>.

- [159] C. Ataca, H. Sahin, and S. Ciraci, “Stable, single-layer MX₂ transition-metal oxides and dichalcogenides in a honeycomb-like structure,” *The Journal of Physical Chemistry C*, vol. 116, no. 16, pp. 8983–8999, 2012.
- [160] C.-H. Chang, X. Fan, S.-H. Lin, and J.-L. Kuo, “Orbital analysis of electronic structure and phonon dispersion in MoS₂, MoSe₂, WS₂, and WSe₂ monolayers under strain,” *Physical Review B*, vol. 88, no. 19, p. 195 420, 2013.
- [161] B. Amin, T. P. Kaloni, and U. Schwingenschlögl, “Strain engineering of WS₂, WSe₂, and WTe₂,” *RSC Advances*, vol. 4, no. 65, pp. 34 561–34 565, 2014.
- [162] A. Kuc, N. Zibouche, and T. Heine, “Influence of quantum confinement on the electronic structure of the transition metal sulfide TS₂,” *Physical Review B*, vol. 83, no. 24, p. 245 213, 2011.
- [163] Q. Xu, A. Sharma, and P. Suryanarayana, “M-SPARC: Matlab-simulation package for ab-initio real-space calculations,” *SoftwareX*, vol. 11, p. 100 423, 2020.
- [164] B. Zhang, X. Jing, S. Kumar, and P. Suryanarayana, “Version 2.0.0-M-SPARC: Matlab-Simulation Package for Ab-initio Real-space Calculations,” *SoftwareX*, vol. 21, p. 101 295, 2023.
- [165] M. Milivojević, S. Dmitrovic, M. Damnjanovic, and T. Vuković, “Spin–Orbit Effects in MoS₂ Nanotubes,” *The Journal of Physical Chemistry C*, vol. 124, no. 20, pp. 11 141–11 149, 2020.
- [166] K. Momma and F. Izumi, “VESTA: a three-dimensional visualization system for electronic and structural analysis,” *Journal of Applied Crystallography*, vol. 41, no. 3, pp. 653–658, 2008.
- [167] M. F. Shojaei, J. E. Pask, A. J. Medford, and P. Suryanarayana, “Soft and transferable pseudopotentials from multi-objective optimization,” *Computer Physics Communications*, vol. 283, p. 108 594, 2023.
- [168] W. Shi and Z. Wang, “Mechanical and electronic properties of Janus monolayer transition metal dichalcogenides,” *Journal of Physics: Condensed Matter*, vol. 30, no. 21, p. 215 301, 2018.
- [169] A. R. Klots, A. K. M. Newaz, B. Wang, D. Prasai, H. Krzyzanowska, J. Lin, D. Caudel, N. J. Ghimire, J. Yan, B. L. Ivanov, *et al.*, “Probing excitonic states in suspended two-dimensional semiconductors by photocurrent spectroscopy,” *Scientific Reports*, vol. 4, no. 1, pp. 1–7, 2014.
- [170] M. M. Ugeda, A. J. Bradley, S.-F. Shi, H. Felipe, Y. Zhang, D. Y. Qiu, W. Ruan, S.-K. Mo, Z. Hussain, Z.-X. Shen, *et al.*, “Giant bandgap renormalization and ex-

citonic effects in a monolayer transition metal dichalcogenide semiconductor,” *Nature Materials*, vol. 13, no. 12, pp. 1091–1095, 2014.

- [171] H. M. Hill, A. F. Rigosi, K. T. Rim, G. W. Flynn, and T. F. Heinz, “Band alignment in MoS₂/WS₂ transition metal dichalcogenide heterostructures probed by scanning tunneling microscopy and spectroscopy,” *Nano Letters*, vol. 16, no. 8, pp. 4831–4837, 2016.
- [172] K. S. Novoselov, D. Jiang, F. Schedin, T. Booth, V. Khotkevich, S. Morozov, and A. K. Geim, “Two-dimensional atomic crystals,” *Proceedings of the National Academy of Sciences*, vol. 102, no. 30, pp. 10 451–10 453, 2005.
- [173] J. N. Coleman, M. Lotya, A. O’Neill, S. D. Bergin, P. J. King, U. Khan, K. Young, A. Gaucher, S. De, R. J. Smith, *et al.*, “Two-dimensional nanosheets produced by liquid exfoliation of layered materials,” *Science*, vol. 331, no. 6017, pp. 568–571, 2011.
- [174] X. Gonze, J.-M. Beuken, R. Caracas, F. Detraux, M. Fuchs, G.-M. Rignanese, L. Sindic, M. Verstraete, G. Zerah, F. Jollet, *et al.*, “First-principles computation of material properties: the ABINIT software project,” *Computational Materials Science*, vol. 25, no. 3, pp. 478–492, 2002.
- [175] J. Heyd, G. E. Scuseria, and M. Ernzerhof, “Hybrid functionals based on a screened Coulomb potential,” *The Journal of Chemical Physics*, vol. 118, no. 18, pp. 8207–8215, 2003.
- [176] M. B. Sreedhara, Y. Miroshnikov, K. Zheng, L. Houben, S. Hettler, R. Arenal, I. Pinkas, S. S. Sinha, I. E. Castelli, and R. Tenne, “Nanotubes from Ternary WS_{2(1-x)}Se_{2x} Alloys: Stoichiometry Modulated Tunable Optical Properties,” *Journal of the American Chemical Society*, 2022.
- [177] A. C. Ugural and S. K. Fenster, *Advanced strength and applied elasticity*. Pearson education, 2003.
- [178] C. Li and T.-W. Chou, “A structural mechanics approach for the analysis of carbon nanotubes,” *International Journal of Solids and Structures*, vol. 40, no. 10, pp. 2487–2499, 2003.
- [179] K. I. Tserpes and P. Papanikos, “Finite element modeling of single-walled carbon nanotubes,” *Composites Part B: Engineering*, vol. 36, no. 5, pp. 468–477, 2005.
- [180] R Zhang and R Cheung, “Mechanical properties and applications of two-dimensional materials,” in *Two-dimensional Materials - Synthesis, Characterization and Potential Applications*. IntechOpen, 2016, ch. 10, pp. 219–246.

- [181] Z. Fan, Z. Wei-Bing, and T. Bi-Yu, “Electronic structures and elastic properties of monolayer and bilayer transition metal dichalcogenides MX_2 (M= Mo, W; X= O, S, Se, Te): a comparative first-principles study,” *Chinese Physics B*, vol. 24, no. 9, p. 097 103, 2015.
- [182] N. A. Pike, A. Dewandre, B. Van Troeye, X. Gonze, and M. J. Verstraete, “Vibrational and dielectric properties of monolayer transition metal dichalcogenides,” *Physical Review Materials*, vol. 3, no. 7, p. 074 009, 2019.
- [183] T. C. T. Ting and T. Chen, “Poisson’s ratio for anisotropic elastic materials can have no bounds,” *The Quarterly Journal of Mechanics and Applied Mathematics*, vol. 58, no. 1, pp. 73–82, 2005.
- [184] I. N. Frantsevich, F. F. Voronov, and S. A. Bokuta, *Elastic Moduli of Metals and Insulators Handbook (Kiev)*, 1983.
- [185] N. Glebko, I. Aleksandrova, G. C. Tewari, T. S. Tripathi, M. Karppinen, and A. J. Karttunen, “Electronic and vibrational properties of TiS_2 , ZrS_2 , and HfS_2 : Periodic trends studied by dispersion-corrected hybrid density functional methods,” *The Journal of Physical Chemistry C*, vol. 122, no. 47, pp. 26 835–26 844, 2018.
- [186] R. T. Sanderson, “Electronegativity and bonding of transitional elements,” *Inorganic Chemistry*, vol. 25, no. 19, pp. 3518–3522, 1986.
- [187] M. Winter, “WebElements [[http://www. webelements. com/](http://www.webelements.com/)], University of Sheffield,” *UK.(Reference Date: 01/02/2000)*, 2000.
- [188] D. F. C. Morris and L. H. Ahrens, “Ionization potentials and the chemical binding and structure of simple inorganic crystalline compounds—I: Chemical binding,” *Journal of Inorganic and Nuclear Chemistry*, vol. 3, no. 5, pp. 263–269, 1956.
- [189] T. Nilges, S. Lange, M. Bawohl, J. M. Deckwart, M. Janssen, H.-D. Wiemhöfer, R. Decourt, B. Chevalier, J. Vannahme, H. Eckert, *et al.*, “Reversible switching between p-and n-type conduction in the semiconductor $\text{Ag}_{10}\text{Te}_4\text{Br}_3$,” *Nature Materials*, vol. 8, no. 2, pp. 101–108, 2009.
- [190] J. Zhang, P. Gu, G. Long, R. Ganguly, Y. Li, N. Aratani, H. Yamada, and Q. Zhang, “Switching charge-transfer characteristics from p-type to n-type through molecular “doping”(co-crystallization),” *Chemical Science*, vol. 7, no. 6, pp. 3851–3856, 2016.
- [191] H. Hiramatsu, K. Ueda, H. Ohta, M. Hirano, M. Kikuchi, H. Yanagi, T. Kamiya, and H. Hosono, “Heavy hole doping of epitaxial thin films of a wide gap p-type semiconductor, LaCuOSe , and analysis of the effective mass,” *Applied Physics Letters*, vol. 91, no. 1, p. 012 104, 2007.

- [192] L. Chen, J. Yang, S. Klaus, L. J. Lee, R. Woods-Robinson, J. Ma, Y. Lum, J. K. Cooper, F. M. Toma, L.-W. Wang, *et al.*, “p-Type transparent conducting oxide/n-type semiconductor heterojunctions for efficient and stable solar water oxidation,” *Journal of the American Chemical Society*, vol. 137, no. 30, pp. 9595–9603, 2015.
- [193] T. Wen, Y. Wang, N. Li, Q. Zhang, Y. Zhao, W. Yang, Y. Zhao, and H.-K. Mao, “Pressure-driven reversible switching between n-and p-Type conduction in chalcopyrite CuFeS_2 ,” *Journal of the American Chemical Society*, vol. 141, no. 1, pp. 505–510, 2018.
- [194] B. D. Naab, S. Himmelberger, Y. Diao, K. Vandewal, P. Wei, B. Lussem, A. Salleo, and Z. Bao, “High mobility n-type transistors based on solution-sheared doped 6,13-Bis (triisopropylsilylethynyl) pentacene thin films,” *Advanced Materials*, vol. 25, no. 33, pp. 4663–4667, 2013.
- [195] A. N. Enyashin, V. V. Ivanovskaya, I. R. Shein, Y. N. Makurin, N. I. Medvedeva, A. A. Sofronov, and A. L. Ivanovskii, “Interatomic interactions and electronic structure of NbSe_2 and $\text{Nb}_{1.25}\text{Se}_2$ nanotubes,” *Journal of Structural Chemistry*, vol. 45, no. 4, pp. 547–556, 2004.
- [196] V. V. Ivanovskaya, A. N. Enyashin, N. I. Medvedeva, and A. L. Ivanovskii, “Electronic properties of superconducting NbSe_2 nanotubes,” *Physica Status Solidi (B)*, vol. 238, no. 3, R1–R4, 2003.
- [197] R. F. W. Bader and T. Nguyen-Dang, “Quantum theory of atoms in molecules–Dalton revisited,” in *Advances in Quantum Chemistry*, vol. 14, Elsevier, 1981, pp. 63–124.
- [198] W. Tang, E. Sanville, and G. Henkelman, “A grid-based bader analysis algorithm without lattice bias,” *Journal of Physics: Condensed Matter*, vol. 21, no. 8, p. 084 204, 2009.
- [199] Y. C. Cheng, Z. Y. Zhu, M. Tahir, and U. Schwingenschlögl, “Spin-orbit–induced spin splittings in polar transition metal dichalcogenide monolayers,” *Europhysics Letters*, vol. 102, no. 5, p. 57 001, 2013.
- [200] A. Rezavand and N. Ghobadi, “Stacking-dependent Rashba spin-splitting in Janus bilayer transition metal dichalcogenides: The role of in-plane strain and out-of-plane electric field,” *Physica E: Low-dimensional Systems and Nanostructures*, vol. 132, p. 114 768, 2021.
- [201] Y. Huang, J. Wu, and K.-C. Hwang, “Thickness of graphene and single-wall carbon nanotubes,” *Physical Review B*, vol. 74, no. 24, p. 245 413, 2006.

- [202] M. M. J. Treacy, T. W. Ebbesen, and J. M. Gibson, “Exceptionally high Young’s modulus observed for individual carbon nanotubes,” *Nature*, vol. 381, no. 6584, pp. 678–680, 1996.
- [203] E. D. Minot, Y. Yaish, V. Sazonova, J.-Y. Park, M. Brink, and P. L. McEuen, “Tuning carbon nanotube band gaps with strain,” *Physical Review Letters*, vol. 90, no. 15, p. 156401, 2003.
- [204] G. Hautier, A. Miglio, G. Ceder, G.-M. Rignanese, and X. Gonze, “Identification and design principles of low hole effective mass p-type transparent conducting oxides,” *Nature Communications*, vol. 4, no. 1, pp. 1–7, 2013.
- [205] C. Wee, S. Maikop, and C. Y. Yu, “Mobility-enhancement technologies,” *IEEE Circuits and Devices Magazine*, vol. 21, no. 3, pp. 21–36, 2005.
- [206] N. Mohta and S. E. Thompson, “Mobility enhancement,” *IEEE Circuits and Devices Magazine*, vol. 21, no. 5, pp. 18–23, 2005.
- [207] T. Mizuno, S. Takagi, N. Sugiyama, H. Satake, A. Kurobe, and A. Toriumi, “Electron and hole mobility enhancement in strained-Si MOSFET’s on SiGe-on-insulator substrates fabricated by SIMOX technology,” *IEEE Electron Device Letters*, vol. 21, no. 5, pp. 230–232, 2000.
- [208] C. K. Maiti, L. K. Bera, S. S. Dey, D. K. Nayak, and N. B. Chakrabarti, “Hole mobility enhancement in strained-Si p-MOSFETs under high vertical field,” *Solid-State Electronics*, vol. 41, no. 12, pp. 1863–1869, 1997.
- [209] A. Sharma and P. Suryanarayana, “Real-space density functional perturbation theory for phonons,” *arXiv preprint arXiv:2202.13534*, 2022.
- [210] P. Suryanarayana, “On spectral quadrature for linear-scaling density functional theory,” *Chemical Physics Letters*, vol. 584, pp. 182–187, 2013.
- [211] P. P. Pratapa, P. Suryanarayana, and J. E. Pask, “Spectral Quadrature method for accurate $O(N)$ electronic structure calculations of metals and insulators,” *Computer Physics Communications*, vol. 200, pp. 96–107, 2016.
- [212] P. Suryanarayana, P. P. Pratapa, A. Sharma, and J. E. Pask, “SQDFT: Spectral Quadrature method for large-scale parallel $O(N)$ Kohn–Sham calculations at high temperature,” *Computer Physics Communications*, vol. 224, pp. 288–298, 2018.
- [213] P. Suryanarayana, V. Gavini, T. Blesgen, K. Bhattacharya, and M. Ortiz, “Non-periodic finite-element formulation of Kohn–Sham density functional theory,” *Journal of the Mechanics and Physics of Solids*, vol. 58, no. 2, pp. 256–280, 2010.

- [214] K. Bhattacharya, V. Gavini, M. Ortiz, M. Ponga, and P. Suryanarayana, “Accurate approximations of density functional theory for large systems with applications to defects in crystalline solids,” *arXiv preprint arXiv:2112.06016*, 2021.
- [215] R. Naaman and D. H. Waldeck, “Chiral-induced spin selectivity effect,” *The Journal of Physical Chemistry Letters*, vol. 3, no. 16, pp. 2178–2187, 2012.
- [216] T. Dumitrică and R. D. James, “Objective molecular dynamics,” *Journal of the Mechanics and Physics of Solids*, vol. 55, no. 10, pp. 2206–2236, 2007.